TÉCNICO LISBOA

Phase Diagram of the 4D U(1) Lattice Pure Gauge Theory

Rafael Carreira de Jesus Torres

Thesis to obtain the Master of Science Degree in

Engineering Physics

Supervisors: Prof. Pedro José Gonçalves Ribeiro
Prof. Nuno Miguel Ribeiro Cardoso

Examination Committee

Chairperson: Prof. Carlos Manuel Dos Santos Rodrigues da Cruz
Supervisor: Prof. Nuno Miguel Ribeiro Cardoso
Members of the Committee: Prof. João Carlos Carvalho de Sá Seixas
Prof. Eduardo Filipe Vieira de Castro

Semptember 2021

Acknowledgments

First and foremost, I would like to extend my deepest gratitude to Professor Pedro Ribeiro, Professor Nuno Cardoso, Professor Paul McClarty, and Professor Pedro Bicudo for guiding me through this project, and for the insights, availability, and support they always offered. It was an honor to work with them and learn from them as much as I did.

I would also like to thank my friends from IST who were there in the hardest moments of this degree and who made the best ones happen. Thank you also to all friends who were not in the faculty with me every day, but were present in other ways, and undoubtedly take responsibility for the personal growth I experienced. I am very grateful for the encouragement they gave me in all steps of this journey and for having them in my life.

Last but definitely not least, I must thank my mother, father, and sister for their unconditional support and advice. Without them, none of this would have been possible, and I am forever thankful for everything they did for me.

Resumo

Lattice gauge theory (LGT) fornece um quadro em que é possível explicar o fenómeno do confinamento em teorias de gauge, o que é fundamental em teorias como a cromodinâmica quântica. Em LGT em três dimensões simétrica sob o grupo $\mathrm{U}(1)$, encontramos confinamento ao longo de todo o espaço de parâmetros, enquanto que, em quatro dimensões, ocorre uma transição de fase entre uma fase confinada e uma fase de Coulomb, na qual as cargas interagem segundo a eletrodinâmica quântica.

Neste projeto, métodos de Monte Carlo são utilizados para simular LGT com simetria $\mathrm{U}(1)$ em quatro dimensões, com diferentes extensões da rede nas direções espaciais e temporal, utilizando o Polyakov loop e a string tension como parâmetros de ordem para a transição de fase.

A transição de fase deste modelo é identificada e, utilizando redes anisotrópicas, é obtido o coupling crítico para o qual a transição de fase ocorre a diferentes temperatures. Deste modo, o diagrama de fase da teoria é construído.

Adicionalmente, a ordem da transição de fase é investigada para redes isotrópicas. É determinada uma transição de fase descontínua, de primeira ordem para baixas temperaturas. Com o aumento da temperatura, a descontinuidade diminui até que a transição se torna de segunda ordem.

Palavras-chave: Lattice gauge theory, Transição de fase, Diagrama de fase, Confinamento, Monte Carlo.

Abstract

Lattice gauge theory (LGT) provides a framework to understand confinement in gauge theories, which is fundamental in theories such as quantum chromodynamics. In three dimensional $\mathrm{U}(1)$ LGT, confinement is present throughout all of the parameter space, while in four dimensions a phase transition takes place between a confining phase and a Coulomb phase, in which the charges interact according to quantum electrodynamics.

In this project, we simulate $\mathrm{U}(1)$ LGT using the Monte Carlo method on four dimensional lattices with different lattice sizes in the spatial and temporal directions, using the Polyakov loop and the string tension as the order parameters identifying the phase transition.

We identify the phase transition of the $\mathrm{U}(1)$ LGT and, by using anisotropic lattices, we recover the critical coupling at which the transition occurs for different temperatures, and construct the phase diagram of this theory.

We further investigate the order of the phase transition for isotropic lattices, finding a first order transition at low temperatures, which becomes weaker with increasing temperature, until in becomes second order.

Keywords: Lattice gauge theory, Phase transition, Phase diagram, Confinement, Monte Carlo.

Contents

Acknowledgments . . . iii
Resumo . . . v
Abstract . . . vii
List of Tables . . . xi
List of Figures . . . xiii
List of Abbreviations . . . xv

1 Introduction **1**

2 Lattice Gauge Theory **3**
2.1 Gauge theory on the continuum . . . 3
2.1.1 Quantization . . . 5
2.2 Path Integral . . . 5
2.2.1 The quantum mechanical path integral . . . 5
2.2.2 The path integral for a gauge theory . . . 7
2.3 Spacetime discretization . . . 8
2.3.1 Fermion Hamiltonian . . . 8
2.3.2 Gauge Field Hamiltonian . . . 10
2.3.3 Derivation of the action . . . 13
2.3.4 Continuum limit . . . 16
2.4 Observables . . . 17
2.4.1 Potential . . . 18
2.5 Temperature . . . 20

3 U(1) Lattice Gauge Theory **21**
3.1 Strong Coupling Limit . . . 21
3.2 Weak Coupling Limit . . . 23
3.2.1 Dirac Monopoles . . . 24
3.2.2 U(1) LGT . . . 25
3.3 Phase Transition . . . 27
3.4 Order of the Phase Transition . . . 28

4 Markov Chain Monte Carlo **29**
4.1 Monte Carlo method . . . 29
4.1.1 Importance sampling . . . 30
4.2 Markov Chain . . . 31
4.3 Metropolis-Hastings Algorithm . . . 32
4.4 Running the simulation . . . 33
4.4.1 Initialization . . . 33
4.4.2 Thermalization . . . 34
4.4.3 Autocorrelation . . . 35
4.4.4 Jacknife . . . 37
4.4.5 Multihit . . . 38
4.4.6 Multilevel . . . 38
4.5 CUDA . . . 40

5 Simulation of the U(1) LGT **41**
5.1 Isotropic Lattice . . . 41
5.1.1 Simulation results . . . 42
5.2 Potential . . . 45
5.3 Order of the Phase Transition . . . 46
5.4 Anisotropic Lattice . . . 48
5.4.1 Simulation results . . . 49
5.4.2 Correction to the Villain approximation . . . 50
5.4.3 Rescaling of the phase diagram . . . 52
5.5 Running coupling constant . . . 55
5.5.1 Anisotropic lattice . . . 56
5.5.2 Running coupling in U(1) LGT . . . 57
5.6 Renormalized anisotropy parameter . . . 59

6 Conclusion **63**

Bibliography **65**

A Gauge fixing **67**
A.1 Temporal gauge . . . 68

B Euclidean correlator **69**

C Tables and Figures **71**

List of Tables

4.1 Autocorrelation times for the average plaquette with 0, 1, 2 and 3 overrelaxation steps for a 24^4 lattice with $\beta = 1$. Note that using one single overrelaxation step significantly reduces the autocorrelation time. 37

5.1 Position of the peaks in the Polyakov Loop susceptibility for an isotropic lattice with $N_s = 24$. 44

5.2 Parameters obtain in the fit to $g(x) = a + b \cdot x + c \cdot x^2 + d \cdot x^3 + e \cdot x^4$ 53

5.3 Fitting parameters obtained in the fit of equation 5.5.15 to the data in tables C.3, C.4 and C.5. Note that for $\xi N_t = 6$, the fit was done without the parameter α_t^3 because less points were available. 58

5.4 Values of $\left(\frac{a_s}{a_t}\right)_{phys}$ calculated at the phase transition on a 24^4 lattice, for each ξ, using different distances. 61

C.1 Fitting parameters obtained in the fit of an equation of the form $aV(r) = A - \frac{b}{r} + \sigma r$ to the potential obtained for a 24^4 isotropic lattice. 71

C.2 Position of the peak in the Polyakov loop susceptibility, β_C,for each value of ξ and $N_t$on a $4\mathcal{D}$ lattice with $N_s = 24$. 72

C.3 Critical value of β_t obtained in the simulations with $4\mathcal{D}$ lattices regularizations in which $\xi N_t = 4$ and $N_s = 24$. 72

C.4 Critical value of β_t obtained in the simulations with $4\mathcal{D}$ lattices regularizations in which $\xi N_t = 6$ and $N_s = 24$. 73

C.5 Critical value of β_t obtained in the simulations with $4\mathcal{D}$ lattices regularizations in which $\xi N_t = 8$ and $N_s = 24$. 73

List of Figures

2.1 The link variable $U_\mu(x)$ connecting lattice sites n and $n+\hat{\mu}$. 9

2.2 The plaquette $\Pi_{\mu\nu}(n)$ is defined at each lattice site as the product of link variables $U_\mu(n)$ oriented around an elementary square. 11

2.3 A representation of the Polyakov loop correlator. The Polyakov loop at r_1 and the anti-Polyakov loop at r_2 are related, respectively, to the propagator of a charge and an anti-charge. As such, this situation can be interpreted as having a charge at r_1 and an anti-charge at r_2, and we can thus use the Polyakov loop correlator to determin the Potential between these two charges. 20

3.1 As we circle around the vortex marked by the $\times$ on the figure, the phases $\phi(x)$ have a 2π jump at the dashed line. Reproduced from [7]. 24

4.1 Average value of the plaquette calculated in an isotropic lattice with $\beta = 1$ at different system sizes. After 2000 iterations, the value of the average of the observable is stable, indicating that the system has reached equilibrium. 34

5.1 Average value of the plaquette (a) and plaquette susceptibility (b) as a function of β for a $4\mathcal{D}$ lattice with $N_t = 4, 6, 8, 10, 12.$ and $N_s = 24.$ 43

5.2 Average value of the Polyakov loop (a) and Polyakov loop susceptibility (b) as a function of β for a $4\mathcal{D}$ lattice with $N_t = 4, 6, 8, 10, 12.$ and $N_s = 24.$ 43

5.3 Position of the peaks in the Polyakov loop susceptibility obtained in blue. In gray, the points from the phase diagram obtained in [18]. The results obtained show great agreement with the literature. 44

5.4 Potential calculated on an isotropic 24^4 lattice for $\beta = 1, 3$, using the multihit and the multilevel methods. For $\beta = 1$, we obtain a linear potential at large distances, corresponding to the confined phase, while for $\beta = 3$ we obtain a Coulomb potential, approaching a constant value for large distances, characteristic of the deconfined phase. 45

5.5 String tension calculated for values of β near the phase transition. Before the phase transition, in the confined phase, this parameter has a finite value, and it decreases as we approach the phase transition, becoming zero in the deconfined phase. 46

5.6 Histogram of the absolute value of the Polyakov loop calculated in a four dimensional lattice with $N_s = 24$ and $N_t = 8$, at the value of the coupling parameter determined for the phase transition, in table 5.1, $\beta = 1.01043$. We can identify two peaks, indicating a first order transition. 47
5.7 Histogram of the absolute value of the Polyakov loop calculated in a four dimensional lattice with $N_s = 24$ and $N_t = 2$, at the value of the coupling parameter determined for the phase transition, in table 5.1, $\beta = 0.89929$. Only one peak is seen, which indicates a continuous transition. 47
5.8 Position of the peaks in the Polyakov loop susceptibility in terms of the quantities in equation 5.4.6 50
5.9 Phase diagram using the relations in equation 5.4.15. 52
5.10 Fit function (orange) and points calculated with the values of β_0 and ξ shown in table C.2 (blue). 53
5.11 Phase diagram in terms of the parameters in equation 5.4.19. 54
5.12 Comparison between the different functions used in the relations in equation 5.4.19. . . . 55
5.13 Phase diagram of the $\mathrm{U}(1)$ LGT in terms of the parameters in equation 5.4.6 with the coupling parameter transformed according to equation 5.5.16, with the parameters obtained for lattice regularizations with $\xi N_t = 6$ 59
5.14 Potential calculated on a 24^4 lattice for β at the phase transition, using the Wilson Loop, for several values of ξ. 60

C.1 Phase diagram of the $\mathrm{U}(1)$ LGT in terms of the parameters in equation 5.4.6 with the coupling parameter transformed according to equation 5.5.16, with the parameters obtained for lattice regularizations with $\xi N_t = 4$ 73
C.2 Phase diagram of the $\mathrm{U}(1)$ LGT in terms of the parameters in equation 5.4.6 with the coupling parameter transformed according to equation 5.5.16, with the parameters obtained for lattice regularizations with $\xi N_t = 8$ 74

List of Abbreviations

LGT	Lattice gauge theory
QED	Quantum electrodynamics
QCD	Quantum chromodynamics

Chapter 1

Introduction

Lattice gauge theories (LGT) [1] allow for the study of gauge theories without using perturbative methods. Performing non-perturbative calculations on a gauge theory in continuous spacetime involves the evaluation of infinite dimensional path integrals, which is not computationally feasible. By Wick rotating spacetime into Eucledian space and discretizing spacetime onto a finite lattice, the path integral becomes finite dimensional which allows for the theory to be simulated and calculations to be made using stochastic techniques. Taking the lattice size to infinity and the lattice spacings to zero, the continuum theory is recovered.

An important result of lattice gauge theory is that it provides a framework to understand confinement in gauge theories, which is fundamental to the nature of quantum chromodynamics (QCD) at low energies.

In this work, we will be interested in the gauge theory which is symmetric under the compact $\mathrm{U}(1)$ group. In three dimensions, the compact $\mathrm{U}(1)$ lattice gauge theory exhibits confinment through all the parameter space, so that free charges can not be observed. As such, the study of this theory can provide insights into more mathematically complex theories, such as QCD. The four dimensional $\mathrm{U}(1)$ LGT is even more interesting, as it also exhibits a phase where the gauge fields confine electrical charges at strong coupling, similarly to the three dimensional case, but, at weak coupling, confinement is no longer present and charged particles interact through a Coulomb interaction, as in quantum electrodynamics (QED). At some coupling, a phase transition is observed separating the two phases of the theory. Although the two phases of this theory are known, a complete phase diagram identifying the phase structure of the theory at a full range of values for the temperature and coupling, including the nature of the phase transition, is still missing.

The goal of this work is to study the phases of the compact $4\mathcal{D}\ \mathrm{U}(1)$ LGT, by simulating the theory and computing observables using Markov Chain Monte Carlo methods. By running simulations at different temperatures, we obtain a phase diagram of this theory.

The outline of this thesis is as follows. We begin by introducing the topic of lattice gauge theory in chapter 2, where we also present the discretization of spacetime in order to construct the action for the pure $\mathrm{U}(1)$ LGT, and present observables relevant to this study. Then, in chapter 3, we look into

the strong and weak coupling limits of $\mathrm{U}(1)$ LGT, introduce the mechanism responsible for the phase transition, and discuss order parameters which allow the distinction between the two phases. Chapter 4 is devoted to a presentation of the numerical methods used in the generation of configurations for the simulation of this theory, and the statistical techniques used to analyse our results. Finally, we present the results of this work in chapter 5 and conclude in chapter 6.

Chapter 2

Lattice Gauge Theory

In this section, we present an overview of lattice gauge theory (LGT). We begin by reviewing the action for a continuum gauge theory and present the path integral as a quantization procedure. We then introduce the spacetime discretization of the lattice regularization, and construct the action for a pure $\mathrm{U}(1)$ lattice gauge theory from the gauge field Hamiltonian. Finally we introduce observables on the lattice relevant to this work, and present how to determine temperature on the lattice. Our description follows [2] and [3].

2.1 Gauge theory on the continuum

The fermionic degrees of freedom of the gauge field theory are represented by the Dirac 4-spinors $\psi(x)^{(f)}$ and $\bar{\psi}(x)^{(f)}$ with $x = (x_1, x_2, x_3, x_4)$ the spacetime position and $f = 1, 2, \cdots, N_f$ the flavour index. The total number of flavours varies according to the gauge group considered. In some gauge groups, the fermionic fields may also have a color index associated. In order to keep the notation simple, we will omit these, as well as the Dirac indexes, and use vector/matrix notation. The fermion fields transform under some representation of the symmetry group as

$$\begin{aligned} \psi(x) &\to \Omega(x)\psi(x) \\ \bar{\psi}(x) &\to \bar{\psi}(x)\Omega(x)^\dagger, \end{aligned} \tag{2.1.1}$$

where $\Omega(x)$ is an element of the symmetry group considered.

With these fields, we can construct the fermionic action as a functional of $\psi(x)^{(f)}$ and $\bar{\psi}(x)^{(f)}$ as

$$S_F^0[\psi, \bar{\psi}, A] = \sum_{f=1}^{N_f} \int \bar{\psi}^{(f)}(x) \left(\gamma_\mu \partial_\mu + m^{(f)}\right) \psi^{(f)}(x) \mathrm{d}^4 x \,, \tag{2.1.2}$$

where γ_μ are the Dirac matrices obeying the anti-commutation rules $\{\gamma_\mu, \gamma_\nu\} = 2\delta_{\mu\nu}$. Note that this action is written in euclidean space, as it will be useful to work in this space for reasons we will visit in the next section.

The gauge principle states that the action must be invariant under the local gauge transformations

in equation 2.1.1. However, applying these to the action in equation 2.1.2, we notice that only the mass term remains invariant. Applying the transformation to the first terms of the action yields an additional term $\partial_\mu \Omega(x)$. Gauge invariance can be restored by replacing the derivative in the action with the *covariant derivative*, $D_\mu(x)$, defined as

$$D_\mu(x) = \partial_\mu + \mathrm{i}gA_\mu(x)\,, \tag{2.1.3}$$

where we introduce the *gauge coupling* g and the *gauge field* A_μ, which has this name because it is the field we need to introduce to recover the gauge invariance of the action in equation 2.1.2. The gauge fields are elements of the Lie algebra corresponding to the gauge group of the theory and transform under a local gauge transformation as

$$A_\mu(x) \to \Omega(x)A_\mu(x)\Omega(x)^\dagger + \mathrm{i}\left(\partial_\mu\Omega(x)\right)\Omega(x)^\dagger\,. \tag{2.1.4}$$

As such, the covariant derivative transforms as

$$D_\mu(x) \to \Omega(x)D_\mu(x)\Omega(x)^\dagger\,, \tag{2.1.5}$$

and thus, replacing the derivative in the action in equation 2.1.2 with the covariant derivative, we obtain the gauge invariant fermionic action, which describes the dynamics of the fermionic degrees of freedom, their self interactions, and couplings to the gauge fields. This is given by

$$S_F[\psi,\bar{\psi},A] = \sum_{f=1}^{N_f}\int \bar{\psi}^{(f)}(x)\left(\gamma_\mu D_\mu + m^{(f)}\right)\psi^{(f)}(x)\mathrm{d}^4x\,. \tag{2.1.6}$$

Next, in order to construct the gauge field part of the action, we consider the *field strength tensor*, $F_{\mu\nu}$ given by

$$F_{\mu\nu}(x) = \frac{1}{ig}\left[D_\mu(x), D_\nu(x)\right] = \partial_\mu A_\nu(x) - \partial_\nu A_\mu(x) + \mathrm{i}g\left[A_\mu(x), A_\nu(x)\right]\,, \tag{2.1.7}$$

which transforms in the same way as the covariant derivative D_μ. As such, a gauge invariant quantity can be constructed from the trace of the product $F_{\mu\nu}F_{\mu\nu}$, which we can prove to be invariant under gauge transformations by taking advantage of the cyclic property of the trace. Then, the gauge invariant action for the degrees of freedom related to the gauge fields can be written in the euclidean space as

$$S_G[A] = \frac{1}{2}\int \mathrm{tr}\left[F_{\mu\nu}(x)F_{\mu\nu}(x)\right]\mathrm{d}^4x\,. \tag{2.1.8}$$

This is the *Yang-Mills action*, which describes the dynamics of the gauge fields A_μ, as well as their self interactions. Many interesting aspects of gauge theories are encoded in the gauge degrees of freedom, and as such, we can study *pure gauge theories* by considering only this part of the action.

Note that in the $\mathrm{U}(1)$ gauge theory, the commutator in equation 2.1.7 vanishes and $F_{\mu\nu}$ is identified with the electromagnetic tensor, so that the action in equation 2.1.8 describes quantum electrodynamics (QED).

2.1.1 Quantization

The continuum gauge theory motivated in the preceding section is a classical field theory. In order for it to describe particle dynamics, we must then apply a quantization procedure, in order to turn the theory into a quantum field theory.

In the *canonical quantization* scheme, fields and their conjugate momenta are replaced by quantum mechanical operators, and the canonical commutation relations are imposed between them, which lead to the identification of operator products as products of creation and annihilation operators.

Alternatively, we can use the *path integral* formalism to quantize the classical fields. In the following section, we introduce this method, by first applying it to a quantum mechanical system and then looking at the case of a gauge theory.

2.2 Path Integral

2.2.1 The quantum mechanical path integral

Consider the quantum mechanical system of a particle propagating in a potential U, which is described by the following Hamiltonian

$$\hat{H} = \frac{\hat{p}^2}{2m} + U(\hat{x})\,. \tag{2.2.1}$$

The amplitude of the propagation of the particle between an initial point x_i and a final point x_f is given by the propagator

$$\left\langle x_f \left| \mathrm{e}^{-iT\hat{H}} \right| x_i \right\rangle\,. \tag{2.2.2}$$

In order to derive the path integral for this system, we begin by dividing the time T in which the particle propagates between x_i and x_f in intervals δt small enough so that the Hamiltonian is approximately constant in each of them. Then, we can separate the propagator in equation 2.2.2 into propagators for each time interval, by introducing partitions of the identity, such that the propagator becomes

$$\left\langle x_f \left| \mathrm{e}^{-iT\hat{H}} \right| x_i \right\rangle = \int dx_{n-1}\cdots dx_1 \left\langle x_f \left| \mathrm{e}^{-i\delta t\hat{H}(t_f)} \right| x_{n-1} \right\rangle \langle x_{n-1}\,|\cdots|\,x_1\rangle \left\langle x_1 \left| \mathrm{e}^{-i\delta t\hat{H}(t_1)} \right| x_i \right\rangle\,. \tag{2.2.3}$$

In order to evaluate this quantity, we begin by looking at each matrix element in the integral, which is given by

$$
\begin{aligned}
\left\langle x_{j+1}\left|\mathrm{e}^{-i\delta t(\hat{p}^2/2m+\hat{U})}\right|x_j\right\rangle &= \int \frac{\mathrm{d}p}{2\pi}\left\langle x_{j+1}\mid p\right\rangle\left\langle p\mid \mathrm{e}^{-i\delta t(\hat{p}^2/2m+U(\hat{x}))}\mid x_j\right\rangle \\
&= \int \frac{\mathrm{d}p}{2\pi}\left\langle x_{j+1}\mid p\right\rangle\left\langle p\mid \mathrm{e}^{-i\delta t\hat{p}^2/2m}\mathrm{e}^{-i\delta tU(\hat{x})}\mid x_j\right\rangle \\
&= \int \frac{\mathrm{d}p}{2\pi}\left\langle x_{j+1}\mid p\right\rangle\left\langle p\mid \mathrm{e}^{-i\delta tp^2/2m}\mathrm{e}^{-i\delta tU(x_j)}\mid x_j\right\rangle \\
&= \mathrm{e}^{-i\delta tU(x_j)}\int \frac{\mathrm{d}p}{2\pi}\mathrm{e}^{-i\delta tp^2/2m}\left\langle x_{j+1}\mid p\right\rangle\left\langle p\mid x_j\right\rangle \\
&= \mathrm{e}^{-i\delta tU(x_j)}\int \frac{\mathrm{d}p}{2\pi}\mathrm{e}^{-i\delta tp^2/2m}\mathrm{e}^{+ipx_{j+1}}\mathrm{e}^{-ipx_j} \\
&= \mathrm{e}^{-i\delta tU(x_j)}\int \frac{\mathrm{d}p}{2\pi}\mathrm{e}^{-i\delta tp^2/2m}\mathrm{e}^{i\delta tp\frac{x_{j+1}-x_j}{\delta t}} \\
&= C\mathrm{e}^{-i\delta tU(x_j)+i\delta t\frac{m}{2}\left(\frac{\delta x_j}{\delta t}\right)^2} \\
&= C\mathrm{e}^{+i\delta tL(x_j,\dot{x}_j)}\,.
\end{aligned}
\tag{2.2.4}
$$

To obtain this result, we began by, in the first step, introducing a partition of the identity in $|p\rangle$. Then, in the third step, we acted with $\hat{p}$ on $|p\rangle$ and with $U(\hat{x})$ on $|x\rangle$. After removing quantities which were not operators from inside the brakets in the fourth step, we used $\langle p|x\rangle = e^{-ipx}$ on the fifth step. Finally, we solved the integral by using the result of the Gaussian integral

$$
\int dp e^{-\frac{1}{2}Ap^2+Bp} = \sqrt{\frac{2\pi}{A}}e^{\frac{B^2}{A}}\,, \tag{2.2.5}
$$

with $A = \frac{i\delta t}{m}$ and $B = i\delta t\frac{\delta x_j}{\delta t}$, with $\delta x_j = x_{j+1} - x_j$. In the last step, we identified the exponent as the Lagrangian for the quantum mechanical system.

Inserting this result in equation 2.2.3, we get the following expression for the propagator

$$
\begin{aligned}
\left\langle x_f\left|\mathrm{e}^{-iT\bar{H}}\right|x_i\right\rangle &= C^n\int dx_{n-1}\cdots dx_1\mathrm{e}^{+i\delta tL(x_{n-1},\dot{x}_{n-1})}\cdots\mathrm{e}^{+i\delta tL(x_i,\dot{x}_i)} \\
&= C^n\int dx_{n-1}\cdots dx_1\mathrm{e}^{+i(\delta tL(x_{n-1},\dot{x}_{n-1})+\cdots+\delta tL(x_i,\dot{x}_i))}\,,
\end{aligned}
\tag{2.2.6}
$$

and as we take the limit $\delta t \to 0$, the exponent on the previous equation becomes the time integral of the Lagrangian, which is the action, given by

$$
S = \int_{t_i}^{t_f} dtL\,. \tag{2.2.7}
$$

And so, the propagator for this quantum mechanical system is given by the path integral as

$$
\left\langle x_f\left|\mathrm{e}^{-iT\bar{H}}\right|x_i\right\rangle = C^n\int dx_{n-1}\cdots dx_1\mathrm{e}^{iS[x]}\,. \tag{2.2.8}
$$

This result states that the propagation of a particle in this system can be thought of as the average of the propagation on each classical path, weighted by a factor $\mathrm{e}^{iS[x]}$ which depends on the action for each path, as opposed to the classical picture, where one single time evolution for the particle propagation is determined.

We now want to compute the partition function for this system, given by

$$Z = \mathrm{tr}\left[e^{-iTH}\right] = \int dx_0 \left\langle x_0 \left| \mathrm{e}^{-iT\bar{H}} \right| x_0 \right\rangle . \tag{2.2.9}$$

Inserting in this equation the result of equation 2.2.8, we find that the partition function for this system is given by

$$Z = C^n \int dx_{n-1} \cdots dx_0 \mathrm{e}^{iS[x]} = \int D[x] \mathrm{e}^{iS[x]} , \tag{2.2.10}$$

with $D[x] = \prod_i C dx_i$, meaning that, for each time i, we integrate over the domain of x. Note that this is only a formal definition, as the product $\prod_i$ in continuum time is not defined.

In practice, it is useful to make an analytical continuation to imaginary time, by considering the euclidean time, $t \to it$. Doing so, the *euclidean path integral* is given by

$$Z = \mathrm{tr}\left[e^{-T_E H}\right] = \int D[x] \mathrm{e}^{-S_E[x]} , \tag{2.2.11}$$

where T_E is the Euclidean time in which the particle propagates, and $S_E[x]$ is the action in euclidean time. We notice that the integrand is now real and bounded from above, which renders calculations much easier. Additionally, when considering the path integral for a gauge theory, we will see that considering euclidean time gives rise to an important relation with statistical physics, which will be useful.

Finally, we have obtained the partition function for a quantum mechanical system using the path integral formalism. This result shows that the euclidean path integral encodes the physical content of the theory, as the partition function allows us to obtain all the thermodynamic observables of this theory.

2.2.2 The path integral for a gauge theory

Having introduced the path integral formalism, we can now apply it to quantize the gauge field theory. To do so, we abandon the classical picture of one distinct time evolution determined by the action, and construct the partition function as an integral over all possible field configurations, weighted by a factor $e^{-S_E[\psi]}$, where $S_E[\psi]$ is the euclidean action of the theory, as

$$Z = \int \mathrm{e}^{-S_E[\psi]} \mathcal{D}[\psi] , \tag{2.2.12}$$

with

$$\mathcal{D}[\psi] = \prod \mathrm{d}\psi(x) . \tag{2.2.13}$$

The path integral formulation reveals an important relation between this quantum field theory and statistical mechanics, as the partition function obtained in terms of the path integral is similar to the partition function of a statistical mechanical system, in terms of the canonical ensemble. This analogy will become more clear once we discretize the path integral in equation 2.2.12, and will be important, as it allows us to apply methods known in statistical mechanics to evaluate our gauge field theory.

2.3 Spacetime discretization

The integral in equation 2.2.12 includes diverging terms, so for it to yield physical results, we must introduce some regularization, such as an ultraviolet cutoff, in order to take care of these arising infinities. Another way to solve this is the lattice regularization. This formalism consists of replacing continuous space–time by a discrete set of points on a lattice Λ with periodic boundary conditions, which, when working on 3 + 1 dimensions, corresponds to considering a hyper cubic lattice with N_s lattice sites on each space direction and N_t on the time direction, each separated by a lattice spacing of a_s and a_t, respectively.

In this setting, each spacetime coordinate is replaced by lattice indexes, as

$$\begin{aligned} x_i \to a_s n_{x_i} \ , \qquad & n_{x_i} = 0, 1, \cdots, N_s - 1 \\ t \to a_t n_t \ , \qquad & n_t = 0, 1, \cdots, N_t - 1 \, . \end{aligned} \tag{2.3.1}$$

And lattice sites are labeled by the vector $\mathbf{n} = (n_x, n_y, n_z, n_t)$. Now, continuous fields $\psi(x)$ live on lattice sites, and as such, are replaced by $\psi(n)$, their lattice counterpart. Therefore, the classical euclidean action becomes discretized on the lattice, and so the partition function on equation 2.2.12 now becomes

$$Z_{lat} = \int \mathrm{e}^{-S_{lat}[\psi]} \mathcal{D}[\psi] \, , \tag{2.3.2}$$

with

$$\mathcal{D}[\psi] = \prod_{n \in \Lambda} \mathrm{d}\psi(n) \, . \tag{2.3.3}$$

After the discretization procedure, the integration measure $\mathcal{D}[\psi]$ is now mathematically well defined, unlike in the continuum case in equation 2.2.13.

In order to recover the initial theory in the continuum limit, we must set the descretized lattice action to be equal to the Euclidean action in the limit where the lattice spacings go to zero, $a \to 0$. In the following sections, we set on obtaining the lattice version of the action for the gauge theory obeying this condition, starting from the Hamiltonian for the fermionic and gauge parts of the theory.

2.3.1 Fermion Hamiltonian

The fermionic part of the Hamiltonian, before enforcing gauge invariance, is given by

$$H_F = \int \mathrm{d}^3 x \bar{\psi}(x) \left(i \gamma_\mu \partial_\mu + m \right) \psi(x) \, . \tag{2.3.4}$$

As we saw before, the lattice counterpart of the continuous fields is given by $\psi(r)$, where $r = (x_1, x_2, x_3)$ labels the lattice sites. In order to write the fermionic Hamiltonian on the lattice, we also need to discretize the field derivative, which can be done by approximating the derivative with a central difference, on a small interval $2a$, with a the lattice spacing, that is,

$$\partial_\mu \psi(x) \to \frac{1}{2a}(\psi(r+\hat{\mu}) - \psi(r-\hat{\mu}))\,, \tag{2.3.5}$$

where $\hat{\mu}$ denotes the unit vector in the μ direction. Replacing the derivative in the Hamiltonian by the one in equation 2.3.5, and noting that we can discretize the integral as $\int d^3x \to a^3 \sum_{r\in\Lambda}$, we obtain the following Hamiltonian

$$H_F = a^3 \sum_{r\in\Lambda} \bar{\psi}(r) \left(\sum_{\mu=1}^{3} i\gamma_\mu \frac{\psi(r+\hat{\mu}) - \psi(r-\hat{\mu})}{2a} + m\psi(r) \right) . \tag{2.3.6}$$

Much like the in continuum case, we now need to impose gauge invariance on the discretized Hamiltonian. On the lattice, we implement the gauge transformations by choosing an element $\Omega(r)$ of the local symmetry group for each lattice site r, such that the fields transform as

$$\begin{aligned} \psi(r) &\to \Omega(r)\psi(r) \\ \bar{\psi}(r) &\to \bar{\psi}(r)\Omega(r)^\dagger\,. \end{aligned} \tag{2.3.7}$$

When applying this gauge transformation, we find that the mass term is left invariant, as in the continuum case, while the discretized derivative term is not. In fact, under this transformation, the term $\bar{\psi}(r)\psi(r+\hat{\mu})$ changes as

$$\bar{\psi}(r)\psi(r+\hat{\mu}) \to \bar{\psi}(r)\Omega(r)^\dagger\Omega(r+\hat{\mu})\psi(r+\hat{\mu})\,, \tag{2.3.8}$$

where the transformation matrices do not cancel each other, which results in this term not being gauge invariant. However, we can make this term invariant under this gauge transformation if we introduce a new field $U_\mu(r)$ in the Hamiltonian, between the two fermion fields, that transforms as

$$U_\mu(r) \to \Omega(r)U_\mu(r)\Omega(r+\hat{\mu})^\dagger\,. \tag{2.3.9}$$

This way, the derivative term now transforms as

$$\begin{aligned} \bar{\psi}(r)U_\mu(r)\psi(r+\hat{\mu}) &\to \bar{\psi}(r)\Omega(r)^\dagger\Omega(r)U_\mu(r)\Omega(r+\hat{\mu})^\dagger\Omega(r+\hat{\mu})\psi(r+\hat{\mu}) \\ &= \bar{\psi}(r)U_\mu(r)\psi(r+\hat{\mu})\,, \end{aligned} \tag{2.3.10}$$

and now the transformation matrices cancel each other, and this term is thus manifestly gauge-invariant.

Equation 2.3.9 shows that $U_\mu(r)$ transforms as an element of the symmetry group considered. Moreover, because of the way this field appears in the Hamiltonian, it can be viewed as belonging to the link connecting lattice sites r and $r+\hat{\mu}$ and being oriented in the μ direction, which is why these are referred to as *link variables*. A representation of the link variable can be seen in figure 2.1

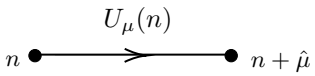

Figure 2.1: The link variable $U_\mu(x)$ connecting lattice sites n and $n+\hat{\mu}$.

Given that the link variables are oriented, we can also consider link variables in the opposite direction, connecting the lattice sites r and $r - \hat{\mu}$ defined as

$$U_{-\mu}(r) = U_{\mu}^{\dagger}(r - \hat{\mu}) \,, \tag{2.3.11}$$

which transform as

$$U_{-\mu}(r) \to \Omega(r) U_{-\mu}(r) \Omega(r - \hat{\mu})^{\dagger} \,. \tag{2.3.12}$$

In the continuum, the gauge transporter, $G(x, y)$ transforms in the same way as the link variables. It is given by the exponential of the path-ordered integral of the gauge field A along a curve $\mathcal{C}$ connecting two points x and y,

$$G(x, y) = P \exp\left(ig \int_{\mathcal{C}} A \cdot \mathrm{d}s \right) \,, \tag{2.3.13}$$

where g is the gauge coupling. This quantity has the same transformation properties as the link variables, transforming as

$$G(x, y) \to \Omega(x) G(x, y) \Omega(y)^{\dagger} \,. \tag{2.3.14}$$

We can interpret the link variables, $U_{\mu}(r)$ as the lattice version of the gauge transporter by defining the gauge variable on a link $A_{\mu}(r)$ as

$$A_{\mu}(r) = \frac{1}{a} \int_{r}^{r+\mu} A \cdot \mathrm{d}s \,. \tag{2.3.15}$$

Thus, we can define the link variables as

$$U_{\mu}(r) = \exp\left(iga A_{\mu}(r) \right) \,, \tag{2.3.16}$$

which shows that the link variables are the lattice counterpart of the gauge fields.

Having defined the link variables and their transformation properties, we can now write the fermion Hamiltonian on the lattice as

$$H_F = a^3 \sum_{r \in \Lambda} \bar{\psi}(r) \left(\sum_{\mu=1}^{3} i\gamma_{\mu} \frac{U_{\mu}(r)\psi(r + \hat{\mu}) - U_{-\mu}(r)\psi(r - \hat{\mu})}{2a} + m\psi(r) \right) \,. \tag{2.3.17}$$

2.3.2 Gauge Field Hamiltonian

The lattice counterpart of the gauge fields are the link variables. As such, in order to build the gauge field Hamiltonian, we need to construct a quantity composed by link variables, that is gauge invariant.

A quantity that we can construct in such a way is the ordered product of link variables, forming a path between two lattice sites, labeled by r_0 and r_1, given by

$$P[U] = U_{\mu_0}(r_0)\, U_{\mu_1}(r_0 + \hat{\mu}_0) \ldots U_{\mu_{k-1}}(r_1 - \hat{\mu}_{k-1}) \ . \tag{2.3.18}$$

Since the link variables transform as shown in equation 2.3.9, applying the gauge transformation to the path $P[U]$, the transformation matrices arising between two adjacent links will cancel such that only the first and last one remains. Then, $P[U]$ transforms as

$$P[U] \to \Omega(r_0)\, P[U] \Omega(r_1)^\dagger \ , \tag{2.3.19}$$

and we can see that this quantity is not gauge invariant. In order to construct a gauge invariant quantity, we start by considering a closed path, $P_C[U]$, that is, instead of the path $P[U]$ between two lattice sites, we consider a path ending in the same lattice site as it started, such that it transforms as

$$P_C[U] \to \Omega(r)\, P_C[U] \Omega(r)^\dagger \ . \tag{2.3.20}$$

Then, we take the trace of this path, $L[U] = \mathrm{tr}\,[P[U]]$ so that we can take advantage of the invariance of the trace under cyclic permutations to cancel the two transformation matrices in equation 2.3.20 with each other. In fact, this quantity will transform as

$$\begin{aligned} L[U] = \mathrm{tr}\,[P[U]] &\to \mathrm{tr}\left[\Omega(n) P[U] \Omega(r)^\dagger\right] \\ &= \mathrm{tr}\left[P[U] \Omega(r)^\dagger \Omega(r)\right] = \mathrm{tr}\,[P[U]] = L[U]\,, \end{aligned} \tag{2.3.21}$$

which shows that it remains invariant under a gauge transformation, meaning that such a quantity, the trace of an ordered product of link variables around a closed path can be used to define the gauge field Hamiltonian on the lattice. Actually, in order to construct the counterpart of the continuum gauge field Hamiltonian, it is enough to use the *plaquette* [1], $\Pi_{\mu\nu}$, the shortest non-trivial closed path of link variables, shown in figure 2.2, defined as

$$\begin{aligned} \Pi_{\mu\nu}(r) &= U_\mu(r) U_\nu(r + \hat{\mu}) U_{-\mu}(r + \hat{\mu} + \hat{\nu}) U_{-\nu}(r + \hat{\nu}) \\ &= U_\mu(r) U_\nu(r + \hat{\mu}) U_\mu(r + \hat{\nu})^\dagger U_\nu(r)^\dagger \,. \end{aligned} \tag{2.3.22}$$

Since the link variables $U_\mu(r)$ commute with each other, such a term is not enough to produce nontrivial dynamics. In order to construct another term for the Hamiltonian, we can make an analogy between our system and a system of coupled rigid rotors.

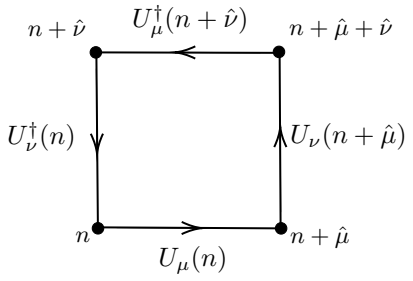

Figure 2.2: The plaquette $\Pi_{\mu\nu}(n)$ is defined at each lattice site as the product of link variables $U_\mu(n)$ oriented around an elementary square.

Rigid Rotor

The gauge degree of freedom is encoded in the link variables, $U_\mu(r)$, which are elements of the symmetry group considered. Let's consider as a symmetry group the group $\mathrm{O}(3)$, which generates rotations in 3 dimensions. In this setting, each link can be seen as a rigid rotor, and the link variables can be parametrized as

$$U_j = e^{i\vec{T}_j \cdot \vec{\Omega}}\,, \tag{2.3.23}$$

where $\vec{T}_j$ is a vector with the representation matrices of the generators of the rotation group for angular momentum j, and $\vec{\Omega}$ is a vector with the rotation angles. The Hamiltonian for the rigid rotor can be written as

$$H = \frac{1}{2} I \omega^2\,, \tag{2.3.24}$$

where $\vec{\omega} = \frac{d\vec{\Omega}}{dt}$ is the angular velocity, and I is the moment of inertia of the rigid rotor.

As each link can be seen as a rigid rotor, the Hamiltonian will include a sum of terms as the one in equation 2.3.24 for each lattice link. These terms are related to the rotation of the link variables in the given symmetry group.

In general, link variables can rotate in the symmetry group considered, and as such, we can include in the Hamiltonian a term of the form of equation 2.3.24 for each lattice link, built from the operator $n_\mu(r)$ conjugate to $U_\mu(r)$, written as[4]

$$\frac{1}{2} \sum_{r,\mu} (n_\mu(r))^2\,. \tag{2.3.25}$$

With these two terms, we can write the gauge field Hamiltonian as

$$H_G = \frac{U}{2} \sum_{r\in\Lambda} \sum_{\mu=1}^{3} (n_\mu(r))^2 - K \sum_{r\in\Lambda} \sum_{\substack{\mu,\nu=1 \\ \mu<\nu}}^{3} \mathrm{Re}\left[\mathrm{tr}\left(U_\mu(r) U_\nu(r+\hat{\mu}) U_\mu(r+\hat{\nu})^\dagger U_\nu(r)^\dagger\right)\right]\,. \tag{2.3.26}$$

Retrieving our analogy between lattice gauge theory and a system of coupled rigid rotors, we can interpret the first term in this Hamiltonian as the one responsible for the rotation of each link variable in the gauge group, and the second one as the term coupling different link variables.

Pure U(1) Lattice Gauge Theory

In this work, we will be interested in the case of the $U(1)$ lattice gauge theory, without fermions.

For this symmetry group, the link variables $U_\mu(r)$ correspond to a complex number with a given phase, $U_\mu(r) = e^{i\phi_\mu(r)}$, so the plaquette becomes

$$
\begin{aligned}
\Pi_{\mu\nu}(r) &= U_\mu(r)U_\nu(r+\hat{\mu})U_\mu^\dagger(r+\hat{\nu})U_\nu^\dagger(r) \\
&= e^{i\phi_\mu(r)}e^{i\phi_\nu(r+\hat{\mu})}e^{-i\phi_\mu(r+\hat{\nu})}e^{-i\phi_\nu(r)} \\
&= e^{i(\phi_\mu(r)+\phi_\nu(r+\hat{\mu})-\phi_\mu(r+\hat{\nu})-\phi_\nu(r))} \\
&= e^{i\Theta_{\mu\nu}(r)}\,,
\end{aligned}
\tag{2.3.27}
$$

where $\Theta_{\mu\nu}(r)$ is the phase of the plaquette $\Pi_{\mu\nu}(r)$. Then, the Hamiltonian in equation 2.3.26 can be written as

$$
H = \frac{U}{2}\sum_{r,\mu}\left(n_\mu(r)\right)^2 - K\sum_{r,\mu<\nu}\cos\left[\phi_\mu(r)+\phi_\nu(r+\mu)-\phi_\mu\left(r+\nu\right)-\phi_\nu(r)\right]\,. \tag{2.3.28}
$$

The two terms of this Hamiltonian can be interpreted in analogy with the eletrodynamics Hamiltonian. The link variable $U_\mu(r)$ is given by equation 2.3.16, so we have the relation $\phi_\mu(r) = gaA_\mu(r)$ between the phase $\phi_\mu(n)$ and the gauge field $A_\mu(n)$, which in $\mathrm{U}(1)$ is the electromagnetic four-potential. As such, in the continuum limit, performing a Taylor expansion on the second term, the sum over the spatial plaquettes becomes the square of the curl of the magnetic potential. Then, the second term of the Hamiltonian is the lattice form of the magnetic field squared. The operator $n_\mu(r)$, as the canonical momenta conjugated to $\phi_\mu(r)$, corresponds to the electric field flux through link $r+\hat{\mu}$, and as such, the first term of the Hamiltonian represents the electric field squared.

2.3.3 Derivation of the action

We now proceed to derive the action for the $U(1)$ lattice gauge theory, from the Hamiltonian in equation 2.3.28. The Hilbert space is spanned by the states $|\phi\rangle = \otimes_{r,\mu}|\phi_\mu(r)\rangle$ or $|n\rangle = \otimes_{r,\mu}|n_\mu(r)\rangle$ such that

$$
e^{i\hat{\phi}_\mu(r)}|\phi\rangle = e^{i\phi_\mu(r)}|\phi\rangle, \quad \hat{n}_\mu(r)|n\rangle = n_\mu(r)|n\rangle\,. \tag{2.3.29}
$$

Using the notation $\frac{d\phi}{2\pi} = \left[\prod_{r,\mu}\frac{d\phi_\mu(r)}{2\pi}\right]$, $\sum_n = \left[\prod_{r,\mu}\sum_{n_\mu(r)}\right]$, $2\pi\delta\left(\phi-\phi'\right) = \prod_{r,\mu}2\pi\delta\left(\phi_\mu(r)-\phi'_\mu(r)\right)$ and $\delta_{n,n'} = \prod_{r,\mu}\delta_{n_\mu(r),n'_\mu(r)}$, we can define the following properties

$$
\begin{aligned}
\langle\phi \mid n\rangle &= e^{i\sum_{r\mu}\phi_\mu(r)n_\mu(r)} \\
\langle\phi \mid \phi'\rangle &= 2\pi\delta\left(\phi-\phi'\right) \\
\langle n \mid n'\rangle &= \delta_{n,n'} \\
\int\frac{d\phi}{2\pi}|\phi\rangle\langle\phi| &= \sum_l |n\rangle\langle n| = 1\,.
\end{aligned}
\tag{2.3.30}
$$

As the operator $\hat{n}_\mu(r)$ corresponds to the lattice version of the electric field flux through the link $r+\hat{\mu}$, the counterpart of the Gauss law on the lattice is that the charge, q, on a lattice site r is given by the sum of the electric flux through the links connected to site r, given by the $\hat{n}_\mu(r)$ operators as

$$
\hat{Q}_r = \sum_\mu\left[\hat{n}_\mu(r)+\hat{n}_\mu(r-\hat{\mu})\right] = q\,. \tag{2.3.31}
$$

We are interested in studying the $\mathrm{U}(1)$ LGT without charges, so we consider the projector to this subspace of the Hilbert space, written as

$$P = \prod_r \delta_{\hat{Q}_r,0} = \int \prod_r \frac{d\theta(r)}{2\pi} e^{i\sum_r \hat{Q}_r \theta(r)}\,, \tag{2.3.32}$$

which has the properties $P^2 = P$ and $[P, H] = 0$. Thus, the partition function is given by

$$Z = \mathrm{tr}[e^{-\beta H} P]\,. \tag{2.3.33}$$

In order to numerically simulate this theory, we perform a Trotter decomposition, by separating the partition function Z into N time intervals, with a temporal extent $\Delta\tau = \beta/N$. Up to terms of order $\Delta\tau$, we can then write the partition function as

$$Z = \mathrm{tr}\left[e^{-\beta H} P\right] = \mathrm{tr}\left[\left(e^{-\frac{\beta}{N} H} P\right)^N\right] = \int D\phi \prod_{\tau=0}^{N-1} \left\langle \phi_\tau \left| e^{-\Delta\tau H} P \right| \phi_{\tau+1} \right\rangle\,, \tag{2.3.34}$$

where $D\phi = \prod_{\tau=0}^{N-1} \sum_{r,l} \frac{d\phi_\mu(\tau,r)}{2\pi}$. Separating the Hamiltonian into the parts containing operators $\hat{\phi}$ and $\hat{n}$, as $H = H_{\hat{n}} + H_{\hat{\phi}}$ and introducing a partition of the identity in $|n\rangle$, we have

$$\begin{aligned}
Z &= \int D\phi \prod_{\tau=0}^{N-1} \langle \phi_\tau | e^{-\Delta\tau H_{\hat{\phi}}} e^{-\Delta\tau H_{\hat{n}}} P | \phi_{\tau+1} \rangle + O(\Delta\tau) \\
&\simeq \int D\phi \sum_n \prod_{\tau=0}^{N-1} \langle \phi_\tau | e^{-\Delta\tau H_{\hat{\phi}}} | n_\tau \rangle \langle n_\tau | e^{-\Delta\tau H_{\hat{n}}} P | \phi_{\tau+1} \rangle \\
&= \int D\phi D\theta \sum_n \prod_{\tau=0}^{N-1} \langle \phi_\tau | e^{-\Delta\tau H_{\hat{\phi}}} | n_\tau \rangle \langle n_\tau | e^{-\Delta\tau H_{\hat{n}}} e^{i\sum_r \hat{Q}_r \theta(\tau,r)} | \phi_{\tau+1} \rangle \\
&= \int D\phi D\theta \sum_n \prod_{\tau=0}^{N-1} \langle \phi_\tau | e^{-\Delta\tau H_{\hat{\phi}}} | n_\tau \rangle \langle n_\tau | e^{-\Delta\tau H_{\hat{n}}} e^{i\sum_{r,\mu} [\hat{n}_\mu(\tau,r) + \hat{n}_{\tau,\mu}(r-\hat{\mu})]\theta(\tau,r)} | \phi_{\tau+1} \rangle\,,
\end{aligned} \tag{2.3.35}$$

where the sum in n in now given by $\sum_n = \prod_{\tau=0}^{N-1} \prod_{r,\mu} \sum_{n_\mu(\tau,r)}$ and we introduced the definition of the projector P with $D\theta = \prod_{\tau=0}^{N-1} \prod_r \frac{d\theta(\tau,r)}{2\pi}$ in the third line. In the last step, we used the Gauss law, given by equation 2.3.31. Then, by acting with the $\hat{\phi}$ and $\hat{n}$ operators on $\langle \phi_\tau |$ and on $\langle n_\tau |$, respectively, evaluating $\langle \phi_\tau | n_\tau \rangle$ and $\langle n_\tau | \phi_{\tau+1} \rangle$ according to equation 2.3.30 and noting that

$$\sum_{r,\mu} [n_\mu(\tau,r) + n_\mu(\tau, r-\hat{\mu})]\theta(\tau,r) = \sum_{r,\mu} n_\mu(\tau,r)[\theta(\tau,r) + \theta(\tau,r+\hat{\mu})]\,, \tag{2.3.36}$$

we finally obtain a partition function of the form

$$Z = \int D\phi D\theta \sum_n e^{-S[\phi,\theta,n]}\,, \tag{2.3.37}$$

with

$$
\begin{aligned}
S[\phi,\theta,n] = &- \Delta\tau K \sum_{\tau,r,\mu<\nu} \cos\left[\phi_\mu(\tau,r) - \phi_\nu(\tau,r+\hat{\mu}) + \phi_\mu\left(\tau,r+\hat{\nu}\right) - \phi_\nu(\tau,r)\right] \\
&- i \sum_{\tau,r,\mu} \left[\phi_\mu(\tau,r) - \phi_\mu(\tau+1,r) + \theta(\tau,r) + \theta(\tau,r+\hat{\mu})\right] n_\mu(\tau,r) \\
&+ \Delta\tau \frac{U}{2} \sum_{\tau,r,\mu} \left[n_\mu(\tau,r)\right]^2 .
\end{aligned}
\tag{2.3.38}
$$

In order to identify this action with a theory on a $(3+1)\mathcal{D}$ lattice, we identify $\hat{\theta}(\tau,r)$ with the phase of a link variable in the temporal direction, as $\hat{\theta}(\tau,r) = -\hat{\phi_0}(\tau,r)$ and $\hat{\theta}(\tau,r+\hat{\mu}) = \hat{\phi_0}(\tau,r+\hat{\mu})$, so that the the second term in equation 2.3.38 corresponds to the phase of a space-time plaquette. Then, we can write the action as

$$
\begin{aligned}
S[\phi,n] = &- \Delta\tau K \sum_{\tau,r,\mu<\nu} \cos\left[\phi_\mu(\tau,r) + \phi_\nu(\tau,r+\hat{\mu}) - \phi_\mu(\tau,r+\hat{\nu}) - \phi_\nu(\tau,r)\right] \\
&- i \sum_{\tau,r,\mu} \left[\phi_\mu(\tau,r) + \phi_0(\tau,r+\hat{\mu}) - \phi_\mu(\tau+1,r) - \phi_0(\tau,r)\right] n_\mu(\tau,r) \\
&+ \Delta\tau \frac{U}{2} \sum_{\tau,r,\mu} \left[n_\mu(\tau,r)\right]^2 ,
\end{aligned}
\tag{2.3.39}
$$

so that the partition function is given by

$$
Z = \int D\phi \sum_l e^{-S[\phi,n]} .
\tag{2.3.40}
$$

We can approximate the sum in n in the partition function in equation 2.3.40 for $\Delta\tau U \gg 1$ using the Villain approximation[5], given by

$$
e^{z\cos(\Phi)} = \sum_n I_n(z) e^{in\Phi} \simeq \sum_n e^{-\frac{1}{2z}n^2 + i\Phi n} ,
\tag{2.3.41}
$$

which is valid for $z \gg 1$. Then, we obtain the approximated partition function, given by

$$
Z = \int D\phi e^{-S[\phi]} ,
\tag{2.3.42}
$$

with the action $S[\phi]$ given by

$$
\begin{aligned}
S[\phi] = &- \Delta\tau K \sum_{\tau,r,\mu<\nu} \cos\left[\phi_\mu(\tau,r) + \phi_\nu(\tau,r+\hat{\mu}) - \phi_\mu(\tau,r+\nu) - \phi_\nu(\tau,r)\right] \\
&- \frac{1}{\Delta\tau U} \sum_{\tau,r,\mu} \cos\left[\phi_\mu(\tau,r) + \phi_0(\tau,r+\hat{\mu}) - \phi_\mu(\tau+1,r) - \phi_0(\tau,r)\right] .
\end{aligned}
\tag{2.3.43}
$$

Finally, we can relabel the spacetime lattice coordinates as $n = (\tau,r)$ with directions $\mu,\nu = (0,1,2,3)$ with $\mu = 0$ for the temporal direction in order to write the action as

$$
\begin{aligned}
S[\phi] = &- \Delta\tau K \sum_{n,\mu<\nu} \cos\left[\phi_\mu(n) + \phi_\nu(n+\hat{\mu}) - \phi_\mu(n+\hat{\nu}) - \phi_\nu(n)\right] \\
&- \frac{1}{\Delta\tau U} \sum_{n,\mu} \cos\left[\phi_\mu(n) + \phi_0(n+\hat{\mu}) - \phi_\mu(n+e_0) - \phi_0(n)\right] .
\end{aligned}
\tag{2.3.44}
$$

This is the canonical action for the $\mathrm{U}(1)$ lattice gauge theory. In simulations of lattice gauge theory, it is usual to set the coupling of the spatial and space-time parts of the action equal, as $\Delta\tau K = \frac{1}{\Delta\tau U} = \beta$, and write the action for the *isotropic* $\mathrm{U}(1)$ lattice gauge theory as

$$S[\phi] = -\beta \sum_{n,\mu<\nu} \cos\left[\phi_\mu(n) + \phi_\nu(n+\hat{\mu}) - \phi_\mu(n+\hat{\nu}) - \phi_\nu(n)\right] , \tag{2.3.45}$$

where β is the *coupling parameter*. Alternatively, we can treat spatial and temporal lattice directions differently, by introducing an *anisotropy parameter* ξ in the action, and write it as [6]

$$\begin{aligned} S[\phi] = &-\frac{\beta}{\xi} \sum_{n,\mu<\nu} \cos\left[\phi_\mu(n) + \phi_\nu(n+\hat{\mu}) - \phi_\mu(n+\hat{\nu}) - \phi_\nu(n)\right] \\ &- \beta\xi \sum_{n,\mu} \cos\left[\phi_\mu(n) + \phi_0(n+\hat{\mu}) - \phi_\mu(n+e_0) - \phi_0(n)\right] . \end{aligned} \tag{2.3.46}$$

2.3.4 Continuum limit

In order to check the validity of the action obtained in the lattice regularization, we must ensure that it approaches its continuum counterpart in the classical continuum limit, $a \to 0$. As the link variable $U_\mu(n)$ is given by equation 2.3.16, we have the relation $\phi_\mu(n) = gaA_\mu(n)$ between the phase $\phi_\mu(n)$ and the gauge field $A_\mu(n)$, with g the gauge coupling and a the lattice spacing. Replacing this in the action in equation 2.3.45, we get

$$S = -\beta \sum_{n,\mu<\nu} \cos\left[gaA_\mu(n) + gaA_\nu(n+e_\mu) - gaA_\mu(n+e_\nu) - gaA_\nu(n)\right] . \tag{2.3.47}$$

We can Taylor expand the gauge fields with shifted arguments as

$$A_\nu(n+e_\mu) = A_\nu(n) + a\partial_\mu A_\nu(n) + \mathcal{O}\left(a^2\right) , \tag{2.3.48}$$

so that the action becomes

$$\begin{aligned} S =& -\beta \sum_{n,\mu<\nu} \cos\left[gaA_\mu(n) + gaA_\nu(n) + ga^2\partial_\mu A_\nu(n) - gaA_\mu(n) - ga^2\partial_\nu A_\mu(n) - gaA_\nu(n)\right] \\ =& -\beta \sum_{n,\mu<\nu} \cos\left[ga^2\partial_\mu A_\nu(n) - ga^2\partial_\nu A_\mu(n)\right] \\ =& -\beta \sum_{n,\mu<\nu} \cos\left[ga^2 F_{\mu\nu}(n)\right] . \end{aligned} \tag{2.3.49}$$

We can then perform a Taylor expansion in the cosine in the previous equation to obtain

$$S = -\beta \sum_{n,\mu<\nu} \left[1 + \frac{1}{2} g^2 a^4 F_{\mu\nu}^2(n)\right] . \tag{2.3.50}$$

In order to go to the continuum limit, we replace the sum over lattice sites with an integral over spacetime, as $a^4 \sum_n \to \int d^4x$. Then, after removing the constant term from the action, we obtain

$$S = -\frac{\beta g^2}{2} \int d^4x \sum_{\mu<\nu} F_{\mu\nu}^2(n) = -\frac{\beta g^2}{4} \int d^4x \sum_{\mu,\nu} F_{\mu\nu}^2(n)\,, \tag{2.3.51}$$

where we used $\sum_{\mu<\nu} F_{\mu\nu}^2 = \frac{1}{2}\sum_{\mu,\nu} F_{\mu\nu}^2$. Equation 2.3.51 is the usual pure $\mathrm{U}(1)$ gauge theory action if we identify

$$\beta = \frac{2}{g^2}\,. \tag{2.3.52}$$

If we take the continuum limit of the anisotropic action in equation 2.3.46 in the same way, we again find the usual pure $\mathrm{U}(1)$ gauge action in the continuum if we also identify

$$\xi = \frac{a_s}{a_t}\,. \tag{2.3.53}$$

2.4 Observables

The ultimate goal of discretizing the continuum gauge theory to a lattice was to make it finite and computable. Having defined the partition function for the $\mathrm{U}(1)$ pure gauge theory in the lattice, we can now compute observables. The average value of an observable $\hat{O}$ on the lattice is given by

$$\langle \hat{O} \rangle = \frac{1}{Z} \int \mathrm{e}^{-S[U]} O[U] \mathcal{D}[U]\,, \tag{2.4.1}$$

where $O[U]$ is a gauge invariant functional of lattice links U obeying

$$O[U] = O\left[\Omega U \Omega^\dagger\right] = O\left[U'\right]\,. \tag{2.4.2}$$

As we have seen when constructing the gauge field Hamiltonian in section 2.3.2, such a quantity is the trace of an ordered product of link variables across a closed loop. Indeed these traced loops of link variables can be used to construct observables on the lattice. One example is the plaquette, $U_{\mu\nu}$ which is a trace of the ordered product of link variables over the elemental square, defined in equation 2.3.22.

Other observables can be constructed as the trace of an ordered product of link variables over a closed loop, as these will be gauge invariant. One such observable is the *Wilson loop* composed of two *Wilson lines* and two *temporal transporters*. The Wilson line $S(r_1, r_2, n_t)$ is an ordered product of spatial link variables at time slice n_t connecting two lattice points (r_1, n_t) and (r_2, n_t) along a path $\mathcal{C}(r_1, r_2)$, defined as

$$S\left(r_1, r_2, n_t\right) = \prod_{(r,j)\in\mathcal{C}(r_1,r_2)} U_j\left(r, n_t\right)\,. \tag{2.4.3}$$

The temporal transporter is a product of temporal link variables along a straight line connecting lattice points $(r, 0)$ and (r, n_t), given by

$$T\left(r, n_t\right) = \prod_{j=0}^{n_t-1} U_0(r, j)\,. \tag{2.4.4}$$

By considering the trace of the product of two Wilson lines and two temporal transporters, we can define the gauge invariant Wilson loop as

$$W_{\mathcal{L}}[U] = \mathrm{tr}\left[S\left(r_1, r_2, n_t\right) T\left(r_2, n_t\right)^{\dagger} S(r_1, r_2, 0)^{\dagger} T\left(r_1, n_t\right)\right] = \mathrm{tr}\left[\prod_{(n,\mu)\in\mathcal{L}} U_\mu(n)\right]\,. \tag{2.4.5}$$

If we consider the Wilson loop with temporal transporters extending over the full temporal size of the lattice, then the Wilson lines will be on the same path, because of periodic boundary conditions, but will be in opposite directions, and, as such, they cancel out. The Wilson loop then reduces to the product of two temporal transporters over the full extent of the temporal direction and at different spatial positions.Because of the periodic boundary conditions, each of the temporal transporters is now defined on a closed loop. We can then define a new observable by taking the trace of each of the temporal transporters, the *Polyakov loop*, defined as

$$P(r) = \mathrm{tr}\left[\prod_{j=0}^{N_T-1} U_0(r, j)\right]\,. \tag{2.4.6}$$

2.4.1 Potential

In order to relate the Wilson loop and the Polyakov loop to physical meaningful quantities, we will begin by looking at the Wilson loop in the temporal gauge. A description of gauge fixing and in particular, of the temporal gauge can be found in appendix A. The temporal gauge is given by

$$U_0(n) = \mathbb{1}, \forall n\,. \tag{2.4.7}$$

In this gauge, the temporal transporters in the definition of the Wilson loop become trivial,

$$T\left(r, n_t\right) = \prod_{j=0}^{n_t-1} U_0(r, j) = \mathbb{1}\,. \tag{2.4.8}$$

Since the expectation value of an observable is gauge invariant, we have

$$\langle W_{\mathcal{L}}\rangle = \langle W_{\mathcal{L}}\rangle_{\text{temp}} = \left\langle \mathrm{tr}\left[S\left(r_1, r_2, n_t\right) S(r_1, r_2, 0)^{\dagger}\right]\right\rangle_{\text{temp}}\,, \tag{2.4.9}$$

where $\langle\rangle_{temp}$ denotes the expectation value calculated in the temporal gauge. As such, we can see the Wilson loop as a correlator between two Wilson lines on temporal slices separated by n_t lattice spacings. A description of euclidean correlators between two observables can be found in appendix B .We can evaluate this euclidian correlator as

$$\left\langle \mathrm{tr}\left[S\left(r_1,r_2,n_t\right)S(r_1,r_2,0)^\dagger\right]\right\rangle_{\mathrm{temp}} = \sum_k \left\langle 0\left|\widehat{S}(r_1,r_2,n_t)\right|k\right\rangle \left\langle k\left|\widehat{S}(r_1,r_2,0)^\dagger\right|0\right\rangle \mathrm{e}^{-tE_k}\,. \tag{2.4.10}$$

As an ordered product of link variables, the transformation properties of $S(r_1,r_2,n_t)$ under a gauge transformation depend only on the first and last link variables of the product and, as in equation 2.3.20, we have

$$S(r_1,r_2,n_t) \to \Omega(r_1,n_t)S(r_1,r_2,n_t)\Omega(r_2,nt)^\dagger\,. \tag{2.4.11}$$

This quantity has the same transformation properties of a fermion-antifermion pair, $\psi(r_1)\bar{\psi}(r_2)$, which, according to equation 2.3.7, transform as

$$\psi(r_1)\bar{\psi}(r_2) \to \Omega(r_1)\psi(r_1)\bar{\psi}(r_2)\Omega(r_2)^\dagger\,. \tag{2.4.12}$$

In fact, the propagator of a fermion in the limit of large charge is given by $S(r_1,r_2,n_t)$ [2], so that $S(r_1,r_2,n_t)$ indeed describes a fermion-antifermion pair.

Then, the states $|n\rangle$ that have a non-vanishing overlap with $\langle 0|S(r_1,r_2,n_t)$ and thus contribute to the sum in equation 2.4.10 are the states describing a static fermion-antifermion pair. As such, the energy E_k is the energy of the fermion-antifermion state $S^\dagger(r_1,r_2,n_t)|0\rangle$, which corresponds to the potential between a static fermion-antifermion pair, separated by distance $r = a|r_1 - r_2|$. Inserting this result in equation 2.4.9, we can write

$$\langle W_{\mathcal{L}}[U]\rangle \propto e^{-n_t a V(r)}(1+\mathcal{O}(e^{-n_t a \Delta E}))\,, \tag{2.4.13}$$

where $V(r)$ denotes the potential and $\Delta E = E_2 - E_1$ is the energy difference between the fermion-antifermion pair and the first exited level of this state.

We can then relate the Wilson loop to the potential between a static fermion-antifermion pair and, in the limit of large n_t, i.e., for Wilson loops extending over large temporal distances, we can neglect the $\mathcal{O}(e^{-n_t a \Delta E})$ terms and use the Wilson loop to calculate the potential.

Similarly, since considering the Wilson loop over the full extent of the temporal direction reduces it to the product of two Polyakov loops in opposite directions, one at the spatial position r_1 and the other at r_2, we can express the same result in terms of a *Polyakov loop correlator* as

$$\langle P(r_1)P^\dagger(r_2)\rangle \propto e^{-N_t a V(r)}(1+\mathcal{O}(e^{-N_t a \Delta E}))\,, \tag{2.4.14}$$

and calculate the potential using the Polyakov loop. The Polyakov loop correlator is illustrated in figure 2.3.

These observables will be revisited in chapter 5. The process of numerically evaluating the average value of observables on the lattice is described in chapter 4.

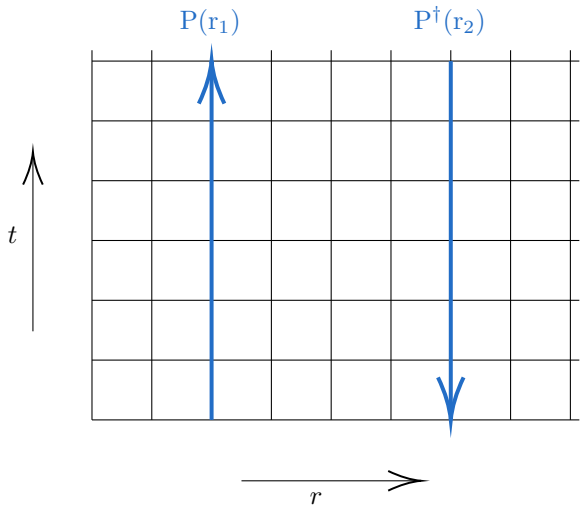

Figure 2.3: A representation of the Polyakov loop correlator. The Polyakov loop at r_1 and the anti-Polyakov loop at r_2 are related, respectively, to the propagator of a charge and an anti-charge. As such, this situation can be interpreted as having a charge at r_1 and an anti-charge at r_2, and we can thus use the Polyakov loop correlator to determin the Potential between these two charges.

2.5 Temperature

Since we want to study the phases of this theory at different temperatures, we need a way to control the temperature of the system. In order to do this, we take advantage of the analogy between the partition function given in terms of the euclidean path integral formulation, and the partition function given in terms of the canonical ensamble of statistical physics.

From the path integral formulation we have

$$Z = \mathrm{tr}\left[e^{-T_E H}\right] , \tag{2.5.1}$$

where T_E denotes the extent in the euclidean time direction and H the Hamiltonian.

From statistical physics, we have that the partition function in given by

$$Z = \mathrm{tr}\left[e^{-\beta H}\right] , \tag{2.5.2}$$

where $\beta = 1/Tk_B$, with T the temperature and k_B the Boltzmann factor.

By matching equations 2.5.1 and 2.5.2, we can identify β with the lattice temporal temporal extent,

$$\beta = T_E \, . \tag{2.5.3}$$

On the lattice, the temporal extent is given by the product of the temporal lattice spacing with the number of points in the temporal direction, $T_E = a_t N_t$. Setting $k_B = 1$, we find that the temperature is related to the temporal lattice spacing and the lattice time extent as

$$\frac{1}{T} = a_t N_t \Leftrightarrow T = \frac{1}{a_t N_t} \, . \tag{2.5.4}$$

Chapter 3

U(1) Lattice Gauge Theory

In this chapter, we briefly review some aspects of the $\mathrm{U}(1)$ lattice gauge theory. In particular, we look at the phases of this theory in the strong and weak coupling regimes, the phase transition between these phases, and the order parameter distinguishing them, making reference to literature results regarding these topics.

3.1 Strong Coupling Limit

In order to look into the behaviour of the $\mathrm{U}(1)$ LGT in $(3+1)\mathcal{D}$ in the strong coupling limit, let's first consider the simpler case of the 1 dimensional theory with a global $\mathrm{U}(1)$ symmetry. Following the derivation in the previous chapter, we can write the Hamiltonian for this theory as

$$H = \frac{U}{2}\sum_{r}\left(n(r)\right)^2 - K\sum_{r,\delta}\cos\left[\phi(r) - \phi\left(r+\delta\right)\right] . \tag{3.1.1}$$

The strong coupling approximation corresponds to taking $\beta \ll 1$, which, in terms of the Hamiltonian parameters corresponds to taking $U \gg K$. By looking at the previous Hamiltonian, we can see that in this limit, we can neglect the potential energy, and write the Hamiltonian as

$$H_0 = \frac{U}{2}\sum_{r}\left(n(r)\right)^2 . \tag{3.1.2}$$

The ground state of this Hamiltonian corresponds to having $n(r) = 0$ at all lattice sites, and the first exited state to taking $n(r) = \pm 1$ at one site in the 1 dimensional lattice, and as such, this theory has a gaped energy spectrum. We can map this theory to a system of rotors sitting at the sites of the $1\mathcal{D}$ lattice, each with angular momentum $n(r)$. Considering the Hamiltonian in equation 3.1.2, the rotors are decoupled, and as such, the first exited state corresponds to the excitation of one single rotor. When considering the second term of the Hamiltonian in equation 3.1.1, the rotors become coupled, and the excitation at one site can hop to other lattice sites. In the opposite limit, with $U \ll K$, the rotors become strongly coupled to each other and the gap of the energy spectrum disappears in the infinite volume limit. [7]

So, in the strong coupling limit, we have point like excitations at given positions on the lattice, which start hopping to other lattice sites as we move away from this limit. [7] When considering time propagation, these point like excitations form world-lines on the $(1+1)\mathcal{D}$ spacetime.

The situation for the $\mathrm{U}(1)$ lattice gauge theory is similar. The Hamiltonian for a $3\mathcal{D}$ lattice is given by

$$H = \frac{U}{2}\sum_{r,\mu}\left(n_\mu(r)\right)^2 - K\sum_{r,\mu<\nu}\cos\left[\phi_\mu(r)+\phi_\nu(r+\mu)-\phi_\mu\left(r+\nu\right)-\phi_\nu(r)\right]. \tag{3.1.3}$$

As before, considering the strong coupling limit, $U \gg K$ we can neglect the potential energy term in the Hamiltonian, and write it as

$$H_0 = \frac{U}{2}\sum_{r,\mu}\left(n_\mu(r)\right)^2. \tag{3.1.4}$$

As before, the ground state corresponds to having all $n_\mu(r)=0$. This operator now has a value for each lattice site, and for each direction, so we can think of it as belonging to the lattice links, instead of to the lattice sites. Unlike the previous case, here the excited states do not simply correspond to taking $n_\mu(r)\neq 0$ in one lattice link, as we must obey the condition $\sum_\mu\left[\hat{n}_\mu(r)+\hat{n}_\mu(r-\hat{\mu})\right]=q$, with $q=0$ for the case without charges. As such, taking $n_\mu(r)\neq 0$ for one lattice link, forces us to also take a finite value for the eigenstate of this operator on neighbouring links, in order to obey the restriction. Then, excited states correspond to closed loops on the lattice, so that at each lattice site the n are conserved. The energy of each state depends on the number of $n_\mu(r)\neq 0$, and as such, it is proportional to the length of the loop. In the $1\mathcal{D}$ case, point like excitations formed world lines when considering time propagation. In this case, excitations are closed loops forming world surfaces as we consider time propagation.

Taking the potential term in equation 3.1.3 into account, we have an effect similar to the previous case where point like excitations moved through the lattice. In this case, the loop acquires quasimomentum, and can also move trough the lattice. Another effect arising from considering the cosine term in the Hamiltonian is that this term can generate new loops, which alter the shape of the initial loop, and as such the state becomes a superposition of closed loops with different shapes. [7]

Physically, $n_\mu(r)$ corresponds to the electric flux through the link $r+\mu$. As such, these closed loops correspond to flux lines. In order to understand how charges behave in this limit, we consider the situation in which we introduce charges on the lattice. If we introduce two charges at two lattice sites, an electric flux line is generated between them. Since in this limit the energy of a state is proportional to the length of the flux lines, the energy of this state will be proportional to the distance between the charges, and as such, the system is said to be in the *confined phase*. In fact, this is the case also for non-abelian theories. Both abelian and non-abelian theories in the strong coupling regime exhibit linear confinement. [1] In $(2+1)\mathcal{D}$ $\mathrm{U}(1)$ LGT, the system is known to remain in this phase through all of the parameter space. [8] However, in $3+1$ dimensions, a phase transition occurs at some value of the gauge coupling to a phase in which the energy of such a state with two charges is the usual electric potential energy. [9, 10]

3.2 Weak Coupling Limit

In order to understand the behaviour of the theory in the weak coupling limit (large β), let's again start by looking at a simpler case, namely the model with a $\mathrm{U}(1)$ global symmetry on a $2\mathcal{D}$ lattice. The partition function of this model is given by

$$Z = \int D\phi \exp\left(-\beta \sum_{x,\delta} \cos\left[\phi(x) - \phi\left(x+\delta\right)\right]\right), \tag{3.2.1}$$

with the phases $\phi(x)$ defined at lattice sites. In the large β limit, we can Taylor expand the cosine in the action, and write the partition function as

$$Z = \int D\phi \exp\left(-\frac{\beta}{2} \sum_{x,\delta} \left[\phi(x) - \phi\left(x+\delta\right)\right]^2\right), \tag{3.2.2}$$

where we dropped the constant term appearing in the Taylor expansion. With the expansion, the partition function looses the periodicity of the cosine in the initial action in equation 3.2.1. In order to solve this, we can introduce an integer $n_\delta(x)$ at each link and allow jumps of $2\pi n_\delta(x)$ on the phases by writing the partition function as

$$Z = \sum_{n_\delta(x)} \int D\phi \exp\left(-\frac{\beta}{2} \sum_{x,\delta} \left[\phi(x) - \phi\left(x+\delta\right) + 2\pi n_\delta(x)\right]^2\right), \tag{3.2.3}$$

with $n_\delta(x)$ defined so that $\phi(x) - \phi(x+\delta) + 2\pi n_\delta(x)$ is in the interval $[-\pi, \pi]$. In equation 3.2.2, we lost the periodicity of the action by expanding around one well of the cosine. Introducing $n_\delta(x)$ restores the periodicity by allowing discrete jumps from one well to another. These variables can be related to vortices, by considering the sum of $n_\delta(x)$ around a closed loop. Taking an integer q_{x^*} defined at the centre of each plaquette, x^*, as

$$q_{x^*} = \sum_{\square} n_\delta(x) = n_1(x) + n_2(x+\hat{e}_1) - n_1(x+\hat{e}_2) - n_2(x)\,, \tag{3.2.4}$$

we can see that by circling around a point x^* with $q_{x^*} = 1$, we get a 2π phase jump in the phase variables.

Using this variable, the partition function of this model can be separated into a partition function for the phases and a patition function for the vortices [7].

$$Z = \prod_x \int D\phi \exp\left(-\frac{\beta}{2} \sum_{x,\delta} \left(\phi(x) - \phi(x+\delta)\right)^2\right) \sum_{q_{x^*}} \exp\left(-\frac{\beta}{2} \sum_{x^*,x^{*\prime}} \Delta^{-1}_{xx^\prime_*} q_{x^*} q_{x^*} 2\pi^2\right), \tag{3.2.5}$$

where $\Delta_{xx^\prime_*}$ is the inverse lattice Laplace operator. This partition function shows that the vortices q_{x^*} carry charge and interact through a Coulomb force [7]. In order to illustrate this, let's consider, as an example, the case of a single vortex at $x^* = 0$ with $q_0 = 1$. By definition, the sum of $B_\delta(x) = \phi(x) - \phi(x+\delta)$ around a closed loop (in this case around $x^* = 0$) is zero, i.e.,

$$\sum_{loop} B_\delta(x) = 0\,. \tag{3.2.6}$$

However, since we defined $n_\delta(x)$ such that $A_\delta(x) = \phi(x) - \phi(x+\delta) + 2\pi n_\delta(x)$ is in the interval $[-\pi, \pi]$, we have that the sum of $A_\delta(x)$ over a closed loop around $x^* = 0$ gives the vorticity q_0 as

$$\sum_{loop} A_\delta(x) = 2\pi q_0\,. \tag{3.2.7}$$

A picture of this unit vortex can be seen in figure 3.1 [7]. Here, the links intersected by the dashed line have $n_\delta(x) = 1$, while the remaining links have $n_\delta(x) = 0$. As we go around the vortex centre, the phases $\phi(x)$ have 2π jumps at the dashed line. In the continuum limit, the sums over closed paths become integrals over closed paths and the phases $\phi(x)$ can be seen as multivalued functions with a 2π jump at the dashed line and a branch point at the centre of the vortex.

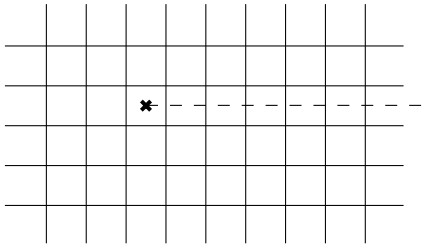

Figure 3.1: As we circle around the vortex marked by the $\times$ on the figure, the phases $\phi(x)$ have a 2π jump at the dashed line. Reproduced from [7].

If there is only one vortex, as represented in figure 3.1, the dashed line must continue to infinity. On a finite lattice, the dashed line cannot extend to infinity, and as such, it must end on another vortex, with a charge symmetric to the charge of the first one, i.e., an anti vortex.

According to the partition function in equation 3.2.5, for large values of β, the vortices are combined forming neutral dipoles, while in the opposite limit, the vortices are no longer combined and the system has a plasma of vortices [7]. This is a situation similar to the Kosterlitz–Thouless transition in the two dimensional XY model [11]. An analogous discussion can be made for the case of $\mathrm{U}(1)$ LGT [12].

3.2.1 Dirac Monopoles

In order to interpret the topological defects in $\mathrm{U}(1)$ LGT, it is convenient to briefly introduce the Dirac magnetic monopole [13].

According to Maxwell's equations, the divergence of the magnetic field is zero, $\vec{\nabla} \cdot \vec{B} = 0$. As such, a magnetic charge with a magnetic field given by

$$\vec{B}_m = q\frac{\vec{x}}{|\vec{x}|^3} \tag{3.2.8}$$

is not allowed. The way to reconcile an object with a magnetic field given by 3.2.8 is to introduce the *Dirac string*, a string of flux connecting the monopole to a source at infinity, such that the total flux of

magnetic field is zero. We can visualise the Dirac string as a very long and thin solenoid ranging from infinity to a point x. The magnetic field inside the solenoid is confined and, in the limit in which the solenoid in shrunk to a one dimensional string, the magnetic field at its endpoint at x is the magnetic field of an isolated charge, which corresponds to the magnetic monopole.

The total magnetic field of the monopole and the string is given by

$$\vec{B}_m = q\frac{\vec{x}}{|\vec{x}|^3} - 4q\pi\delta(x)\delta(y)\Theta(z)\,, \tag{3.2.9}$$

where $\delta(x)$ is the Dirac delta function and $\Theta(x)$ is the Heaviside function. In this equation, the first term is the magnetic Coulomb field of a monopole from equation 3.2.8, and the second term accounts for the magnetic field in the string.

The theory on the lattice gives a natural framework to construct Dirac monopoles and strings, as we will see in the following section. While in the continuum the energy of the Dirac string is infinite, on the lattice this problem is avoided and the string has zero energy. [12]

3.2.2 U(1) LGT

In three dimensional lattice gauge theory, we have a partition function analogous to the one in equation 3.2.1 bu with the phases on lattice sites replaced by phases of the link variables. We can express this partition function as

$$Z = \int D\phi \exp\left(-\beta \sum_{n,\mu<\nu} \cos\left[\Theta_{\mu\nu}\right]\right)\,, \tag{3.2.10}$$

where $\Theta_{\mu\nu}$ is the plaquette phase, defined as the sum of link phases around an elementary square in equation 2.3.22. Similarly to the previous case, we can Taylor expand the action around one well of the cosine. Then, in order to restore the periodicity of the action, we can add an integer $n_{\mu\nu}(x)$, which is now defined on the plaquette, so that the action can be written as

$$Z = \sum_{n_{\mu\nu}(x)} \int D\phi \exp\left(-\beta \sum_{n,\mu<\nu} \left(\Theta_{\mu\nu} + 2\pi n_{\mu\nu}(x)\right)^2\right)\,, \tag{3.2.11}$$

with $n_{\mu\nu}(x)$ such that $\Theta_{\mu\nu} + 2\pi n_{\mu\nu}(x)$ is in the interval $]\pi, \pi[$. As we saw in the previous chapter, $\Theta_{\mu\nu}$ is the lattice counterpart of the magnetic flux. As such, $n_{\mu\nu}(x)$ can be seen as a flux appearing due to the passage of a string through a plaquette. A string entering a cube through a plaquette, can either go out of the cube through another plaquette or have its endpoint inside the cube. In order for the flux to be conserved, if the string has its endpoint in a cube centered at x^*, the flux going into the cube must dissipate through its six faces. This is identified as a monopole. As such, by summing the $n_{\mu\nu}(x)$ variables around a cube, we can obtain the monopole charge, defined as

$$q_{x^*} = \sum_{cube} n_{\mu\nu}(x) \tag{3.2.12}$$

, where x^* denotes the centre of the cube.

Analogously to the previous case of a $\mathrm{U}(1)$ global symmetry, in this case we can write the partition function as a partition function for the free photons multiplied by a partition function for the monopoles, as [7]

$$Z = \prod_x \int D\phi \exp\left(-\frac{\beta}{2}\sum_{x,\delta}\left(\Pi_{\mu\nu}\right)^2\right)\sum_{q_{x^*}}\exp\left(-\frac{\beta}{2}\sum_{x^*,x^{*\prime}}\Delta^{-1}_{xx^{\prime}_*}q_{x^*}q_{x^*}2\pi^2\right), \tag{3.2.13}$$

where we can see that the monopoles behave like charges interacting through the Coulomb potential. In the large β limit, the monopoles are combined into neutral dipoles, formed by a monopole and an antimonopole connected by a string. How this leads to confinement of electric charges can be understood through an analogy with a type II superconductor in an external magnetic field. If the external magnetic field penetrates the superconductor, the particles in the vacuum, i.e., the electrons of the superconductor, establish electric currents which confine the magnetic field to a one dimensional flux tube. Similarly, in the $\mathrm{U}(1)$ gauge system at weak coupling, if a pair of electric charges is introduced in the vacuum, the vacuum particles, which in this case are the magnetic monopoles, establish magnetic currents which confine the electric field between the charges to a flux tube, which has constant energy, and thus leads to a linear potential, which corresponds to confinement. [14]

In the previous section, we saw that in the strong coupling limit, $\mathrm{U}(1)$ LGT was in the confined phase, with a potential between two charges depending linearly on the distance between them. For the 2 + 1 dimensional case, we found a similar situation in the opposite limit. As such, $(2+1)\mathcal{D}$ $\mathrm{U}(1)$ LGT is expected to remain in the phase where electric charges are confined through all the parameter space.

As we consider the theory in four dimensions, the instanton solutions of the $3\mathcal{D}$ case identified as monopoles in equation 3.2.9, which were point like, can now move in a fourth direction, and so, in $4\mathcal{D}$ they are manifested as a current and can be represented by a world line [7]. In order for the magnetic flux to be conserved, these lines have to extend to infinity or to form closed loops on the lattice. As in the $3\mathcal{D}$ case, we can separate the partition function for this system into a partition function for the loops of magnetic flux lines, and a partition function for free photons. In the weak coupling limit, $\beta \gg 1$, the closed loops of magnetic flux represent the world lines of the monopole-antimonopole pairs that appeared in $3\mathcal{D}$ at this limit. The contribution of such a loop to the action is proportional to its length and, as such, in the infrared limit, the magnetic flux lines have no influence on the system which can thus be described only by the free photons. As such, in this limit, the energy spectrum has no mass gap, and our theory can be described by massless photons, so that charged particles interact through a Coulomb interaction, as in QED.

In the strong coupling limit, we found that this system was in the confined phase. However, in the weak coupling limit in four dimensions, we expect charges to interact according to QED, with the potential between two electric charges being of the Coulomb form, instead of linear. Therefore, for some critical value of the coupling parameter, β_c, we expect to find a phase transition such that for $\beta < \beta_c$ the system is in the confined phase and for $\beta > \beta_c$ the system is in the *Coulomb phase*.

3.3 Phase Transition

The distinguishing feature between the confining and non-confining phases is the potential, which should grow linearly with distance in the former case and should be of the Coulomb form in the latter. As such, we can distinguish between these two phases by calculating the potential, through the Polyakov loop correlator, according to equation 2.4.14. According to the form of the potential in the two phases, we can parameterize it as [2]

$$V(r) = A + \frac{B}{r} + \sigma r \,, \tag{3.3.1}$$

where the first term is an irrelevant normalization to the energy, the second term is the Coulomb potential with strength B, and the last term is the linearly growing confining potential, with σ the *string tension*.

For large distances, the term σr dominates the potential. As such, if $\sigma \neq 0$, we have a linearly rising potential, corresponding to the confining phase. Only for $\sigma = 0$ do we have a Coulomb potential at large distances. Therefore, the string tension σ is an order parameter of our theory, distinguishing between the confining and non-confining phase.

At large distances, $a|r_1 - r_2| \to \infty$, we can factorize the Polyakov loop correlator in equation 2.4.14 as

$$\lim_{a|r_1-r_2|\to\infty} \left\langle P(r_1)P(r_2)^\dagger \right\rangle = \langle P(r_1)\rangle \left\langle P(r_2)^\dagger \right\rangle = |\langle P\rangle|^2 \,, \tag{3.3.2}$$

where in the last step, we replaced the expectation value of the Polyakov loop at a given position with the spatial average of this quantity, since the average value must be translational invariant.

In this limit, $a|r_1 - r_2| \to \infty$, the potential in the confining phase goes to infinity, while in the Coulomb phase, it approaches a constant value. Taking this into account and inserting the result of equation 3.3.2 into the definition of the Polyakov loop correlator in equation 2.4.14 at large distances, we note that, due to the linear growth of the potential, the Polyakov loop should have a zero expectation value, $\langle P\rangle = 0$ in the confined phase, while in the Coulomb phase, it should have a finite value, $\langle P\rangle \neq 0$. As such, the Polyakov loop is also an order parameter which allows us to distinguish between the two phases of the $\mathrm{U}(1)$ LGT.

By numerically simulating the $\mathrm{U}(1)$ LGT, with an action given by 2.3.45, for different values of N_t and β, we can determine the values of the critical coupling parameter, β_c, at which the phase transition occurs, and construct a phase diagram in terms of β and $\frac{1}{N_t}$, which is proportional to the temperature. Such a phase diagram can be found in the literature [15] and shows the phase boundary between the two phases of this theory. However, such calculations only allow the determination of the critical coupling parameter for a small number of sparsely separated temperatures, due to the limitation in selecting different finite values of N_t. As such, a complete phase diagram for the $\mathrm{U}(1)$ LGT is yet to be determined. One way to probe the parameter space more efficiently is to consider the anisotropic regularization of the $\mathrm{U}(1)$ LGT, and we will look at this in chapter 5.

3.4 Order of the Phase Transition

In the limit of zero temperature, $N_t \to \infty$, the transition from the confined to the Coulomb phase in $4\mathcal{D}$ $\mathrm{U}(1)$ LGT has been shown to be a first order transition at the critical value of the coupling parameter $\beta_c = 1.0111331(21)$ [15, 16].

In the opposite limit, considering $N_t = 1$, the Polyakov loop corresponds to a single temporal link variable, and as such, the temporal link variables are gauge invariant. In this limit, the spacetime plaquettes have the space links lying on top of each other, because of the periodic boundary conditions, and as such, these cancel out, and the plaquette becomes the product of two temporal link variables separaterd by one lattice spacing in the spatial direction. As such, the contribution of the spacetime plaquettes to the action is given by

$$S[\phi]_{temp} = -\beta \sum_{n,\mu} \cos\left[\phi_0(\tau, n + e_\mu) - \phi_0(n)\right] \ . \tag{3.4.1}$$

This is the action for a $3\mathcal{D}$ XY model, which is known to have a second order phase transition at $\beta_c = 0.45420(2)$ [17]. Then, we see that in the limiting case $N_t = 1$, the $4\mathcal{D}$ $U(1)$ LGT can be decomposed into a $U(1)$ LGT on a $3\mathcal{D}$ lattice, which is known to remain in the confined phase for all values of the gauge coupling, and a $3\mathcal{D}$ XY model.

Therefore, the theory we are interested in has a first order phase transition for $N_t \to \infty$ and a second order phase transition for $N_t = 1$, at different values of the coupling parameter, β. As such, a phase boundary connecting the two transition points is expected, along which the order of the phase transition must change, in order to reconcile the different orders of the phase transition at the limiting cases [18].

The order of the phase transition along the phase boundary has been investigated using different approaches, and it has been found that the phase transition of the $\mathrm{U}(1)$ LGT in $4\mathcal{D}$ is of first order for $N_t \geq 6$, becoming more weakly first order with decreasing N_t, and becomes second order for $N_t < 6$ [19].

Chapter 4

Markov Chain Monte Carlo

In this chapter, we review the numerical methods used throughout this work. We begin by introducing statistical sampling with the Monte Carlo method, then the generation of configurations according to a probability distribution with a Markov Chain, and finally the Metropolis-Hastings algorithm. We conclude with a description of the process of running the computational simulation for the $\mathrm{U}(1)$ LGT, and of techniques used for error estimation and variance reduction. Our description follows [2], [20] and [21].

4.1 Monte Carlo method

Physical systems usually have rather large phase spaces, which renders exact calculations impossible. One way to overcome this issue, is to consider the system's statistical behaviour, instead of trying to obtain analytical results. In lattice gauge theory, the expectation value of some observable is given by the functional integral

$$\langle O \rangle = \frac{1}{Z} \int \mathcal{D}[U] \mathrm{e}^{-S_G[U]} O[U] \,, \tag{4.1.1}$$

with

$$Z = \int \mathcal{D}[U] \mathrm{e}^{-S_G[U]} \,, \tag{4.1.2}$$

as explained in section 2.4. For large lattice sizes, this integral becomes impossible to evaluate analytically. As such, we can consider an estimator of the expectation value, $\langle O \rangle$, by sampling N states (configurations) of the lattice, U_n, computing the value of the observable O in each configuration, and considering the sample mean,

$$\langle O \rangle \approx \bar{O} = \frac{1}{N} \sum_{U_n} O\left[U_n\right] \,, \tag{4.1.3}$$

where the sum runs over configurations U_n distributed according to the Boltzmann probability distribution, $\exp(-S[U_n])$, and which has a variance

$$\sigma^2 = \langle (O - \langle O \rangle)^2 \rangle \,, \tag{4.1.4}$$

which we can estimate as

$$s^2 = \frac{1}{N-1} \sum_{U_n} (O[U_n] - \bar{O})^2 \,. \tag{4.1.5}$$

Therefore, provided we are able to sample a set of configurations according to the desired probability distribution, we can obtain an estimate of the expectation value of observables, given by equation 4.1.3, with an error $\epsilon = \sqrt{s^2/N}$.

4.1.1 Importance sampling

Using the Monte Carlo method, we can approximate the integral of some function $f(x)$ in an interval $x \in [a, b]$ by sampling N values of $f(x_n)$, with x_n randomly chosen in the interval of integration according to the uniform distribution $\rho_u(x) = \frac{1}{b-a}$, and then taking the sample mean as

$$\frac{1}{b-a} \int_a^b \mathrm{d}x f(x) = \langle f \rangle_{\rho_u} = \lim_{N \to \infty} \frac{1}{N} \sum_{n=1}^{N} f\left(x_n\right) \,. \tag{4.1.6}$$

When computing the estimator with this method, we must use a finite number N, which results in an associated error for the estimator of the order $1/\sqrt{N}$. The number of samples N is then chosen according to the accuracy we want to obtain. However, the number of samples, N required grows exponentially with the desired accuracy, and as such, a compromise must be made according to the available computational resources.

Using the Monte Carlo method with the uniform distribution, we are sampling uniformly through all the phase space, and thus, considering that all the regions of the phase diagram are of equal importance. However, in many physical systems, the dynamics are governed mainly by a small region of the phase space, and as such, we can use *importance sampling*, in order to reduce the variance of the estimators calculated by the Monte Carlo method. The expectation value of $f(x)$ with regard to a probability distribution $\rho(x)$ is given by

$$\langle f \rangle_\rho = \frac{\int_a^b \mathrm{d}x \rho(x) f(x)}{\int_a^b \mathrm{d}x \rho(x)} \,. \tag{4.1.7}$$

In importance sampling Monte Carlo, we sample x_n with the probability density $\rho(x)$ and estimate the average of $f(x)$ by calculating the value of $f(x_n)$ for each x_n as

$$\langle f \rangle_\rho = \lim_{N \to \infty} \frac{1}{N} \sum_{n=1}^{N} f\left(x_n\right) \,. \tag{4.1.8}$$

In LGT, we want to sample the lattice configurations, U_n according to the Boltzmann distribution, so we use the normalized probability density

$$\mathrm{d}P(U) = \frac{\mathrm{e}^{-S[U]}\mathcal{D}[U]}{\int \mathcal{D}[U]\mathrm{e}^{-S[U]}}\,, \tag{4.1.9}$$

and estimate the average value of an observable with equation 4.1.3.

In the following sections, we will discuss how to obtain the configurations, U_n, through a Markov chain method, in order to compute the estimators of the average observables, as well as techniques used in the simulations, and error reduction methods.

4.2 Markov Chain

A Markov chain is a stochastic process consisting of a sequence of configurations computed subsequently according to a certain probability rule.

Let $\mathbf{S} = \{S_1, S_2, \cdots, S_n\}$ be the set of possible sample states in the Markov chain. At every step t, the system assumes some state $X_t = S_i$. The index t is referred to as Markov- or Monte Carlo-time. A Markov process is characterized by the Markov Property, which states that the evolution of configurations only depends on the transition matrix, T, which encodes the probability of each state S_i to transition to another state S_j,with $T_{ij} = P(S_i \to S_j) = P(X_t = S_j | X_{t-1} = S_i)$. This property implies that the evolution of a Markov chain is independent of the past of the system, i.e., the next configuration, S_j, into which the system transitions depends solely on the present configuration, S_i, and not on the ones preceding it.

Since the entries of the transition matrix, T, are interpreted as transition probabilities, these also obey

$$0 \leq T_{ij} \leq 1, \quad \sum_j T_{ij} = 1\,. \tag{4.2.1}$$

We will only be interested in the case in which the Markov chain is time-homogeneous, that is, in the case in which the transition matrix T is the same for every Markov-time step.

The Markov chain is said to be *irreducible* if there are no non-communicating regions in the phase space, i.e, if there is a probability of going to any state S_j in a finite number of time steps, starting from any configuration S_i.

Furthermore, for a state S_i in the Markov chain has period p if the system can only come back to that state after a number of steps that is a multiple of p. If for every state, the period is $p = 1$, the Markov chain is called *aperiodic*. This condition is ensured if the diagonal elements of the transition matrix are positive, $T_{ii} \neq 0$.

A Markov chain that is irreducible and aperiodic is called *ergodic*.

The total probability that the system is in state S_j at Markov-time t, $P(X_t = S_j)$ is given by the sum over all states S_i of the transition probability from state S_i to state S_j, weighted by the probability of the system being in state S_i at time $t-1$, that is

$$P(X_t = S_j) = \sum_i P(X_t = S_j | X_{t-1} = S_i) P(X_{t-1} = S_i) = T_{ij} P(X_{t-1} = S_i)\,. \tag{4.2.2}$$

In order for this Markov process not to have sinks or sources of probability, the probability of the system going to state S_j in equation 4.2.2 must be equal to the probability of the system going out of state S_j, which is given by the sum of the transition probabilities from state S_j into state S_i, multiplied by the probability of the system being in state S_j at time t. Then, we must have

$$\sum_i T_{ij} P(X_{t-1} = S_i) = \sum_i T_{ji} P(X_t = S_j)\,. \tag{4.2.3}$$

Since, from the properties of transitions probabilities in equation 4.2.1, $\sum_i T_{ji} = 1$, the previous equation gives

$$\sum_i T_{ij} P(X_{t-1} = S_i) = P(X_t = S_j)\,. \tag{4.2.4}$$

This equation shows that there is an equilibrium distribution, for which the probability of the system being in state S_j is kept the same after successive applications of the matrix T, for each state S_j. if the Markov chain is irreducible, is can be shown that the equilibrium distribution is unique and, if it is also ergodic, the system will reach the equilibrium distribution regardless of the initial configuration. This is an important result, as it ensures that, when using an algorithm based on a ergodic Markov process, starting from any configuration, the system will equilibrate and reach an equilibrium distribution. As such, after reaching the equilibrium distribution, calculation Markov-time averages of observables is equivalent to calculating averages over all the configuration space. The process of reaching the equilibrium distribution is called *thermalization* and the way of determining when the system reaches equilibrium will be discussed in section 4.4.

A sufficient condition for equation 4.2.3 to be satisfied is the *detailed balanced condition*, which imposes that the arguments of the sums is equal for each terms,

$$T_{ij} P(X_{t-1} = S_i) = T_{ji} P(X_t = S_j)\,. \tag{4.2.5}$$

This condition than ensures that there exists a equilibrium distribution and is used my most algorithms, in particular by the ones we will be interested in.

4.3 Metropolis-Hastings Algorithm

The Metropolis-hasting algorithm [22, 23] is Markov chain Monte Carlo method for generating sequential configurations with a desired target distribution. This method provides a transition matrix that respects the detailed balance condition in equation 4.2.5, and thus the Markov chain will evolve to an equilibrium distribution, after which equilibrium configurations can be generated.

In LGT, the variables of interest are the links on a $(3+1)\mathrm{D}$ lattice with periodic boundary conditions.

We want to generate configurations with a target probability distribution proportional to the Boltzmann probability distribution, $e^{-S_G[U]}$, where $S_G[U]$ is the lattice gauge action defined in equation 2.3.45.

In $\mathrm{U}(1)$ LGT, the link variables are given by $U_n = e^{i\phi_n}$, so the configurations are defined by the link angles ϕ_n. As such, the algorithm for implementing the Metropolis-Hastings method for $\mathrm{U}(1)$ LGT consists in, for each link:

1. Generating a new value for the link angle, ϕ_n' according to a uniform random distribution;
2. Calculate the new value of the action, $S_G[U']$ with the proposed value for the new link variable;
3. Accept the new value for the link variable with a probability

$$P_{accept} = \min\left(1, \frac{e^{-S_G[U']}}{e^{-S_G[U]}}\right) . \tag{4.3.1}$$

4. If the new link variable is accepted, it replaces the old one. If not, the value of the link variable remains the same and we move one to the next iteration. Markov-time is incremented in any case.

In each iteration of the Metropolis-Hasting algorithm, this process is repeated for each link variable. Note that, because of the way the acceptance probability is defined, if the action calculated with the proposed new value for the link variable is equal or less than the initial one, the new link variable is always accepted as we will have $e^{-S_G[U']}/e^{-S_G[U]} \geq 1$.

We can now use this method to generate several configurations in order to calculate the estimator of the average values of the observables considered, according to equation 4.1.3. In order to do this calculation, the configurations considered must be taken after the equilibrium probability distribution is reached. This calculation also assumes that the configurations considered are uncorrelated, which is not the case for configurations generated with a Markov chain. How we ensure that these two conditions are satisfied will be the topic of the next sections.

In the $\mathrm{U}(1)$ LGT action in equation 2.3.45, we notice that the action for one link variable only depends on the plaquettes connected to it. Therefore, the lattice can be decomposed into even and odd sites, according to whether the sum of the coordinates, $x_0+x_1+x_2+x_3$, is even or odd and the system can be evolved system separately for each parity of sites. This way, each site block of a given parity is updated with respect to a constant background composed by the sites of opposite parity.

4.4 Running the simulation

4.4.1 Initialization

In order to start the simulation, an initial configuration must be chosen. As stated in the previous section, after enough Monte Carlo updates, any configuration we start with will evolve into a equilibrium configuration, which follows the thermal distribution. As such, any initial configuration can be taken. The two most common initial configurations correspond to the *cold start* and *hot start*.

In the cold start, the link variables are set to the identity element, which in $\mathrm{U}(1)$ corresponds to setting $U_n = 1$, or, equivalently, setting the link angle to zero, $\phi_n = 0$.

In the hot start, random values are taken for the initial link variables, following a uniform distribution, which in $\mathrm{U}(1)$ corresponds to taking random values for the value of ϕ_n in the interval $[-\pi, \pi]$.

The choice of the initial conditions can be made according to the region of the parameter space we are probing. For example, in the region of weak coupling (large β), the cold start configuration is closer to the equilibrium configuration, so the system will reach equilibrium in less Monte Carlo time. However, either start configuration will lead to equilibrium, after enough iterations. Throughout this work, cold start was used to initialize the simulations.

4.4.2 Thermalization

The Metropolis-Hastings algorithm sequentially updates the configuration on the lattice, starting from any configuration given. Eventually, a thermalized configuration is reached, which follows the equilibrium probability distribution, which is proportional to the Boltzmann distribution. In order to obtain the average value of observables, we can only use the configurations obtained after the system equilibrates. In order to determine when the system reaches equilibrium, we compute the average value of some observable after each Monte Carlo iteration, and evaluate how many iterations are necessary in order for the observable to reach a constant value.

The observable used to determine the thermalization time was the plaquette, introduced in equation 2.3.22. In figure 4.1, we show, as an example, the average value of the plaquette calculated after each iteration for an isotropic lattice with $\beta = 1$ at different system sizes. We found that after 2000 iterations the system is thermalized for all values of the coupling constant β and all system sizes. As such $N_{therm} = 2000$ was used, and the first 2000 configurations generated were discarded throughout this work, in order to ensure that all observables were calculated at equilibrium.

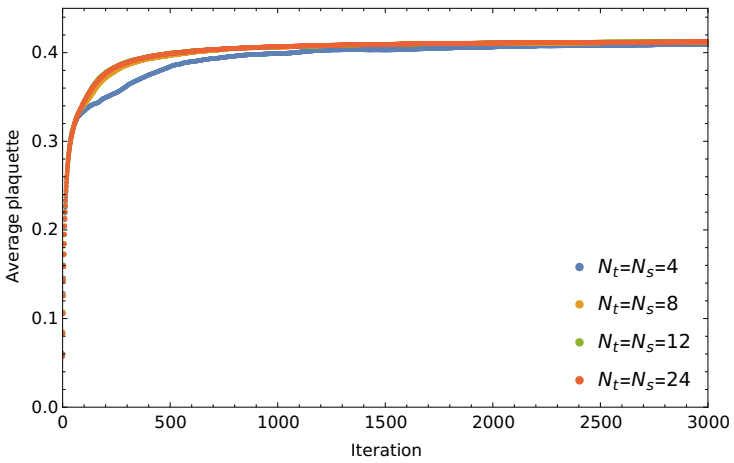

Figure 4.1: Average value of the plaquette calculated in an isotropic lattice with $\beta = 1$ at different system sizes. After 2000 iterations, the value of the average of the observable is stable, indicating that the system has reached equilibrium.

4.4.3 Autocorrelation

As the Metropolis-Hastings algorithm is a Markov process, which generates configurations sequentially, each configuration depends on the previous one. As such, there is a strong degree of correlation between the configurations generated. However, in order to estimate the value of observables through the Monte Carlo method, using equation 4.1.3, the configurations used must be uncorrelated from each other. After equilibrium is reached, the correlation between two configurations depends only on the Markov-time separating them. As such, in order to evaluate the correlation between the configurations generated, we consider the autocorrelation function, given by

$$C_X(t) = C_X\left(X_i, X_{i+t}\right) = \langle \left(X_i - \langle X_i \rangle\right)\left(X_{i+t} - \langle X_{i+t} \rangle\right) \rangle \ . \tag{4.4.1}$$

Typically, the autocorrelation function decays exponentially, so we consider the normalized autocorrelation function,

$$\Gamma_X(t) \equiv \frac{C_X(t)}{C_X(0)} \sim \exp\left(-\frac{t}{\tau}\right) \ , \tag{4.4.2}$$

where τ is the autocorrelation time, defined as the time after which the autocorrelation function decays by a factor e. We can estimate this parameter as

$$\tau \approx \frac{1}{2} + \sum_{t=1}^{N} \Gamma_X(t) \, , \tag{4.4.3}$$

where N is the number of configurations generated, since because of the exponential decay of $\Gamma_X(t)$, we have

$$\frac{1}{2} + \sum_{t=1}^{N} \Gamma_X(|t|) \approx \int_0^\infty \mathrm{d}t \mathrm{e}^{-t/\tau} = \tau \, . \tag{4.4.4}$$

In practice, we estimate the autocorrelation time by evaluating equation 4.4.3 after each iteration, by replacing N with the number of iterations, M, stopping when we obtain a value of τ such that

$$M \geq 4\tau + 1 \, , \tag{4.4.5}$$

with an error given by

$$\delta\tau = \sqrt{\frac{4M+2}{N}}\tau \, . \tag{4.4.6}$$

Having determined the autocorrelation time, τ, we now keep only the configurations separated by 3τ, out of those generated, and do all the statistical treatment assuming these to be uncorrelated, since they are only weakly correlated with each other. However, the autocorrelation times for the configurations generated with the Metropolis-Hastings algorithm are in some cases very large. As such, a significant number of configurations would be discarded, which would mean wasting computational resources. A more efficient way to proceed is to implement methods to decrease the degree of correlation between

sequential configurations, in order to obtain a lower autocorrelation time, as the one presented below.

Overrelaxation

The overrelaxation method is used to decrease the autocorrelation between two sequential configurations. It takes advantage of the fact that the Metropolis algorithm always accepts a new configuration U' if the action calculated with this configuration is the same as the one calculated with the previous configuration, according to equation 4.3.1. As such, this algorithm consists of replacing each link variable with a new link variable that keeps the action constant.

The action for the $\mathrm{U}(1)$ LGT is given in equation 2.3.45 in terms of the plaquette, which corresponds to the multiplication of four link variables forming an elementary square on the lattice. Since the action is given in terms of the plaquette, we consider the effect of changing one link variable, $U_\mu(n)$, on the plaquettes which share that link variable. In $4\mathcal{D}$, there are six plaquettes sharing the link variable $U_\mu(n)$. Therefore, the local contribution of these plaquettes to the action is given by

$$S = \beta \sum_{plaquettes} \mathrm{Re}\left[\Pi_{\mu\nu}(n)\right] = \beta \sum_{\nu\neq\mu} \mathrm{Re}\left[U_\mu(n) W_{\mu\nu}(n)\right] , \tag{4.4.7}$$

where we factorized each plaquette as the product between the link variable $U_\mu(n)$ and the *staple*, defined as the product between the other three link variables forming the plaquette. The sum of the two staples in each direction $\nu \neq \mu$ is given by

$$W_{\mu\nu}(n) = U_\nu(n+\hat{\mu}) U_\mu^\dagger(n+\hat{\nu}) U_\nu^\dagger(n) + U_\nu^\dagger(n-\hat{\nu}+\hat{\mu}) U_\mu^\dagger(n-\hat{\nu}) U_\nu(n-\hat{\nu}) . \tag{4.4.8}$$

By only changing the value of the link variable $U_\mu(n)$, the value of the staples of this link remains constant. As such, we can consider the sum of $W_{\mu\nu}(n)$ over all directions $\nu \neq \mu$, written as

$$W_\mu(n) = \sum_{\nu\neq\mu} W_{\mu\nu}(n) = \sum_{\nu\neq\mu} U_\nu(n+\hat{\mu}) U_\mu^\dagger(n+\hat{\nu}) U_\nu^\dagger(n) + U_\nu^\dagger(n-\hat{\nu}+\hat{\mu}) U_\mu^\dagger(n-\hat{\nu}) U_\nu(n-\hat{\nu}) , \tag{4.4.9}$$

which remains constant as we change $U_\mu(n)$.

We can then express the local contribution of the plaquettes which share the link $U_\mu(n)$ to the action, given by equation 4.4.7 as

$$S = \beta\, \mathrm{Re}\left[U_\mu(n) \sum_{\nu\neq\mu} W_{\mu\nu}(n) \right] = \beta\, \mathrm{Re}\left[U_\mu(n) W_\mu(n)\right] . \tag{4.4.10}$$

Since, in $\mathrm{U}(1)$, the link variables are complex numbers, the sum of staples $W_\mu(n)$ corresponds to the sum of complex numbers, and as such, we can express it as $W_\mu(n) = |W_\mu(n)| e^{i\theta_{W_\mu}(n)}$. Then, we can express equation 4.4.10 as

$$S = \beta |W_\mu(n)|\, \mathrm{Re}\left[e^{i\phi_\mu(n) + \theta_{W_\mu}(n)} \right] = \beta |W_\mu(n)| \cos\left(\phi_\mu(n) + \theta_{W_\mu}(n)\right) , \tag{4.4.11}$$

which is clearly invariant under the change $(\phi_\mu(n) + \theta_{W_\mu}(n)) \to 2\pi - (\phi_\mu(n) + \theta_{W_\mu}(n))$. Therefore, in order to apply the overrelaxation algorithm for a given link variable, we calculate the sum of the staples for that link, and change the link variable as $\phi_\mu \to 2\pi - 2\theta_{W_\mu}(n) - \phi_\mu(n)$. Repeating this process for every link variable, we obtain a new lattice configuration with the same action as before, but less correlated to the configuration at the previous Markov time.

Overrelaxation steps	$\tau_{Plaquette}$
0	42.38 ± 12.41
1	25.90 ± 5.95
2	23.40 ± 5.11
3	19.82 ± 4.00

Table 4.1: Autocorrelation times for the average plaquette with 0, 1, 2 and 3 overrelaxation steps for a 24^4 lattice with $\beta = 1$. Note that using one single overrelaxation step significantly reduces the autocorrelation time.

In table 4.1, we present the autocorrelation time of the average plaquette calculated with different numbers of overrelaxation steps for a given lattice configuration. The autocorrelation is significantly reduced when using overrelaxation steps, and as such, throughout this work we used 3 overrelaxation steps after each Monte Carlo iteration.

4.4.4 Jacknife

In order to determine the variance of calculated observables, we use the Jackknife method [24, 25]. This method consists of taking subsets of the set of measurements, by omitting the i-th measurement, and computing the average of each subset, $\bar{x}_i$, as

$$\bar{x}_i = \frac{1}{n-1} \sum_{j=1, j\neq i}^{n} x_j \,. \tag{4.4.12}$$

Then, the average $\bar{x}$ can be computed as the average of the average value of each of the n subsets, given by,

$$\bar{x} = \frac{1}{n} \sum_{i=1}^{n} \bar{x}_i \,. \tag{4.4.13}$$

It is easy to show that this average equals the average of the full set of measurements, since the sum $\sum_{i=1}^{n} \sum_{j=1, j\neq i}^{n} x_j$ sums each measurement $n-1$ times, i.e., $\sum_{i=1}^{n} \sum_{j=1, j\neq i}^{n} x_j = (n-1) \sum_{i=1}^{n} x_i$.

The variance of the distribution can then be related to the deviation of the average value of each subset from the average of the full set, as

$$\sigma_{\bar{x}}^2 = \frac{n-1}{n} \sum_{i=1}^{n} (\bar{x}_i - \bar{x})^2 = \frac{1}{n(n-1)} \sum_{i=1}^{n} (x_i - \bar{x})^2 \,. \tag{4.4.14}$$

4.4.5 Multihit

A method which can be used to reduce the variance of calculated observables is multihit[26]. This thecnique consists of replacing each temporal link variable with an effective link variable calculated against a constant background, as

$$U_\mu(n) \to \frac{\int \mathrm{d}U U \exp(-\beta S)}{\int \mathrm{d}U \exp(-\beta S)} \,. \tag{4.4.15}$$

Observables calculated with these new link variables have the same average value as the ones calculated without considering this substitution, but have a smaller variance. This way, it is possible to reduce statistical errors.

In lattice QCD, the expression in equation 4.4.15 is usually evaluated numerically, as the analitical calculation is somewhat envolved. However, considering the symmetry group $\mathrm{U}(1)$, this calculation can easily be done and we obtain the substitution[27]

$$U_\mu(n) \to \frac{I_1\left(\beta\left|W_\mu(n)\right|\right)}{I_0\left(\beta\left|W_\mu(n)\right|\right)} \frac{W_\mu(n)}{\left|W_\mu(n)\right|} \,, \tag{4.4.16}$$

where $I_n(x)$ are the modified Bessel functions of order n, and $W_\mu(n)$ is the sum of the staples of the link $U_\mu(n)$, defined in equation 4.4.9.

This method will be useful to calculate the Polyakov loop correlator,$\langle P(0)P^\dagger(r)\rangle$, defined in equation 2.4.14, as, particularly in the confined phase, this quantity has large fluctuations, which induce large statistical errors. When calculating correlation functions of this type, involving a product of link variables separated by some spatial distance r, we must discard the results for $r = 1$, as the multihit method for the correlation between two link variables is only valid if the link variables are at distance $r \geq 2$[26].

4.4.6 Multilevel

The calculations of expectation values of large Wilson loops and of correlators between Wilson loops or Polyakov loops in LGT is difficult, as the signal-to-noise ratio is very low for large loops. The multilevel method[28] presents a mechanism to exponentially reduce the statistical errors in these calculations, which takes advantage of the locality of the action, i.e., of the fact that the action for one link variable only depends on the value of the plaquettes connected to it.

In this section, we briefly outline the details of the multilevel method, by considering the calculation of the Polyakov loop correlator.

The Polyakov loop correlator consists of the average value of the product of a Polyakov loop and an anti Polyakov loop, separated by a distance r in the μ direction. The Polyakov loop is given by a product of temporal links over the full temporal extent of the lattice, N_t, given by equation 2.4.6. As such, we can write the product between a Polyakov loop and an anti Polyakov loop as

$$P^\dagger(x)P(x+r\hat{\mu}) = \Big(U_0(x)\cdots U_0(x+N_t\hat{e}_0)\Big)^\dagger \Big(U_0(x+r\hat{\mu})\cdots U_0(x+r\hat{\mu}+N_t\hat{e}_0)\Big) \,. \tag{4.4.17}$$

Since the link variables, $U_0(x)$ are elements of the $\mathrm{U}(1)$ group, they commute with each other, and as such, we can write the product between a Polyakov loop and an anti Polyakov loop as

$$\begin{aligned} P^\dagger(x)P(x+r\hat{\mu}) &= \left(U_0^\dagger(x)U_0(x+r\hat{\mu})\right)\cdots\left(U_0^\dagger(x+N_t\hat{e}_0)U_0(x+r\hat{\mu}+N_t\hat{e}_0)\right) \\ &= \mathbb{T}(x,0,r,\mu)\cdots\mathbb{T}(x,N_t-1,r,\mu)\,, \end{aligned} \tag{4.4.18}$$

where we introduced the two link operator

$$\mathbb{T}(x,t,r,\mu) = U_0^\dagger(x+\hat{e}_0 t)U_0(x+r\hat{\mu}+\hat{e}_0 t)\,. \tag{4.4.19}$$

The two link operators $\mathbb{T}(x,t,r,\mu)$ correspond to the product of two temporal link variables in some temporal layer separated by a distance r in the μ direction. Since we interpreted the product of a Polyakov loop and an anti Polyakov loop as the temporal propagator of a static fermion and antifermion pair, we can interpret the two link operator $\mathbb{T}(x,t,r,\mu)$ as the propagator of a static fermion and antifermion pair separated by a distance r from t to $t+a_t$.

Due to the locality of the action, we can separate the lattice into sublattices of size 2 in the temporal direction by fixing the value of the spatial links in the 3 dimensional temporal hyperplanes limiting the sublattice. This way, we can calculate an average on the lattice as the product of averages on each sublattice.

As such, we can relate the average value of the Polyakov correlator to the average of the two link operators $\mathbb{T}(x,t,r,\mu)$ on each sublattice as

$$\langle P^\dagger(x)P(x+r\hat{\mu})\rangle = \langle[\mathbb{T}(x,0,r,\mu)\mathbb{T}(x,1,r,\mu)]\cdots[\mathbb{T}(x,N_t-2,r,\mu)\mathbb{T}(x,N_t-1,r,\mu)]\rangle\,, \tag{4.4.20}$$

where $\langle\cdot\rangle$ and $[\cdot]$ denote the average on the full lattice and the average on a sublattice, respectively.

We can apply the same reasoning to calculate the average value of the product of two two link operators on a temporal sublattice of thickness 2 as the product of the average of each two link operators on the sublattice of thickness 1 where they are inserted, as

$$[\mathbb{T}(x,0,r,\mu)\mathbb{T}(x,1,r,\mu)] = [[\mathbb{T}(x,0,r,\mu)][\mathbb{T}(x,1,r,\mu)]]\,. \tag{4.4.21}$$

As such, we can calculate the Polyakov correlator as

$$\langle P^\dagger(x)P(x+r\hat{\mu})\rangle = \langle[[\mathbb{T}(x,0,r,\mu)][\mathbb{T}(x,1,r,\mu)]]\cdots[[\mathbb{T}(x,N_t-2,r,\mu)][\mathbb{T}(x,N_t-1,r,\mu)]]\rangle\,. \tag{4.4.22}$$

In order to calculate the average values within a given sublattice, the Metropolis-Hastings algorithm, described in section 4.3 is used to generate configurations in the sublattice, in the same way as for the full lattice. This is done while keeping the spatial links on the hyperplanes limiting the sublattice fixed. Overrelaxation steps, described in section 4.4.3 can be used in each level of the multilevel method in

order to reduce the correlation between the configurations generated.

More levels can be added to this algorithm, by considering an intermediate step with averages taken on sublattices of thickness 4 after calculating the averages on the sublattices of size 2 in the temporal direction. In chapter 5, in order to calculate the Polyakov loop correlator, we will consider two levels of the multilevel algorithm, by taking the average of the two link operators $\mathbb{T}(x,t,r,\mu)$ first on sublattices of size 2, and then of size 4. Note that this can only be done it the total temporal extent of the lattice is a multiple of 4.

4.5 CUDA

The generation of lattice configurations involves, for each link variable, the generation of a random value and the calculation of the action to determine whether the new value for the link variable is accepted or not, as covered in section 4.3. In a four dimensional lattice with a large number of points in each direction, this results in an extremely large number of calculations, which would take a large amount of time to be done sequentially. Furthermore, as several configurations of the lattice are generated in each simulation, in order to calculate the average value of observables, it quickly becomes impractical to run simulations this way. Parallel computing is a way to speed up this process, by carrying out separate calculations on different cores of the central process unit (CPU) and thus doing several calculations simultaneously. However, the number of cores in a CPU is relatively small, and more efficiency can be achieved by using the graphics processing unit (GPU), which has many cores and high memory bandwidth, to run the calculations. This can be done by using the the Compute Unified Device Architecture (CUDA).

CUDA is an architecture developed by NVIDIA, which takes advantage of the large number of cores and threads in a GPU to perform general purpose calculations using parallel computation. It is designed to be used with C, C++ and Fortran programming languages. In this work, we used CUDA with the C++ programming language, which allowed for the use of useful features of C++ in calculations parallelized in the GPU. The use of this type of architecture with a CUDA-enabled GPU significantly decreases the computational time necessary in processes in which calculations can be highly parallelized, such as the case we are interested in.

Throughout this work, we will be using CUDA to run the simulations and calculations on the lattice. We used five CUDA-enabled GPUs, namely, two NVIDIA GeForce GTX TITAN X, two NVIDIA GeForce RTX 2080 Ti, and one NVIDIA Tesla M2075.

Chapter 5

Simulation of the U(1) LGT

In this chapter we present the details and the results of the computational simulations of the $\mathrm{U}(1)$ LGT. We begin by looking at the isotropic case, for which, after mentioning the quantities calculated, we present the methods used to extract the value of the critical coupling, β_c at which the phase transition takes place. We follow with a discussion of the order of this phase transition. Finally, using the same treatment as for the isotropic case, we use the anisotropic regularization in order to obtain the coordinates of the phase transition at higher temperatures, and retrieve the full phase diagram of the $\mathrm{U}(1)$ LGT.

5.1 Isotropic Lattice

We begin by looking at the isotropic case, by considering the same coupling for the spatial and spatial-temporal parts of the action, and thus, considering the lattice spacing in the spatial directions to be equal to the lattice spacing in the temporal direction, $a_s = a_t = a$. For this case, we will use the following action for the simulations

$$S = -\sum_{n,\mu<\nu} \beta Re\left[\Pi_{\mu\nu}(n)\right] = -\sum_{n,\mu<\nu} \beta \cos\left[\phi_\mu(n) + \phi_\nu\left(n+\hat{\mu}\right) - \phi_\mu\left(n+\hat{\nu}\right) - \phi_\nu(n)\right] . \tag{5.1.1}$$

As stated in chapter 2, the observables calculated in LGT are mean values of path ordered products of link variables. The simplest observable to be considered is then given by the mean value of the plaquette, $\Pi_{\mu\nu}$, defined by the product of links over the shortest closed path of link variables, the boundary of an elementary square on the lattice. The mean value of the plaquette in $(3+1)\mathrm{D}$ LGT is given by

$$W = \frac{1}{6N_tN_s^3}\sum_{n,\mu<\nu} Re\Pi_{\mu\nu}(n)\,, \tag{5.1.2}$$

where N_t and N_s denote the temporal and spatial extent of the lattice, respectively, x denotes the lattice sites and we divide by 6, the number of plaquettes defined on each lattice point. The mean value of the plaquette is proportional to the free energy of the system, and as such, in order to identify phase transitions on the average plaquette, we also consider the plaquette susceptibility, given by

$$C_v = N_t N_s^3 (\langle W^2 \rangle - \langle W \rangle^2) \,. \tag{5.1.3}$$

Another quantity we will be interested in is the Polyakov loop, defined as the ordered product of link variables along a line on the temporal direction,

$$P(r) = \prod_{t=0}^{N_t - 1} U_0(t, r) \,, \tag{5.1.4}$$

where x now denotes the lattice sites on the spatial lattice.

Note that, because we imposed closed boundary conditions, the Polyakov loop is defined as a product of link variables along a closed path, and as such, it is a gauge invariant quantity.

The observable computed, the mean value of the Polyakov loop, is given by the average of the Polyakov loop over the spatial volume,

$$P = \frac{1}{N_s^3} \sum_r P(r) \,. \tag{5.1.5}$$

The average Polyakov loop is an important quantity for our study, since it can be interpreted as the probability of observing a single static charge[2]. As such, this observable distinguishes between a confined phase and a deconfined phase. At large values of the coupling constant (small β) we expect our theory to be confined, so that no free charges are observed, and as such, $P = 0$. At small values of the coupling constant (large β), we expect our theory to be deconfined, so that free static charges can be observed, and we have $P \neq 0$. Therefore, the average Polyakov loop is the order parameter that distinguishes between the two phases of this theory, and it is this observable that will be used in order to determine the value of β at which the phase transition between this two phases occurs.

In order to identify the phase transition, we will study the susceptibility of the Polyakov loop, defined as

$$\chi_P = N_t N_s^3 (\langle P^2 \rangle - \langle P \rangle^2) \,, \tag{5.1.6}$$

which peaks at the critical value of β for which the phase transition occurs.

5.1.1 Simulation results

Average Plaquette

In order to probe the value of the average plaquette for different values of the gauge coupling, we simulate the action in equation 5.1.1 for different values of β and calculate the average plaquette, as well as its susceptibility for each of these values. More detail on the methods used for the simulation can be found in chapter 4. We repeat this procedure for different extents of the lattice in the temporal direction, N_t, in order to study the theory at different temperatures, $T = \frac{1}{a_t N_t}$, while keeping the spatial extent fixed at $N_s = 24$.

The results obtained for the average plaquette and its susceptibility can be seen in figure 5.1. In figure 5.1 (a), instead of plotting the average plaquette, W, presented in equation 5.1.2, we plot $1 - W$, in order to match the literature.

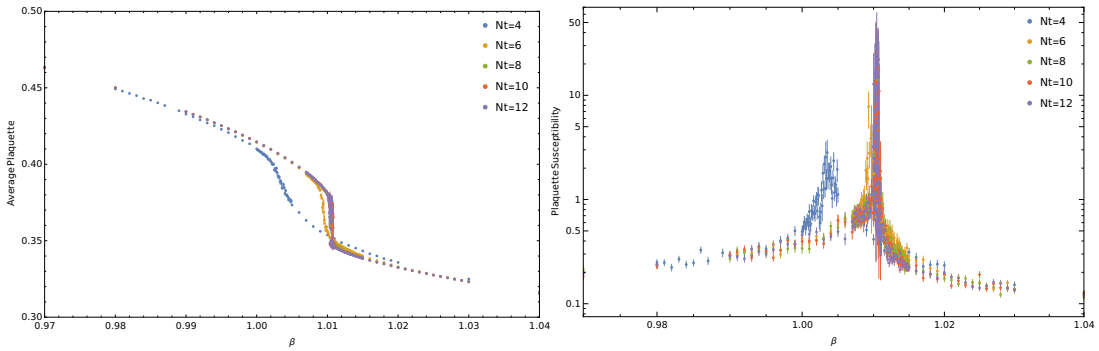

((a)) ((b))

Figure 5.1: Average value of the plaquette (a) and plaquette susceptibility (b) as a function of β for a $4\mathcal{D}$ lattice with $N_t = 4, 6, 8, 10, 12$. and $N_s = 24$.

In figure 5.1 (a), we can see that the average plaquette undergoes a phase transition as we vary the value of the coupling parameter, β, which becomes evident in figure 5.1 (b) where we notice the peaks in the plaquette susceptibility. However, a quantity more suited to identify the phase transition, as we saw in chapter 3 is the Polyakov loop, at which we will be looking in the following.

Average Polyakov loop

The average Polyakov loop is determined in a similar way to the average plaquette, by simulating the action in equation 5.1.1 for different values of β and N_t, with $N_s = 24$. The average value of the Polyakov loop is shown in figure 5.2, where it can be seen that the Polyakov varies from $\langle P \rangle = 0$ for strong coupling to a finite value at weak coupling, denoting the transition from the confined to the deconfined phase. The precise value of the critical coupling, β_c, at which this phase transition occurs for each value of N_t can be obtained by determining the position of the peaks in the Polyakov loop susceptibility shown in figure 5.2.

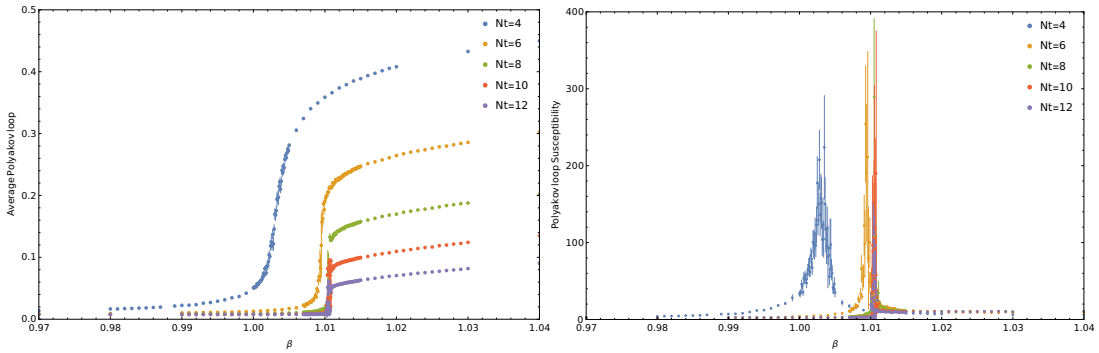

((a)) ((b))

Figure 5.2: Average value of the Polyakov loop (a) and Polyakov loop susceptibility (b) as a function of β for a $4\mathcal{D}$ lattice with $N_t = 4, 6, 8, 10, 12$. and $N_s = 24$.

Phase diagram

In order to determine the value of the coupling, β_c, at which the phase transition occurs, the data for the Polyakov loop susceptibility close to the peak was fitted to a Lorentzian function, of the form

$$\chi(\beta) = \frac{A}{\pi} \frac{\Gamma/2}{(\beta - \beta_c)^2 + (\Gamma/2)^2}\,, \tag{5.1.7}$$

for each value of N_t. Hence the values of β_c shown in table 5.1 were obtained for each value of N_t. It can be seen that the value of β_c increases with N_t, varying less for larger values of N_t, as we reach the limit of zero temperature. In figure 5.3 we present the values of the critical coupling for each value of N_t plotted in the parameter space.

N_t	β_c
2	0.89929 ± 0.00015
4	1.00276 ± 0.00006
6	1.00948 ± 0.00009
8	1.01043 ± 0.00009
10	1.01051 ± 0.00054
12	1.01057 ± 0.00007

Table 5.1: Position of the peaks in the Polyakov Loop susceptibility for an isotropic lattice with $N_s = 24$.

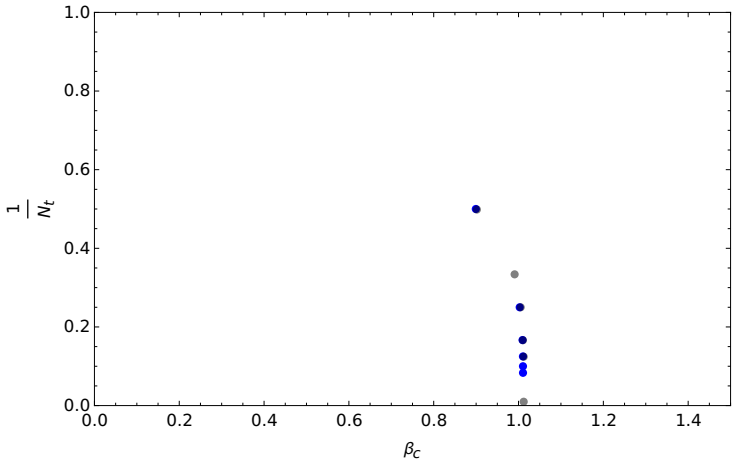

Figure 5.3: Position of the peaks in the Polyakov loop susceptibility obtained in blue. In gray, the points from the phase diagram obtained in [18]. The results obtained show great agreement with the literature.

The results obtained are compatible with previous phase diagrams obtained in the literature [18], which validated our approach to determine the points at which the phase transition takes place, as well as the numerical simulations made.

This phase diagram is clearly incomplete, as we were only able to probe a narrow region of the parameter space by studying the isotropic lattice. In order to obtain a complete phase diagram, we need to determine the coordinates of the phase transition at higher temperatures. However, going to higher temperatures in this lattice regularization is not possible, as it would require considering a smaller number of points in the lattice temporal direction, N_t, and we have already reached the inferior limit of the number of points with $N_t = 2$. This challenge can be overcome by considering the anisotropic lattice

regularization. As will be seen in the next section, this regularization allows the study of the $\mathrm{U}(1)$ LGT at higher temperatures.

5.2 Potential

Another way to investigate the phase transition of the $\mathrm{U}(1)$ LGT is to look at the potential between two static charges, as seen in section 3.3. The correlator between two Polyakov loops separated by some distance r decays exponentially with this potential, as

$$\langle P^*(0)P(r)\rangle = e^{-N_t a V(r)}\,, \tag{5.2.1}$$

where N_t is the number of points in the time direction, a is the lattice spacing and r is the distance in lattice units. Inverting this relation, we can determine the potential at a given distance, by calculating the average value of the correlator of two Polyakov loops separated by that distance, as

$$aV(r) = -\frac{1}{N_t}\log(\langle P(0)P^\dagger(r)\rangle)\,. \tag{5.2.2}$$

It is difficult to get significant statistics to calculate this correlator, as there are fluctuations in the value of the Polyakov loop at each spatial lattice point, which introduce a significant amount of noise, leading to large statistical errors. In order to overcome this, we used the multihit and multilevel methods to calculate the potential. A presentation on these methods can be found in sections 4.4.5 and 4.4.6.

We calculated the potential for several values of the coupling parameter, β and found that for strong coupling (small β), the potential depends linearly with the distance r at large distances, showing that electric charges are confined in this region of the parameter space. For weak coupling (large β), we found a Coulomb potential, with the value of the potential becoming constant at large values of r, which shows that electric charges are no longer confined, and instead we have a situation similar to electrodynamics. In figure 5.4 we show the potential computed at two values of β, illustrating the two situations.

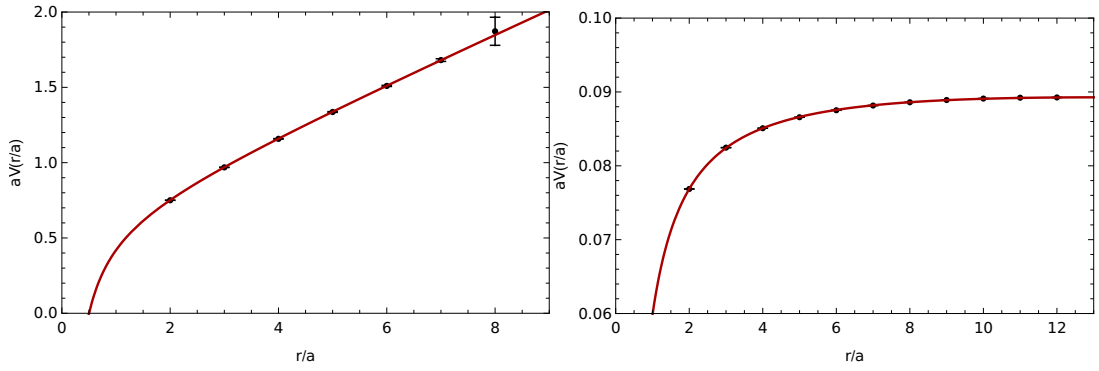

((a)) $\beta = 1$ ((b)) $\beta = 3$

Figure 5.4: Potential calculated on an isotropic 24^4 lattice for $\beta = 1, 3$, using the multihit and the multilevel methods. For $\beta = 1$, we obtain a linear potential at large distances, corresponding to the confined phase, while for $\beta = 3$ we obtain a Coulomb potential, approaching a constant value for large distances, characteristic of the deconfined phase.

According to the form of the potential in the confining and Coulomb phases, we fitted our results with a function of the form

$$aV(r) = A - \frac{b}{r} + \sigma r\,, \tag{5.2.3}$$

where σ is the string tension, which is finite in the confining phase, being responsible for the linear behaviour of the potential at large distances, and goes to zero in the deconfined phase, leaving us with a Coulomb potential. Thus, the string tension is an order parameter of the $\mathrm{U}(1)$ LGT, indicating which phase our system is in for each value of the coupling constant β. The fitting parameters obtained for each value of β can be seen in table C.1. In figure 5.5, we can see the value of the string tension decreasing near the phase transition, until it becomes zero in the Coulomb phase.

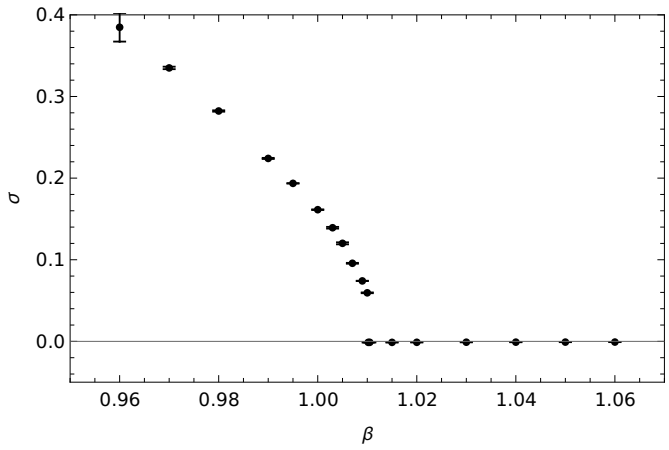

Figure 5.5: String tension calculated for values of β near the phase transition. Before the phase transition, in the confined phase, this parameter has a finite value, and it decreases as we approach the phase transition, becoming zero in the deconfined phase.

5.3 Order of the Phase Transition

When working very close to the phase transition, the lattice configurations generated by the Markov chain may oscillate between the two phases of the theory. Therefore, at values of the gauge coupling, β, near the phase transition, the absolute value of Polyakov loop calculated on the configurations generated can be zero, $|P| = 0$, characteristic of the confined phase, or a finite value, $|P| \neq 0$, as happens in the case of the Coulomb phase. If the transition is discontinuous, the value of the average Polyakov loop has a jump at the phase transition, and as such the value of the Polyakov loop calculated in configurations in the Coulomb phase can be significantly different from zero. These oscillations of the Markov chain between the two configurations introduce errors in obtaining the value of the average Polyakov loop very close to the phase transition. However, these also present a way to determine the order of the phase transition.

If the transition is discontinuous, by generating successive configurations near the phase transition with the Markov chain Monte Carlo method described in chapter 4, we expect to find values of the Polyakov loop for each configuration both at zero, and at a value away from zero. Then, by plotting an

histogram of the absolute value of the Polyakov loop, we will find two peaks at the two values of the Polyakov loop for each phase, if the transition is of first order. By generating configurations at values of β near the phase transition, we found this two peak structure at large values of N_s for $N_t \geq 6$, indicating that, for isotropic lattices with these temporal extents, the transition is first order, as expected [19]. As an example, in figure 5.6 we present the histogram obtained for a simulation with $N_t = 8$, where we can see the double peak appearing at the phase transition.

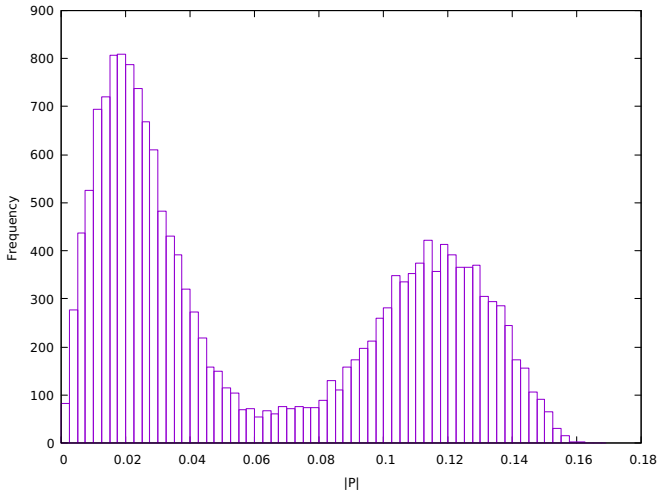

Figure 5.6: Histogram of the absolute value of the Polyakov loop calculated in a four dimensional lattice with $N_s = 24$ and $N_t = 8$, at the value of the coupling parameter determined for the phase transition, in table 5.1, $\beta = 1.01043$. We can identify two peaks, indicating a first order transition.

For lattices with less points in the temporal direction, the two peak structure was not found. In particular for $N_t = 2$, as can be seen in figure 5.7, only one peak is seen at the phase transition. As we vary β from the confined phase to the Coulomb phase, in this case, we always have one peak, which is centered at larger values of the Polyakov loop, as β increases. As such, for the isotropic lattice with this extent of the temporal direction, we can identify the phase transition as continuous.

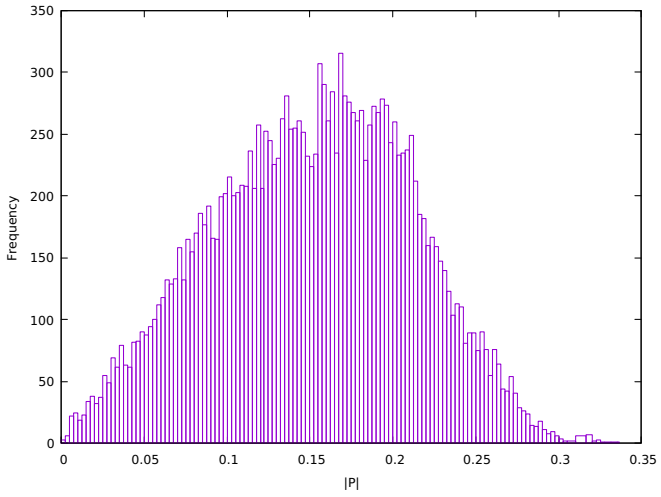

Figure 5.7: Histogram of the absolute value of the Polyakov loop calculated in a four dimensional lattice with $N_s = 24$ and $N_t = 2$, at the value of the coupling parameter determined for the phase transition, in table 5.1, $\beta = 0.89929$. Only one peak is seen, which indicates a continuous transition.

The situation for lattices with $N_t = 4$ was more complicated, as for smaller values of the spatial extent of the lattice, N_s, the theory appeared to have a weakly first order transition, with two peaks appearing in the Polyakov loop histogram very close to each other, with a significant overlap. However, as we increased N_s, the second peak becomes smaller and harder to identify. It is not clear whether the second peak is still present at large values of N_s, but because of the proximity between the two peaks, the smaller peak is harder to identify or if this peak vanishes at large spatial extents. As such, for $N_t = 4$, as we take the spatial size to infinity, the phase transition is either second order or very weakly first order.

These results agree with the literature [19], indicating a first order phase transition for $N_t \geq 6$ and a second order phase transition for $N_t = 2.$, as we approach the limit $N_t = 1$, where we recover the three dimensional XY model. A more clear picture of what happens for $N_t = 4$ could be obtained by investigating the scaling of the maximum value of the plaquette susceptibility, C_v with the spatial extent of the lattice, N_s. By determining the critical exponents of this quantity, it would be possible to confidently determine the order of the phase transitions.

5.4 Anisotropic Lattice

In order to study this theory at different temperatures, we introduce the anisotropic lattice regularization [6], by setting a different coupling for the space-space and space-time plaquettes on the action. The anisotropic action is written as in equation 2.3.46, where ξ is the anisotropy parameter. In this action, we have a coupling $\beta\xi$ on the space-time part, and a coupling $\frac{\beta}{\xi}$ on the space-space part, thus, by choosing different values of ξ, we can study the theory with different couplings on each direction. Setting $\xi = 1$ we recover the isotropic action in equation 5.1.1.

Since the anisotropy parameter gives a measure of the ratio between the spatial and temporal lattice spacings, $\xi = as/at$, by choosing different values of ξ, we can change a_t while keeping a_s constant, thus changing the temperature, given by

$$T = \frac{1}{N_t a_t} = \frac{\xi}{N_t a_s}\,. \tag{5.4.1}$$

Since in the isotropic case, we had the same lattice spacing a on all directions, by keeping the spatial lattice distance constant, we can express the temperature as

$$T = \frac{\xi}{N_t a}\,, \tag{5.4.2}$$

where a is the lattice spacing on the isotropic lattice.

From equation 5.4.2 it is clear that studying an anisotropic lattice with an anisotropy parameter ξ and N_t points in the time direction is equivalent to studying the isotropic lattice with $\frac{N_t}{\xi}$ points in the time direction, which allows us to probe new regions of the parameter space that were inaccessible through the isotropic regularization, since our approach only allows even integer values of N_t to be considered. Therefore, considering the anisotropic lattice regularization will make it possible to construct a more

complete phase diagram of the $U(1)$ LGT.

5.4.1 Simulation results

The simulations with the anisotropic lattice were conducted in the same way as for the isotropic lattice in the previous section. For each value of N_t, the temporal extent of the lattice, we calculated the value of the average plaquette, Polyakov loop, and their susceptibilities, for each value of β, and fitted the peaks in the Polyakov loop susceptibility to a Lorentzian function (equation 5.1.7) in order to determine the critical values of the coupling at which the phase transition occurs, β_c. The values of β_c obtained for each lattice size and for each value of ξ can be seen in table C.2

Phase diagram

In order to plot the phase diagram in terms of the parameters in the Hamiltonian model, we compare the anisotropic action used in the simulations, in equation 2.3.46 to the action derived from the Hamiltonian in chapter 2, written in equation 2.3.44. By matching the coefficients multiplying the spatial and space-time parts of the actions in equations 2.3.46 and 2.3.44, we find the following relations between the simulation parameters and the Hamiltonian parameters

$$\frac{\beta}{\xi} = \Delta\tau K \Leftrightarrow K = \frac{\beta}{\xi\Delta\tau}\,, \tag{5.4.3}$$

$$\beta\xi = \frac{1}{\Delta\tau U} \Leftrightarrow U\Delta\tau = \frac{1}{\beta\xi} \Leftrightarrow U = \frac{1}{\Delta\tau\beta\xi}\,, \tag{5.4.4}$$

where the time intervals $\Delta\tau$ used in the Trotter decomposition coincide with the lattice spacing in the temporal direction when we identify our theory with a $4\mathcal{D}$ LGT in section 2.3.3, so the temperature is given by

$$T = \frac{1}{N_t\Delta\tau}\,. \tag{5.4.5}$$

With the Hamiltonian parameters, as well as the temperature, written as functions of the simulation parameters, we can express the quantities in terms of which we want to plot the phase diagram as

$$\begin{aligned} \frac{K}{U} &= \beta^2\,, \\ \frac{T}{U} &= \frac{\beta\xi}{N_t}\,. \end{aligned} \tag{5.4.6}$$

Having determined the critical value of the coupling, β_c, for different values of N_t for each value of the anisotropy parameter considered, we can plot the points at which the phase transition occurs, in terms of the quantities in equation 5.4.6, in order to obtain the phase diagram, as is shown in figure 5.8.

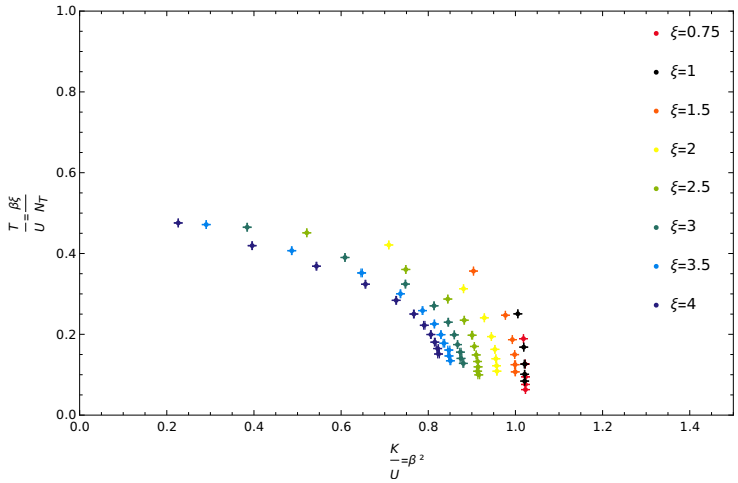

Figure 5.8: Position of the peaks in the Polyakov loop susceptibility in terms of the quantities in equation 5.4.6

.

Plotting the coordinates of the phase transition in terms of the quantities in equation 5.4.6 is not enough to retrieve the phase diagram of the $\mathrm{U}(1)$ LGT. As can be seen in figure 5.8, by using this parameterization, the points for the position of the peaks in the Polyakov loop susceptibility do not line up in a single curve. This may happen because of the approximations used when deriving the action in equation 2.3.44 from the Hamiltonian model. In fact, if we are studying this theory outside of the region of validity of these approximations, the coefficient multiplying the space-time plaquette in the action, $1/\Delta\tau U$, may be incorrect, and it is thus not appropriate to use the parameterization in equation 5.4.6 to plot the phase diagram. In the following sections, we will explore this possibility, in order to obtain the correct phase diagram for this theory.

5.4.2 Correction to the Villain approximation

As mentioned in the previous section, the coefficient multiplying the space-time part of the action in equation 2.3.46 is not exact because of the approximations used to derive this action from the Hamiltonian. This derivation can be found in chapter 2. In order to retrieve the phase diagram of the $U(1)$ LGT we can consider a better approximation of the action from the Hamiltonian model, in equation 2.3.44. In chapter 2, we derived the following action from the Hamiltonian

$$\begin{aligned} S[\phi, n] = &- \Delta\tau K \sum_{\tau,r,\mu<\nu} \cos\left[\phi_\mu(\tau,r) + \phi_\nu(\tau, r+\hat{\mu}) - \phi_\mu(\tau, r+\hat{\nu}) - \phi_\nu(\tau,r)\right] \\ &- i \sum_{\tau,r,\mu} \left[\phi_\mu(\tau,r) + \phi_0(\tau, r+\hat{\mu}) - \phi_\mu(\tau+1,r) - \phi_0(\tau,r)\right] n_\mu(\tau,r) \\ &+ \Delta\tau \frac{U}{2} \sum_{\tau,r,\mu} \left[n_\mu(\tau,r)\right]^2 , \end{aligned} \tag{5.4.7}$$

and further simplified the last two terms of this action by using the Villain approximation, given by [5]

$$e^{z\cos(\Phi)} = \sum_n I_n(z) e^{in\Phi} \simeq \sum_n e^{-\frac{1}{2z}n^2 + i\Phi n} , \tag{5.4.8}$$

with $z = \frac{1}{\Delta\tau U}$. However, this approximation is valid only in the limit of large z [29]. Without considering this limit, the approximation can be expressed as

$$e^{z\cos(\Phi)} = \sum_n I_n(z) e^{in\Phi} \simeq \sum_n e^{-\frac{1}{2z_V}n^2 + i\Phi n}\,, \tag{5.4.9}$$

with

$$z_V = -\frac{1}{2\log\left(\frac{I_1(z)}{I_0(z)}\right)}\,. \tag{5.4.10}$$

In the limit $z \to \infty$, we have $z_V \approx z$ and we recover equation 5.4.8.

Using now the approximation in equation 5.4.9 in the action in equation 5.4.7 with $z_V = \frac{1}{\Delta\tau U}$ we obtain

$$\begin{aligned} S[\phi] = &-\Delta\tau K \sum_{n,\mu<\nu} \cos\left[\phi_\mu(n) + \phi_\nu(n+\hat{\mu}) - \phi_\mu(n+\hat{\nu}) - \phi_\nu(n)\right] \\ &- z \sum_{n,\mu} \cos\left[\phi_\mu(n) + \phi_0(n+\hat{\mu}) - \phi_\mu(n+e_0) - \phi_0(n)\right]\,. \end{aligned} \tag{5.4.11}$$

with z such that

$$\frac{1}{\Delta\tau U} = -\frac{1}{2\log\left(\frac{I_1(z)}{I_0(z)}\right)}\,. \tag{5.4.12}$$

By matching the coefficients multiplying the spatial and space-time parts of the action in equation 5.4.11 with the ones on the simulated action, in equation 2.3.46, we obtain the relations

$$\beta\xi = z \Rightarrow \frac{1}{\Delta\tau U} = -\frac{1}{2\log\left(\frac{I_1(\beta\xi)}{I_0(\beta\xi)}\right)} \Leftrightarrow \frac{1}{U} = -\frac{\Delta\tau}{2\log\left(\frac{I_1(\beta\xi)}{I_0(\beta\xi)}\right)}\,, \tag{5.4.13}$$

$$\frac{\beta}{\xi} = \Delta\tau K \Leftrightarrow K = \frac{\beta}{\xi\Delta\tau}\,. \tag{5.4.14}$$

These relations, along with the definition of the temperature, T, in equation 5.4.5, yield

$$\begin{aligned} \frac{K}{U} &= -\frac{\beta}{\xi}\frac{1}{2\log\left(\frac{I_1(\beta\xi)}{I_0(\beta\xi)}\right)}\,, \\ \frac{T}{U} &= -\frac{1}{N_t}\frac{1}{2\log\left(\frac{I_1(\beta\xi)}{I_0(\beta\xi)}\right)}\,. \end{aligned} \tag{5.4.15}$$

We can now plot the critical points at which the phase transition occurs for each value of N_t and ξ in terms of $\frac{K}{U}$ and $\frac{T}{U}$, defined in equation 5.4.15 and obtain the phase diagram shown in figure 5.9.

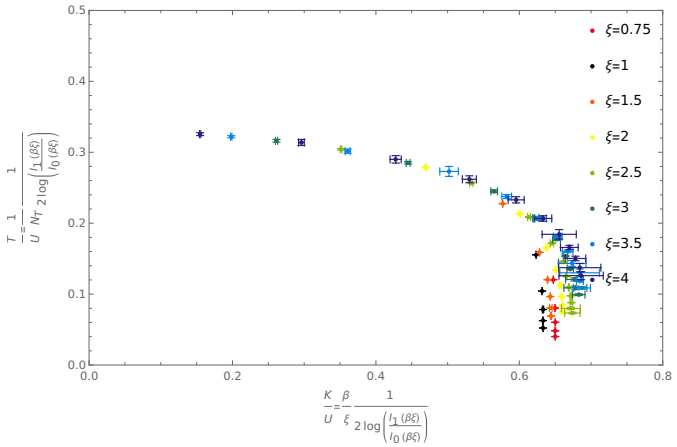

Figure 5.9: Phase diagram using the relations in equation 5.4.15.

With this approach, we obtain a better collapsed phase diagram than in the initial case, in which we considered the action in equation 2.3.44. However, considering this correction on the Villain approximation does not fully collapse the phase diagram, in particular for larger values of $\frac{K}{U}$, which indicates that, although this approximation is more general than the one used when initially deriving the action from the Hamiltonian model, it is still not exact, and considering higher order approximations could provide further improvements on the collapse of the points for different values of ξ.

5.4.3 Rescaling of the phase diagram

The discussion in the previous sections makes it clear that the coefficient multiplying the space-time part of the action in equation 2.3.44 is not exact because of the approximations used to derive this action from the Hamiltonian in chapter 2. Considering the next order Villain approximation, we were able to get a better collapse of the curves indicating the phase transition from the confined phase to the Coulomb phase. However, the correction considered in the previous section did not fully collapse the phase diagram which indicates that higher order approximations might be necessary. As such, in order to obtain the correct form of the phase diagram, we replace the coefficient multiplying the space-time part of the action with an unknown function of itself, and write the action as

$$\begin{aligned} S[\phi] = &- \Delta\tau K \sum_{n,\mu<\nu} \cos\left[\phi_\mu(n) + \phi_\nu(n+\hat{\mu}) - \phi_\mu(n+\hat{\nu}) - \phi_\nu(n)\right] \\ &- f\left(\frac{1}{\Delta\tau U}\right) \sum_{n,\mu} \cos\left[\phi_\mu(n) + \phi_0(n+\hat{\mu}) - \phi_\mu(n+e_0) - \phi_0(n)\right] . \end{aligned} \tag{5.4.16}$$

Again, by matching the coefficients multiplying each part of the previous action with the ones on the action in terms of the coupling and anisotropy parameters, in equation 2.3.46, we now find the following relations

$$\frac{\beta}{\xi} = \Delta\tau K \Leftrightarrow K = \frac{\beta}{\xi\Delta\tau} , \tag{5.4.17}$$

$$\beta\xi = f\left(\frac{1}{\Delta\tau U}\right) \Leftrightarrow \frac{1}{\Delta\tau U} = g\left(\beta\xi\right) \Leftrightarrow U = \frac{1}{\Delta\tau g\left(\beta\xi\right)}\,, \tag{5.4.18}$$

where we denote the inverse function of $f(x)$ by $g(x) = f^{-1}(x)$. Having written the Hamiltonian parameters, as well as the temperature, as functions of the simulation parameters, we can express the phase diagram in term of the quantities

$$\begin{aligned} \frac{K}{U} &= \frac{\beta \cdot g\left(\beta\xi\right)}{\xi}\,, \\ \frac{T}{U} &= \frac{g\left(\beta\xi\right)}{N_t}\,. \end{aligned} \tag{5.4.19}$$

In order to find the form of the function $g(x)$ we set the condition that in the limit of zero temperature ($N_t \to +\infty$), the value of $\frac{K}{U}$ goes to 1, i.e., $\frac{K_0}{U} = 1$. Then, using the relations in equation 5.4.19, we find

$$\frac{K_0}{U} = 1 \Leftrightarrow \frac{\beta_0(\xi) \cdot g\left(\beta_0(\xi) \cdot \xi\right)}{\xi} = 1 \Leftrightarrow g\left(\beta_0(\xi) \cdot \xi\right) = \frac{\xi}{\beta_0(\xi)}\,, \tag{5.4.20}$$

where $\beta_0(\xi) = \lim_{N_t \to +\infty} \beta(N_t, \xi)$

Using the data obtained in the simulations, we can obtain the value of β_0 for each ξ. The value of the critical coupling, β_c, increases for increasing values of N_t. However, as we approach large lattice sizes in the temporal direction, the value of β_c only increases slightly with increasing N_t. As such, for each value of the anisotropy parameter considered, the value of β_c for the largest value of N_t considered was taken as β_0 for this treatment. Then, by plotting $g(x) = \frac{\xi}{\beta_0}$ with respect to $x = \xi \cdot \beta_0(\xi)$, and performing a fit, we can find $g(x)$. Using a fit function of the form $g(x) = a + b \cdot x + c \cdot x^2 + d \cdot x^3 + e \cdot x^4$ we found the value for the fit parameters shown in table 5.2. The points used for the fit, as well as the fit function are shown in figure 5.10.

a	b	c	d	e
-0.193 ± 0.080	1.084 ± 0.077	-0.017 ± 0.026	0.122 ± 0.033	-0.016 ± 0.005

Table 5.2: Parameters obtain in the fit to $g(x) = a + b \cdot x + c \cdot x^2 + d \cdot x^3 + e \cdot x^4$

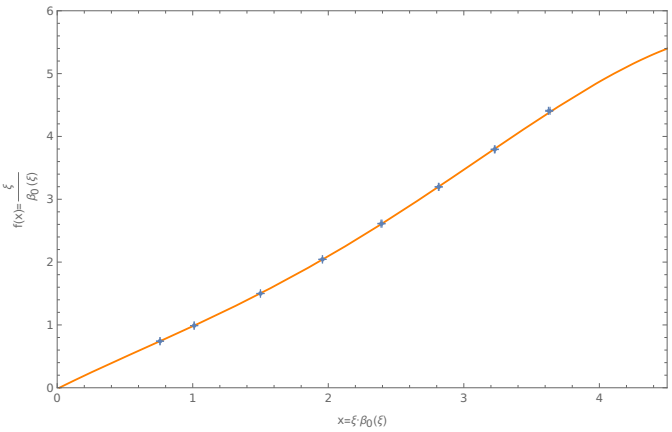

Figure 5.10: Fit function (orange) and points calculated with the values of β_0 and ξ shown in table C.2 (blue).

Using the expression found for $g(x)$ with the fit parameters expressed in table 5.2 we can now plot the points at which the phase transition occurs in terms of $\frac{K}{U}$ and $\frac{T}{U}$, defined in equation 5.4.19 and obtain the phase diagram in figure 5.11. Unlike in the initial case, in which the parameterization of the phase diagram was derived from the action in equation 2.3.44, here the data for different values of the anisotropy parameter ξ are collapsed in a single curve, showing the correct form of the phase diagram. This shows that indeed the term multiplying the space-time plaquette in the initial action was imprecise in the region we are working on, and scaling it with a function as in the action shown in equation 5.4.16 accounted for this fact. However, this phase diagram does not provide all the information about the phases of the $\mathrm{U}(1)$ LGT. Unlike in the previous section, here in order to obtain this rescaled phase diagram, we set $\frac{K}{U} = 1$ in the zero temperature limit. As such, although this approach gives us the correct form of the phase diagram, we have no information about the correct limit of the parameters of the phase diagram, since it can still be globally rescaled. Since in the previous section, we did not impose a value for the limit of $\frac{K}{U}$ at zero temperature, the phase diagram in figure 5.9 can provide an estimate of this quantity, although it is not very precise, as the colapse of the phase diagram obtained using the next order correction to the Villain approximation is not exact in the limit of zero temperature.

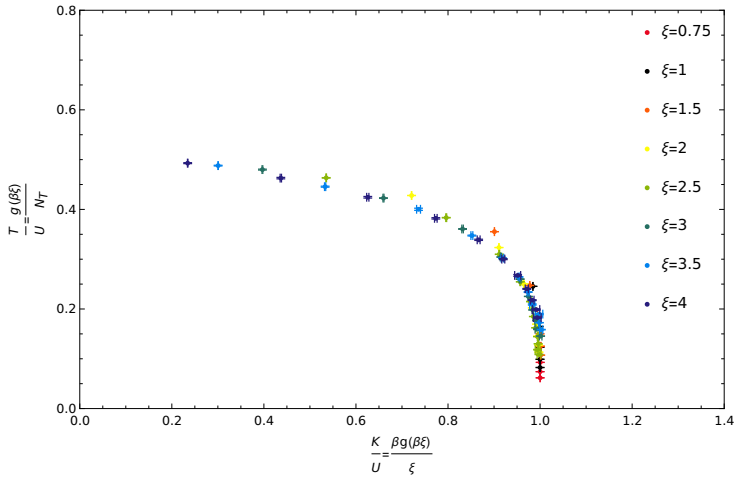

Figure 5.11: Phase diagram in terms of the parameters in equation 5.4.19.

In figure 5.12, we plot the coordinates of the phase transition for each value of ξ and $\mathbf{N}_t$ as well as the different functions used to express the parameters in equation 5.4.19. We note that the initial case is equivalent to using the identity function, $g(x) = x$, while the first order correction to the Villain approxiamtion considered in the previous section corresponds to using the expression in equation 5.4.12 as the rescaling function, with $z = \beta\xi$. We can see that the initial approximation works well for values of the anisotropy parameter close to 1, which explains the proximity of the points calculated for $\xi = 0.75, 1$ and 2 in figure 5.8, However, for larger values of ξ, the identity function becomes increasingly separated from the zero temperature coordinates of the phase transition for each ξ, which explains the inability of this function to produce a collapsed curve on the phase diagram. The function representing the correction to the Villain approximation considered in the last section also agrees with the simulation results for the lowest values of ξ and is closer to our data at higher values of the anisotropy parameter than the initial case. However, it is above the phase transition coordinates for large values of ξ, which is

consistent with the bad collapse of the curves for large values of ξ at low temperature observed in figure 5.9.

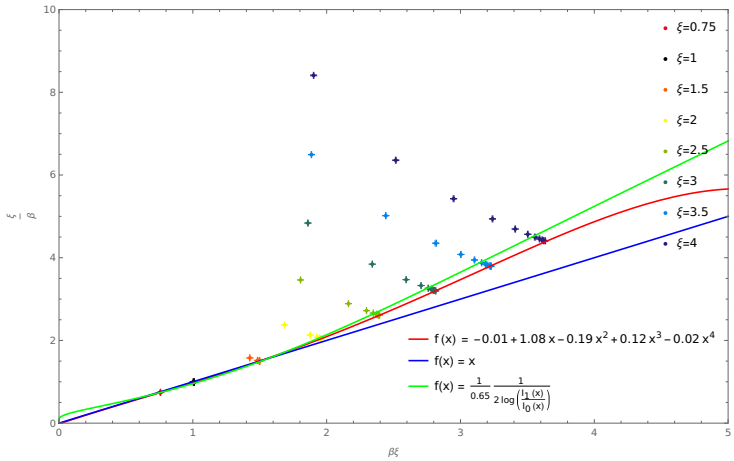

Figure 5.12: Comparison between the different functions used in the relations in equation 5.4.19.

5.5 Running coupling constant

In this section, we study the change of the coupling parameter, β, as we consider anisotropy, through the introduction of the anisotropy parameter, ξ in the lattice action. In order to do so, we will begin by briefly visiting the results of the running coupling constant for $\mathrm{SU}(N)$, and then propose an approach for the $\mathrm{U}(1)$ LGT.

In $\mathrm{SU}(N)$, the lattice gauge action can be written as[2]

$$S = \frac{\beta}{N} \sum_{n} \sum_{\mu<\nu} \mathrm{Re}\,\mathrm{tr}\left[\mathbb{1} - U_{\mu\nu}(n)\right] . \tag{5.5.1}$$

The bare coupling constant g introduced in the action in equation 5.5.1 as $\beta = \frac{2N}{g^2}$ is not a directly observable physical quantity. In order to obtain this quantity in physical units, we need to compute observables on the lattice and identify them with experimental results.

We can consider different derivations of the action 5.5.1 by, for example, considering different discretizations of the derivative or different lattice grids. This will lead to different forms of the action. However, when taking the limit $a \to 0$, the lattice cutoff is removed, and, as such, physical observables must be independent of a and agree with experimental measurements. Since the observables computed on the lattice depend on the lattice spacing a and on the bare coupling g, this implies that the bare coupling g must depend on a, so that the physical observables become independent on a as we take the limit $a \to 0$.

If $P(g(a), a)$ is a physical observable that reproduces the physical value on the limit $a \to 0$, this requirement is given by the differential equation

$$\frac{dP(g,a)}{d\ln a} = 0 \quad \Leftrightarrow \quad \left(\frac{\partial}{\partial \ln a} + \frac{\partial g}{\partial \ln a}\frac{\partial}{\partial g}\right) P(g,a) = 0 . \tag{5.5.2}$$

The coefficient on the second term is the β-function, which gives the dependence of the coupling g on the lattice spacing a,

$$\beta(g) = \frac{\partial g}{\partial \ln a} \,. \tag{5.5.3}$$

This function can be expanded around $g = 0$ using perturbation theory and, in $\mathrm{SU}(N)$ is given by [30]

$$\beta(g) = -b_0 g^3 - b_1 g^5 + \mathcal{O}\left(g^7\right) \,, \tag{5.5.4}$$

with

$$\begin{aligned} b_0 &= \frac{11N}{48\pi^2} \,, \\ b_1 &= \frac{34}{3}\left(\frac{N}{16\pi^2}\right)^2 \,. \end{aligned} \tag{5.5.5}$$

The differential equation 5.5.3 with $\beta(g)$ given by equation 5.5.4 can be solved using separation of variables and yields the following relation between the lattice spacing a and the gauge coupling g [31],

$$a\Lambda_L = \left(b_0 g^2\right)^{-\frac{b_1}{2b_0^2}} \exp\left(-\frac{1}{2b_0 g^2}\right) \,, \tag{5.5.6}$$

with Λ_L the lattice scale parameter used to set the scale by fixing the value of g for some a.

5.5.1 Anisotropic lattice

We can consider the anisotropic lattice regularization [6], in the same way as in section 5.4, by setting different couplings for the spatial and space-time parts of the action. The action for the anisotropic case, in $\mathrm{SU}(N)$, can be written as

$$S = \frac{\beta_t}{N}\sum_{n,\mu} \mathrm{Re}\,\mathrm{tr}\left[\mathbb{1} - \Pi_{\mu 0}(n)\right] + \frac{\beta_s}{N}\sum_{n,\mu<\nu} \mathrm{Re}\,\mathrm{tr}\left[\mathbb{1} - \Pi_{\mu\nu}(n)\right] \,, \tag{5.5.7}$$

with $\beta_t = \xi^2 \beta_s$, where ξ is the anisotropy parameter.

In the this case, the dependence of the lattice spacing on the coupling changes for each ξ and equation 5.5.6 becomes [30]

$$a\Lambda(\xi) = \left(b_0 g'^2\right)^{-\frac{b_1}{2b_0^2}} \exp\left(-\frac{1}{2b_0 g'^2}\right) \,, \tag{5.5.8}$$

with $\frac{2N}{g'^2} = \sqrt{\beta_t \beta_s}$.

If we define $\frac{2N}{g_t^2} = \beta_t$ and $\frac{2N}{g_s^2} = \beta_s$ such that we can write $\frac{1}{g'^2} = \frac{1}{g_t}\frac{1}{g_s}$, we can expand these quantities around $\xi = 1$ as

$$\frac{1}{g_t} = \frac{1}{g} + c_t(\xi) + O(g^2) \,, \tag{5.5.9}$$

$$\frac{1}{g_s} = \frac{1}{g} + c_s(\xi) + O(g^2)\,. \tag{5.5.10}$$

Using these expansions, we can compute the ratio between the lattice scale in the anisotropic and isotropic lattices, given by equations 5.5.8 and 5.5.6, respectively, as

$$\frac{\Lambda(\xi)}{\Lambda_L} = \exp\left(-\frac{c_s(\xi) + c_t(\xi)}{4b_0}\right)\,. \tag{5.5.11}$$

This is equivalent to relating the anisotropic coupling parameters β_t and β_s with the isotropic coupling parameter β as

$$\begin{aligned} \beta_t &= \xi\left(\beta + 2Nc_t(\xi)\right)\,, \\ \beta_s &= \tfrac{\beta + 2Nc_s(\xi)}{\xi}\,. \end{aligned} \tag{5.5.12}$$

Considering the $\frac{1}{\xi}$ expansion of the functions c_t and c_s as

$$2Nc_{t,s} \equiv \alpha^0_{t,s} + \frac{\alpha^1_{t,s}}{\xi} + \cdots\,. \tag{5.5.13}$$

We can express the relation between the isotropic and anisotropic couplings in equation 5.5.12 as

$$\begin{aligned} \beta_t &= \left(\beta + \alpha^0_t\right)\xi + \alpha^1_t\,, \\ \beta_s &= \left(\tfrac{\beta + \alpha^0_s}{\xi}\right) + \tfrac{\alpha^1_t}{\xi^2}\,. \end{aligned} \tag{5.5.14}$$

As we saw in section 5.4, the temperature of an isotropic lattice with a temporal extent N_t is the same as that of an anisotropic lattice with anisotropy parameter ξ and a temporal extent of ξN_t. This fact, together with the results from this section, shows that considering an isotropic lattice with coupling β and N_t points in the temporal direction is equivalent to considering an anisotropic lattice with $\beta_s = \xi^2\beta_t$ and ξN_t points on the temporal direction, with β_t and β_s defined as equation 5.5.14. Classically, the equivalence between the anisotropic and isotropic lattices would be given by $\beta_t = \beta\xi$ and $\beta_s = \frac{\beta}{\xi}$, but in order to take into account the effects of quantum fluctuations at one loop, we must change the coupling parameters according to equation 5.5.14 [31].

The coefficients of the $\frac{1}{\xi}$ expansion of the functions $c_{t,s}$ in equation 5.5.13 hav been determined for $\mathrm{SU}(N)$ by constructing an effective action for the LGT in terms of the Polyakov loop and taking its continuum limit, $a \to 0$. Since in this limit, the results should be independent of the regularization used, equating the actions for $\xi = 1$ and $\xi \neq 1$ gives the correct form of the functions $c_{t,s}$, and thus determines the running of the coupling parameters $\beta_{t,s}$ with the anisotropy parameter [31].

5.5.2 Running coupling in U(1) LGT

The form of the functions $c_{t,s}$ determining the change of the coupling parameter, β with the anisotropy parameter, ξ in $\mathrm{U}(1)$ LGT is not known. However, by inspecting the data obtained in the simulations, we can see that the critical value of the coupling parameter, $\beta_{c,t}$, obtained for the isotropic lattice with N_t points in the temporal direction is not the same as the one obtained for the anisotropic lattices with ξN_t

points in the temporal direction. Since these lattices are at the same temperature, in order for them to be equivalent, the coupling parameter, β, must also depend on ξ.

In order to find the ξ dependence of the coupling parameter, β, for anisotropic lattices, we can compare the values for the critical coupling at the phase transition obtained for lattices with different anisotropy parameters, ξ, at the same temperature, i.e., at constant values of ξN_t for several values of ξ. By plotting this data with respect to ξ and fitting a function through the points, we can obtain the functions $c_{t,s}$ determining the change of the coupling parameter with ξ. Starting from the form of the expression of the running coupling for $\mathrm{SU}(N)$ in equation 5.5.14 and adding terms of higher order in ξ, we propose an anzatz of the form

$$\beta_t = \left(\beta + \alpha_t^0\right)\xi + \alpha_t^1 + \alpha_t^2\xi^2 + \alpha_t^3\xi^3\,, \tag{5.5.15}$$

where β is the coupling parameter in the isotropic lattice with the temperature considered.

The values of the critical coupling at the phase transition, $\beta_{t,c}$, obtained in the simulations for lattice regularizations with $\xi N_t = 4$, 6 and 8 can be seen in tables C.3, C.4 and C.5, respectively. Using this data, a fit was made for each value of ξN_t, using a function of the form of 5.5.15. The fitting parameters obtained are presented in table 5.3.

ξN_t	α_t^0	α_t^1	α_t^2	α_t^3
4	0.21361 ± 0.0031	-0.0992 ± 0.0017	-0.1275 ± 0.0017	0.01309 ± 0.00028
6	0.0358 ± 0.0017	-0.0014 ± 0.0013	-0.0344 ± 0.0004	0
8	0.1092 ± 0.0032	-0.0443 ± 0.0009	-0.0696 ± 0.0013	0.00476 ± 0.00027

Table 5.3: Fitting parameters obtained in the fit of equation 5.5.15 to the data in tables C.3, C.4 and C.5. Note that for $\xi N_t = 6$, the fit was done without the parameter α_t^3 because less points were available.

Having determined the coefficients of the relation between the coupling parameter, β_t and the anisotropy parameter, ξ, we can now invert equation 5.5.15 in order to properly relate the results on the anisotropic lattice with the isotropic case. We find that this is done by changing $\beta_{t,c}$ as

$$\beta_{c,t}(\xi) \to \frac{\beta_{c,t}(\xi) - \alpha_t^1 - \alpha_t^2\xi^2 - \alpha_t^3\xi^3}{\xi} - \alpha_t^0\,. \tag{5.5.16}$$

By applying this transformation on the quantities $\frac{K}{U}$ and $\frac{T}{U}$, in equation 5.4.6 in respect to which we want to plot the phase diagram of the $\mathrm{U}(1)$ LGT we obtain the phase diagram shown in figure 5.13 using the fitting parameters obtained for lattice regularizations with $\xi N_t = 6$. Using the fitting parameters obtained for $\xi N_t = 4$ and $\xi N_t = 8$, we obtain phase diagrams consistent with the one shown. These can be found, respectively, in figures C.1 and C.2.

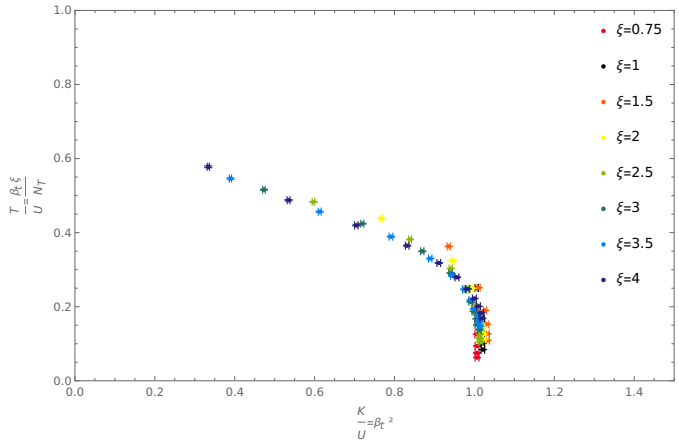

Figure 5.13: Phase diagram of the $\mathrm{U}(1)$ LGT in terms of the parameters in equation 5.4.6 with the coupling parameter transformed according to equation 5.5.16, with the parameters obtained for lattice regularizations with $\xi N_t = 6$

5.6 Renormalized anisotropy parameter

By expanding the action for the $\mathrm{U}(1)$ LGT in terms of small lattice spacings and using $\beta = \frac{2}{g^2}$, with g the bare coupling constant, we find, at the classical level, $\xi = \frac{a_s}{a_t}$. However, ξ is not the physical ratio between lattice spacings in the spatial and temporal directions, and we should refer to this parameter as the *bare anisotropy parameter*. The actual physical ratio between a_s and a_t can differ from the bare anisotropy parameter. In this section, we will look at a method to determine the *renormalized coupling parameter*, $\xi_r = \left(\frac{a_s}{a_t}\right)_{phys}$.

As we saw in section 2.4.1, we can relate the potential for a fermion-antifermion pair propagating in the temporal direction with the average value of the Wilson loop. Let's denote by $W_{st}(r,t)$ a Wilson loop in which the Wilson lines extend over a distance r in one spatial direction and the temporal propagators extend over a distance t in the temporal direction, with r and t in lattice units. From equation 2.4.13, we see that we can determine the potential as

$$a_t V_t(r) = \log\left[\frac{W_{st}(r,t)}{W_{st}(r,t+1)}\right], \tag{5.6.1}$$

which is valid at large temporal distances t.

Similarly, if we consider a quantity similar to the Wilson loop, composed by Wilson lines in one spatial direction, but with the temporal propagators replaced by *spatial propagators* in another direction, we can define a *spatial Wilson loop*, $W_{ss}(r_1, r_2)$, and relate it to the potential of a fermion-antifermion pair propagating in the spatial direction of the spatial propagator. This way, we can determine the spatial potential as

$$a_s V_s(r_1) = \log\left[\frac{W_{ss}(r_1,r_2)}{W_{ss}(r_1,r_2+1)}\right]. \tag{5.6.2}$$

The potentials $V_t(r)$ and $V_s(r)$ are measured, respectively, in units of a_t and a_s. As such, they differ by a factor of $\xi_r = \left(\frac{a_s}{a_t}\right)$. They should also differ by an additive constant, resulting from the fact that the

self-energy corrections to the potential are different for spatial and temporal propagation. [32]

$$a_s V_s(r) = \xi_r a_t V_t(r) + const\,. \tag{5.6.3}$$

As such, we can compute the physical ratio between the spatial and temporal lattice spacings, by determining the spatial and temporal potentials, and calculating the ratio [32, 33]

$$\xi_r = \frac{a_s V_s(r_1) - a_s V_s(r_2)}{a_t V_t(r_1) - a_t V_t(r_2)}\,, \tag{5.6.4}$$

for two different distances r_1 and r_2, in lattice units.

The spatial and temporal potentials calculated with the Wilson loop at the phase transition are plotted in figure 5.14 for some values of the bare anisotropy parameter ξ. As expected, for the isotropic case with $\xi = 1$, the two potentials are the same as in this case there is no difference between the temporal and spatial directions. For $\xi = 0.75$, we find a temporal potential larger than the spatial potential, which is consistent with a value of ξ_r below 1. Consistently, for $\xi = 2$, we find a spatial potential larger then the temporal potential which is in accordance with a value of ξ_r greater than one. The errors in the potential increase rapidly with increasing distance r. This is due to the fact that the signal to noise ratio for the Wilson loop is very low, and decreases for large values of r.

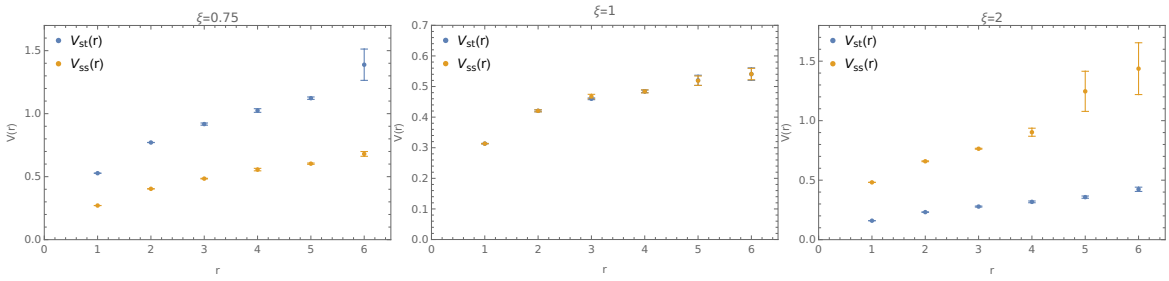

((a)) $\xi = 0.75$ ((b)) $\xi = 1$ ((c)) $\xi = 2$

Figure 5.14: Potential calculated on a 24^4 lattice for β at the phase transition, using the Wilson Loop, for several values of ξ.

In table 5.4, we present the values of the physical ratio between the spatial and temporal lattice spacings calculated at the phase transition for the different values of the anisotropy parameter, ξ used. In the isotropic case, with $\xi = 1$, the values of the physical ratio between the lattice spacings are consistent with $\xi_r = 1$, as expected. For the anisotropic lattices considered, we can see that the value of ξ_r is greater that ξ for lattices with $\xi > 1$ and less that the value of ξ for the case with an anisotropy parameter $\xi < 1$, with the difference between the anisotropy parameter and the renormalised anisotropy parameter increasing with increasing ξ.

ξ	β	a_s/a_t		
		$R_1 = a_s$ $R_2 = 2a_s$	$R_1 = a_s$ $R_2 = 3a_s$	$R_1 = 2a_s$ $R_2 = 3a_s$
0.75	1.01145	0.545 ± 0.004	0.548 ± 0.014	0.55 ± 0.04
1	1.01057	1.00 ± 0.04	1.05 ± 0.05	1.19 ± 0.24
1.5	0.9998	1.78 ± 0.04	1.87 ± 0.11	2.00 ± 0.30
2	0.9785	2.46 ± 0.08	2.38 ± 0.09	2.26 ± 0.25
2.5	0.9570	3.19 ± 0.13	3.30 ± 0.15	3.5 ± 0.6
3	0.9383	3.89 ± 0.17	3.88 ± 0.22	3.9 ± 0.7
3.5	0.9223	4.42 ± 0.24	4.43 ± 0.29	4.5 ± 0.9
4	0.9075	5.00 ± 0.23	5.3 ± 0.4	5.7 ± 1.0

Table 5.4: Values of $\left(\frac{a_s}{a_t}\right)_{phys}$ calculated at the phase transition on a 24^4 lattice, for each ξ, using different distances.

Chapter 6

Conclusion

This project was motivated by the fact that, although many properties of the $\mathrm{U}(1)$ LGT have already been studied, a complete phase diagram for this theory was missing from the literature. In this work, by simulating the $\mathrm{U}(1)$ LGT on lattices with different sizes in the temporal and spatial directions using Markov Chain Monte Carlo methods, we were able to retrieve the full phase diagram of this theory.

For the isotropic lattice considered in the beginning of this work, we were able to identify the phase transition by looking at the Polyakov loop and the string tension as order parameters, and recover results consistent with those found in the literature. Then, by introducing anisotropy between the spatial and temporal directions on the lattice, we were able to probe the theory at higher temperatures, and thus obtain the coordinates of the phase transition in a broader parameter region.

We were able to identify the order of the phase transition for different values of the lattice temporal extent for the isotropic regularization, determining that it is of first order at low temperatures, as defined in the Hamiltonian picture, and becomes weaker with increasing temperature until it becomes second order. However, this is not enough to identify the exact point where the order of the phase transition changes along the curve in the phase diagram. By considering anisotropic lattices, we were able to extend the range of temperatures and coupling parameters at which we were able to study the $\mathrm{U}(1)$ LGT. Therefore, in the future, in order to determine the value of the temperature at which the phase transition goes from discontinuous to continuous more accurately, it would be interesting to consider the anisotropic lattice regularization, and repeat the process used in section 5.3 to determine the order of the phase transition at different lattice extents in the temporal direction.

Bibliography

[1] K. G. Wilson, *Phys. Rev. D* **10**, 2445 (1974).

[2] C. Gattringer, C. B. Lang, *Quantum chromodynamics on the lattice*, vol. 788 (Springer, Berlin, 2010).

[3] J. Smit, *Introduction to Quantum Fields on a Lattice (Cambridge Lecture Notes in Physics, 15)* (2002).

[4] J. Kogut, L. Susskind, *Physical Review D* **11**, 395 (1975).

[5] J. Villain, *Journal de Physique* **36**, 581 (1975).

[6] J. Engels, F. Karsch, H. Satz, I. Montvay, *Nuclear Physics B* **205**, 545 (1982).

[7] A. M. Polyakov, *Gauge Fields and Strings*, vol. 3 (1987).

[8] A. M. Polyakov, *Physics Letters B* **59**, 82 (1975).

[9] T. Banks, R. Myerson, J. Kogut, *Nuclear Physics B* **129**, 493 (1977).

[10] S. D. Drell, H. R. Quinn, B. Svetitsky, M. Weinstein, *Phys. Rev. D* **19**, 619 (1979).

[11] J. M. Kosterlitz, D. J. Thouless, *Journal of Physics C: Solid State Physics* **6**, 1181 (1973).

[12] T. A. DeGrand, D. Toussaint, *Physical Review D* **22**, 2478 (1980).

[13] P. A. M. Dirac, *Proceedings of the Royal Society of London. Series A, Containing Papers of a Mathematical and Physical Character* **133**, 60 (1931).

[14] J. Gervais, *et al.*, *Non-linear and Collective Phenomena in Quantum Physics: A Reprint Volume from Physics Reports* **23**, 6 (1983).

[15] M. Vettorazzo, P. de Forcrand, *Nucl. Phys. B* **686**, 85 (2004).

[16] G. Arnold, B. Bunk, T. Lippert, K. Schilling, *Nucl. Phys. B Proc. Suppl.* **119**, 864 (2003).

[17] J. de Sousa, D. F. de Albuquerque, *Physica A: Statistical Mechanics and its Applications* **236**, 419 (1997).

[18] M. Vettorazzo, P. De Forcrand, Finite temperature phase transition in the 4d compact U(1) lattice gauge theory, *Tech. rep.* (2004).

[19] C. Bonati, M. D'elia, Phase diagram of the 4D U(1) model at finite temperature, *Tech. rep.* (2013).

[20] H. J. Rothe, *Lattice gauge theories: An Introduction*, vol. 43 (1992).

[21] D. P. Landau, *A guide to Monte Carlo simulations in statistical physics* (2013), third edition. edn.

[22] N. Metropolis, A. W. Rosenbluth, M. N. Rosenbluth, A. H. Teller, E. Teller, *The Journal of Chemical Physics* **21**, 1087 (1953).

[23] W. K. Hastings, *Biometrika* **57**, 97 (1970).

[24] M. H. Quenouille, *Biometrika* **43**, 353 (1956).

[25] J. Tukey, *Ann. Math. Statist.* **29**, 614 (1958).

[26] G. Parisi, R. Petronzio, F. Rapuano, *Phys. Lett. B* **128**, 418 (1983).

[27] A. Irback, C. Peterson, *Phys. Rev. D* **36**, 3804 (1987).

[28] M. Lüscher, P. Weisz, *Journal of High Energy Physics* **2001**, 010–010 (2001).

[29] W. Janke, H. Kleinert, *Nuclear Physics, Section B* **270**, 135 (1986).

[30] F. Karsch, *Nuclear Physics B* **205**, 285 (1982).

[31] M. Billó, M. Caselle, A. D'Adda, S. Panzeri, *Nuclear Physics B* **472**, 163 (1996).

[32] T. R. Klassen, *Nucl. Phys. B* **533**, 557 (1998).

[33] N. H. Shakespeare, H. D. Trottier, *Phys. Rev. D* **59**, 014502 (1999).

Appendix A

Gauge fixing

In this section, we briefly describe the process of fixing a gauge in a pure lattice gauge theory.

Starting from a random configuration of link variables, and with all the gauge transformation matrices set to the identity, $\Omega(n) = \mathbb{1}$, we can gauge transform a link variable, $U_{\mu_0}(n_0)$ to the identity by setting the transformation matrix on the end point of the link, i.e., on the lattice site $n_0+\mu_0$ as $\Omega(n_0+\mu_0) = U_{\mu_0}(n_0)$. This way, the link variable $U_{\mu_0}(n_0)$ transforms as

$$U_{\mu_0}(n_0) \to \Omega(n_0)U_{\mu_0}(n_0)\Omega^\dagger(n_0+\mu_0) = \mathbb{1}U_{\mu_0}(n_0)U^\dagger_{\mu_0}(n_0) = \mathbb{1}\,. \tag{A.1}$$

This change of value for the transformation matrix $\Omega(n_0+\mu_0)$ also has an effect on other link variables connected to the site $n_0+\mu_0$. For example, a link variable with direction μ_1 starting on $n_0+\mu_0$ will transform as

$$U_{\mu_1}(n_0+\mu_0) \to \Omega(n_0+\mu_0)U_{\mu_1}(n_0+\mu_0)\Omega^\dagger(n_0+\mu_0+\hat{\mu_1}) = U_{\mu_0}(n_0)U_{\mu_1}(n_0+\mu_0)\mathbb{1} = U_{\mu_0}(n_0)U_{\mu_1}(n_0+\mu_0)\,. \tag{A.2}$$

The same transformation can be made to set other link variables to $\mathbb{1}$. As changing the transformation matrix on the site corresponding to the endpoint of a link also changes other link variables connected to that site, we can gauge transform all links to the identity, except those which are connected to a link that has previously been gauge transformed to $\mathbb{1}$, as doing so would change the value of that link. As such, the set of links that we can gauge transform to the identity corresponds to the a cluster of links which does not contain closed loops. This cluster is called a *maximal tree*. [2] Note that transforming the links on a subset of a maximal tree to the identity also corresponds to a gauge fixing.

As the observables calculated in LGT are gauge invariant, the process of gauge fixing on a maximal tree of links, or on a subset of a maximal tree, does not change the expectation value of the observable. Link variables gauge transformed to $\mathbb{1}$ can then be removed from the integrals in order to simplify calculations.

A.1 Temporal gauge

One particular example of a gauge fixing in which link variables are set to the identity in a subset of a maximal tree is the temporal gauge. This gauge corresponds to setting all temporal links to $\mathbb{1}$ on a lattice with an infinite lattice extent, as

$$U_0(n) = \mathbb{1} \quad , \forall n \, . \tag{A.1}$$

Since the link variables are given by $U_\mu(n) = e^{iagA_\mu(n)}$, the counterpart of the temporalgauge on the continuum is defined by fixing $A_0(x) = 0$ for all x.

Appendix B

Euclidean correlator

The euclidean correlator between two observables is defined as [2]

$$\langle O_2(t)O_1(0)\rangle_T = \frac{1}{Z_T}\,\mathrm{tr}\left[e^{-(T-t)\hat{H}}\widehat{O}_2 e^{-t\widehat{H}}\widehat{O}_1\right]\,, \tag{B.1}$$

where t is the euclidean temporal distance between the observables O_1 and O_2, T is the temporal extent of the system, Z_T is a normalization factor given by

$$Z_T = \mathrm{tr}\left[e^{-T\widehat{H}}\right]\,, \tag{B.2}$$

and $\hat{H}$ is the Hamiltonian operator with eigenstate $|n\rangle$ such that

$$\hat{H}|n\rangle = E_n|n\rangle\,, \tag{B.3}$$

where E_n is the energy of state $|n\rangle$. The energies of the eigenstates of the Hamiltonian are ordered as

$$E_0 < E_1 < E_2 < \cdots\,. \tag{B.4}$$

We can evaluate the normalization factor, Z_T as

$$Z_T = \mathrm{tr}\left[e^{-T\widehat{H}}\right] = \sum_n \left\langle n\left|e^{-T\widehat{H}}\right|n\right\rangle = \sum_n \left\langle n\left|e^{-TE_n}\right|n\right\rangle = \sum_n e^{-TE_n}\langle n|n\rangle = \sum_n e^{-TE_n}\,, \tag{B.5}$$

where in the last step we used $\langle n|n\rangle = 1$. We can express Z_T in terms of the energy differences with respect to the vacuum energy E_0 as $\Delta E_n = E_n - E_0$, by writing

$$\begin{aligned} Z_T = \sum_n e^{-TE_n} &= e^{-TE_0} + e^{-TE_1} + e^{-TE_2} + \cdots \\ &= e^{-TE_0}(1 + e^{-T\Delta E_1} + e^{-T\Delta E_2} + \cdots)\,. \end{aligned} \tag{B.6}$$

We can also evaluate the trace in equation B.1 as,

$$\mathrm{tr}\left[e^{-(T-t)\hat{H}}\widehat{O}_2 e^{-t\widehat{H}}\widehat{O}_1\right] = \sum_m \left\langle m \left| e^{-(T-t)\widehat{H}}\widehat{O}_2 e^{-t\hat{H}}\widehat{O}_1 \right| m \right\rangle . \tag{B.7}$$

By inserting a partition of the identity $\mathbb{1} = \sum_n |n\rangle\langle n|$ in the previous equation and acting with the Hamiltonian operators on the bras, we get

$$\begin{aligned}
\mathrm{tr}\left[e^{-(T-t)\hat{H}}\widehat{O}_2 e^{-t\widehat{H}}\widehat{O}_1\right] &= \sum_{m,n} \left\langle m \left| e^{-(T-t)\widehat{H}}\widehat{O}_2 \right| n \right\rangle \left\langle n \left| e^{-t\hat{H}}\widehat{O}_1 \right| m \right\rangle \\
&= \sum_{m,n} e^{-(T-t)E_m} \left\langle m \left| \widehat{O}_2 \right| n \right\rangle e^{-tE_n} \left\langle n \left| \widehat{O}_1 \right| m \right\rangle \\
&= \sum_{m,n} \left\langle m \left| \widehat{O}_2 \right| n \right\rangle \left\langle n \left| \widehat{O}_1 \right| m \right\rangle e^{-(T-t)E_m} e^{-tE_n} \\
&= e^{-tE_0} \sum_{m,n} \left\langle m \left| \widehat{O}_2 \right| n \right\rangle \left\langle n \left| \widehat{O}_1 \right| m \right\rangle e^{-(T-t)\Delta E_m} e^{-t\Delta E_n} ,
\end{aligned} \tag{B.8}$$

where in the last term we factorized e^{-tE_0} in order to express the argument of the sum in terms of the energy differences with respect to the vacuum.

Inserting the result of equations B.6 and B.8 in the definition of the euclidean correlator in equation B.1, we obtain

$$\langle O_2(t)O_1(0)\rangle_T = \frac{\sum_{m,n} \left\langle m \left| \widehat{O}_2 \right| n \right\rangle \left\langle n \left| \widehat{O}_1 \right| m \right\rangle e^{-t\Delta E_n} e^{-(T-t)\Delta E_m}}{1 + e^{-T\Delta E_1} + e^{-T\Delta E_2} + \ldots} . \tag{B.9}$$

We note that the correlator in equation B.9 does not depend on the energies of the eigenstates of the Hamiltonian, $|n\rangle$, but only on the energy differences ΔE_n. As such, we can do a shift in all energies by setting $E_0 = 0$, so that we can denote the energy differences as simply E_n.

In the limit $T \to \infty$, all the terms in the denominator except the first vanish. Moreovere, in the numerator, because of the factor $e^{-T\Delta E_m}$, only terms with $\Delta E_m = 0$, i.e., $|m\rangle = |0\rangle$, contribute to the sum. As such, we finaly obtain the euclidean correlator as

$$\langle O_2(t)O_1(0)\rangle_T = \sum_n \left\langle 0 \left| \widehat{O}_2 \right| n \right\rangle \left\langle n \left| \widehat{O}_1 \right| 0 \right\rangle e^{-t\Delta E_n} . \tag{B.10}$$

Appendix C

Tables and Figures

β	a	b	σ	$\chi^2/d.o.f$
0.96	0.48247 ± 0.08951	0.32338 ± 0.10920	0.384796 ± 0.01754	11.67
0.97	0.52332 ± 0.00806	0.34358 ± 0.01011	0.33550 ± 0.00152	0.84
0.98	0.56585 ± 0.00450	0.36636 ± 0.00577	0.28223 ± 0.00082	0.07
0.99	0.59417 ± 0.00378	0.36700 ± 0.00500	0.22412 ± 0.00066	0.08
0.995	0.60368 ± 0.01509	0.36536 ± 0.02056	0.19358 ± 0.00025	1.47
1	0.59860 ± 0.00237	0.34188 ± 0.00334	0.16131 ± 0.00038	1.00
1.001	0.61437 ± 0.00122	0.32820 ± 0.06178	0.07406 ± 0.00018	0.01
1.003	0.59299 ± 0.00702	0.32501 ± 0.01002	0.13921 ± 0.00004	0.69
1.005	0.60035 ± 0.00797	0.32419 ± 0.01136	0.12012 ± 0.00124	0.46
1.007	0.62186 ± 0.00302	0.34279 ± 0.00414	0.09567 ± 0.00050	0.03
1.01	$0.61101 \pm .00314$	0.32114 ± 0.00469	0.05948 ± 0.00045	0.06
1.0102	0.58729 ± 0.00093	0.25548 ± 0.00093	-0.001307 ± 0.00004	0.01
1.0105	0.53419 ± 0.00032	0.23532 ± 0.00062	-0.00118 ± 0.00003	0.06
1.015	0.49474 ± 0.00054	0.20226 ± 0.00108	-0.00122 ± 0.00005	0.43
1.02	0.47279 ± 0.00068	0.18713 ± 0.00135	-0.00114 ± 0.00006	3.52
1.03	0.44523 ± 0.00063	0.17123 ± 0.00126	-0.00102 ± 0.00006	8.91
1.04	0.42560 ± 0.00057	0.16131 ± 0.00114	-0.00095 ± 0.00005	11.81
1.05	0.41019 ± 0.00052	0.15402 ± 0.00105	-0.00089 ± 0.00005	16.47
1.06	0.39742 ± 0.00048	0.14840 ± 0.00095	-0.00085 ± 0.00005	18.53

Table C.1: Fitting parameters obtained in the fit of an equation of the form $aV(r) = A - \frac{b}{r} + \sigma r$ to the potential obtained for a 24^4 isotropic lattice.

ξ	N_t	β_C
0.75	2	0.97372 ± 0.00023
	4	1.00920 ± 0.00034
	6	1.01122 ± 0.00006
	8	1.01153 ± 0.00013
	10	1.01141 ± 0.00014
	12	1.01145 ± 0.00017
1	2	0.89929 ± 0.00015
	4	1.00276 ± 0.00006
	6	1.00948 ± 0.00009
	8	1.01043 ± 0.00009
	10	1.01051 ± 0.00054
	12	1.01057 ± 0.00007
1.5	2	0.68221 ± 0.00019
	4	0.95067 ± 0.00008
	6	0.98846 ± 0.00007
	8	0.99650 ± 0.00007
	10	0.99911 ± 0.00010
	12	0.9996 ± 0.0008
	14	0.9998 ± 0.0003
2	2	0.52554 ± 0.00026
	4	0.84230 ± 0.00032
	6	0.93856 ± 0.00026
	8	0.96366 ± 0.00024
	10	0.97204 ± 0.00008
	12	0.97617 ± 0.00028
	14	0.97728 ± 0.00012
	16	0.97811 ± 0.00014
	18	0.9785 ± 0.0005
2.5	2	0.4239 ± 0.0004
	4	0.7220 ± 0.0004
	6	0.8652 ± 0.0005
	8	0.91916 ± 0.00033
	10	0.93942 ± 0.00044
	12	0.9490 ± 0.0009
	14	0.95173 ± 0.00010
	16	0.95394 ± 0.00006
	18	0.95561 ± 0.00015
	20	0.95618 ± 0.00026
	22	0.9557 ± 0.0019
	24	0.9570 ± 0.0015
3	2	0.3540 ± 0.0006
	4	0.6200 ± 0.0007
	6	0.7803 ± 0.0005
	8	0.8646 ± 0.0006
	10	0.9018 ± 0.0005
	12	0.9197 ± 0.0005
	14	0.92719 ± 0.00029
	16	0.9312 ± 0.0004
	18	0.9348 ± 0.0012
	20	0.9355 ± 0.0015
	22	0.9383 ± 0.0008
3.5	2	0.30344 ± 0.00032
	4	0.5390 ± 0.0004
	6	0.6977 ± 0.0006
	8	0.8045 ± 0.0014
	10	0.8580 ± 0.0006
	12	0.8871 ± 0.0007
	14	0.9022 ± 0.0004
	16	0.9105 ± 0.0005
	18	0.9143 ± 0.0013
	20	0.9204 ± 0.0018
	22	0.92062 ± 0.00031
	24	0.9223 ± 0.0008
4	2	0.26607 ± 0.00026
	4	0.4757 ± 0.0005
	6	0.6291 ± 0.0008
	8	0.7372 ± 0.0008
	10	0.8098 ± 0.0007
	12	0.8522 ± 0.0007
	14	0.8758 ± 0.0007
	16	0.8893 ± 0.0012
	18	0.8978 ± 0.0006
	20	0.9028 ± 0.0007
	22	0.9064 ± 0.0014
	24	0.9075 ± 0.0015

Table C.2: Position of the peak in the Polyakov loop susceptibility, β_C,for each value of ξ and $N_t$on a $4\mathcal{D}$ lattice with $N_s = 24$.

ξ	N_t	$\beta_{t,c}$
1	4	1.00276 ± 0.00006
1.5	6	1.48268 ± 0.00011
2	8	1.9273 ± 0.0005
2.5	10	2.3489 ± 0.0007
3	12	2.7571 ± 0.0008
3.5	14	3.1557 ± 0.0019
4	16	3.5628 ± 0.0018

Table C.3: Critical value of β_t obtained in the simulations with $4\mathcal{D}$ lattices regularizations in which $\xi N_t = 4$ and $N_s = 24$.

ξ	N_t	$\beta_{t,c}$
1	6	1.00948 ± 0.00009
2	12	1.9523 ± 0.0006
3	18	2.8043 ± 0.0035
4	24	3.6297 ± 0.0018
5	30	4.468 ± 0.019

Table C.4: Critical value of β_t obtained in the simulations with $4\mathcal{D}$ lattices regularizations in which $\xi N_t = 6$ and $N_s = 24$.

ξ	N_t	$\beta_{t,c}$
0.75	6	0.75841 ± 0.00004
1	8	1.01043 ± 0.00009
1.5	12	1.4993 ± 0.0012
2	16	1.95622 ± 0.00028
2.5	20	2.3905 ± 0.0006
3	24	2.8110 ± 0.0030
4	32	3.640 ± 0.004

Table C.5: Critical value of β_t obtained in the simulations with $4\mathcal{D}$ lattices regularizations in which $\xi N_t = 8$ and $N_s = 24$.

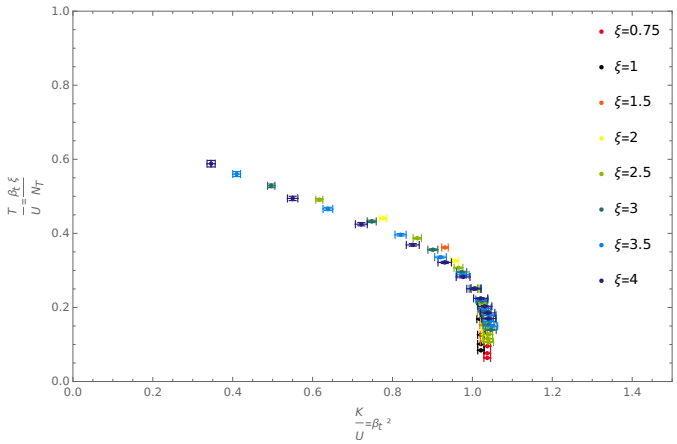

Figure C.1: Phase diagram of the $\mathrm{U}(1)$ LGT in terms of the parameters in equation 5.4.6 with the coupling parameter transformed according to equation 5.5.16, with the parameters obtained for lattice regularizations with $\xi N_t = 4$

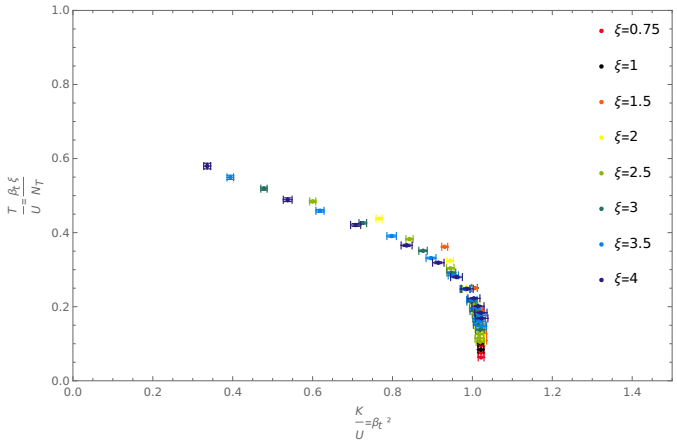

Figure C.2: Phase diagram of the $\mathrm{U}(1)$ LGT in terms of the parameters in equation 5.4.6 with the coupling parameter transformed according to equation 5.5.16, with the parameters obtained for lattice regularizations with $\xi N_t = 8$